

## ABSTRACT

MORRISSEY, PATRICK DESMOND. Fabrication, Distortion, and Metrology of Shrink Fit Electrical Connections. (Under the direction of Dr. Jeffrey W. Eischen)

The fabrication of pulsed-power experiments on systems such as ATLAS at Los Alamos National Labs requires assembly of shrink fit or press fit joints. These joints are used to carry large electrical currents on the order of several megampères for Z-pinch cylindrical implosions of thin-walled cylinders. The joints, which represent the shrink fit or press fit interfaces between cylindrical components (1100 aluminum liners and copper glide planes), are also called on to support mechanical stresses. As a result, the integrity of these joints is critical to the success of the mission. The analytical challenge for investigating these components lies in the presence of a partial shrink fit, that is, a shrink fit in which the length of contact between mating cylinders does not equal the entire length of at least one of the components. Such a design leads to stress distributions that are impossible to calculate using standard shrink fit theory that is analytically tractable. Arguably more important, however, is the varying radial deflection profile along the length of the liner that results from the partial shrink fit. For the success of these experiments, uniform implosions are deemed to be highly beneficial; thus, determining how to predict and compensate for liner deflection profiles is crucial.

The primary issues at hand include the following: mechanics of the interference fits, physical description of the contact surfaces between the liner and glide planes, joint void (gap) description, and material property effects. Furthermore, for the shrink fit design of ATLAS Generation I, liner geometry alterations were investigated for potential performance

improvement, particularly for the elimination of joint interface gaps and lower stress magnitudes. For the modified ATLAS design that included components designed to compress and distort other elements (Generation II), effects of localized geometry modifications were investigated for the same purposes. Composite liners, i.e., liners with two constituent materials, were also examined, along with potential problems such as cylindrical out-of-roundness on the precision scale. To investigate these issues, finite element analysis models have been created and compared to experimental data. A measurement technique has been developed to compare radial deflection profiles of diamond turned thin-walled shrink fit test specimens to finite element models of corresponding geometry. Verification of the computer generated finite element models with experimental results could provide tremendous aid in accurately predicting the shape, deflection, and stress distribution of such cylindrical elements.

# **FABRICATION, DISTORTION, AND METROLOGY OF SHRINK FIT ELECTRICAL CONNECTIONS**

by

**Patrick Desmond Morrissey**

A thesis submitted in partial fulfillment of the  
requirements for the degree of

Master of Science

**Department of Mechanical Engineering**

**North Carolina State University**  
Raleigh, NC

May 2003

Approved by:

---

Chair of Advisory Committee

## **DEDICATION**

This work is dedicated in memory of  
my mother, Jane Morrissey,  
who has always given me  
inspiration in my education  
and in everything I have achieved.

## **BIOGRAPHY**

Patrick Desmond Morrissey was born in Stamford, Connecticut and grew up in Greensboro, North Carolina. He was an avid player of the piano and guitar, and enjoyed playing soccer and lacrosse for several years. He attended North Carolina State University and graduated in December of 2000 with a Bachelor of Science in Mechanical Engineering. Patrick worked at Guilford Mills Incorporated in Greensboro as an intern during the summers of 1998 and 1999 working on improving their heating systems for fabric production. Upon completion of his undergraduate studies, Patrick immediately continued into the Masters Program for Mechanical Engineering. He began as a teaching assistant, directing mechanical engineering labs for undergraduate students, and later joined the Precision Engineering Center in August of 2001. His research, sponsored by Los Alamos National Laboratories, is a finite element analysis of components in high-energy pulsed-power experiments. He graduated in August of 2003.

## ACKNOWLEDGEMENTS

There are many people who played a key role in the completion of my graduate studies, whether educationally, inspirationally, and/or financially. I would like to thank the following individuals for all the help they have given me:

- **Los Alamos National Laboratories** – Special thanks for the project funding, which was graciously appreciated.
- **Dad, Meghan, Amy, and Brent** – Your constant praise and support has given me motivation to excel and perform to my full ability. Thanks for all the advice you've given me and for always being there.
- **Dr. Eischen** – Your knowledge in the field of my research, along with your guidance and patience, played a key role in the completion of my work.
- **Dr. Dow** – Thanks for bringing me in and for giving me the opportunity to use such a paramount facility.
- **Alex and Ken** – Your superior knowledge in Precision Engineering and the equipment at the PEC has been a remarkable help for me. I've always been amazed by your willingness to assist others and myself first, no matter how busy you may have been.
- **David, Nobu, Stuart, Travis, and Witoon** – Thanks for keeping us all down to Earth even when times were tense with studies and research.
- **The Brothers of Chi Psi Fraternity** – You all have given me wonderful memories throughout my entire schooling career.

## TABLE OF CONTENTS

<b>LIST OF TABLES .....</b>	<b>viii</b>
<b>LIST OF FIGURES .....</b>	<b>ix</b>
<b>LIST OF SYMBOLS &amp; ABBREVIATIONS .....</b>	<b>xiv</b>
<b>1.0 INTRODUCTION.....</b>	<b>1</b>
1.1 Pulsed-Power Technology.....	2
1.2 Background.....	3
1.3 Pulsed-Power Experiment Design Criteria.....	4
1.3.1 Current Rise Time Determination .....	5
1.3.2 Conductor Motion.....	6
1.3.3 Contact Design .....	8
1.3.4 Thermal Difficulties.....	9
1.3.5 Current Concentrations .....	9
1.3.6 Vapor Production.....	10
<b>2.0 FINITE ELEMENT MODELING .....</b>	<b>12</b>
2.1 Standard Shrink Fit Modeling .....	12
2.1.1 Number of Elements and Convergence .....	15
2.2 Partial Shrink Fit Modeling .....	18
2.3 Finite Element Analysis of ATLAS .....	21
2.3.1 Geometry and Material Properties.....	21
2.3.2 Thermal Shrink Fit Assembly .....	23
2.3.3 Radial Deflection Results.....	24
2.3.4 Radial Deflection Compensation.....	29
2.3.5 Liner / Glide Plane System Integrity .....	31

<b>3.0 ADVANCED LINER ANALYSIS AND REDESIGN .....</b>	<b>34</b>
3.1    Gap Analysis and Liner Design Changes.....	34
3.2    Effects of an Out-of-Round Liner.....	39
<b>4.0 FINITE ELEMENT VERIFICATION .....</b>	<b>43</b>
4.1    Shrink Fit Test Specimen #1.....	43
4.1.1    Test Specimen #1: Design.....	43
4.1.2    Test Specimen #1: Fabrication and Dimensional Measurements .....	49
4.1.3    Test Specimen #1: Surface Measurements .....	50
4.2    Shrink Fit Test Specimen #2.....	53
4.2.1    Test Specimen #2: Design.....	53
4.2.2    Test Specimen #2: Fabrication and Dimensional Measurements .....	53
4.2.3    Test Specimen #2: Surface Measurements .....	57
4.3    Shrink Fit Test Specimen #3.....	60
4.3.1    Test Specimen #3: Design.....	60
4.3.2    Test Specimen #3: Fabrication and Dimensional Measurements .....	60
4.3.3    Test Specimen #3: Surface Measurements .....	66
<b>5.0 ATLAS GENERATION II .....</b>	<b>73</b>
5.1    Finite Element Analysis of ATLAS Generation II .....	73
5.1.1    Upper Glide Plane / Liner Interaction.....	78
5.1.2    Compression Ring Modeling .....	80
5.1.3    Suggested Geometric Changes in the Lower Ring Compressor .....	82
<b>6.0 COMPOSITE LINERS.....</b>	<b>84</b>
6.1    Composite Liner Geometry Effects .....	85
6.1.1    Radial Gap Analysis .....	87
6.1.2    Radial Deflection Analysis .....	89
6.1.3    Stress Analysis .....	92

<b>7.0 CONCLUSIONS .....</b>	<b>95</b>
7.1 Standard Shrink Fit Modeling .....	95
7.2 ATLAS Modeling .....	95
7.2.1 Radial Deflection Prediction and Compensation .....	95
7.2.2 Interface Gap Prediction and Compensation.....	96
7.3 Finite Element Verification .....	97
7.3.1 Radial Measurement Techniques .....	97
7.3.2 Radial Deflection Measurements .....	97
7.4 ATLAS Generation II Modeling.....	99
7.4.1 Small Glide Plane / Liner Interface .....	99
7.4.2 Compression Ring Distortion.....	99
7.5 Composite Liners .....	100
<b>LIST OF REFERENCES.....</b>	<b>102</b>
<b>APPENDIX A .....</b>	<b>103</b>
<b>APPENDIX B .....</b>	<b>107</b>

## LIST OF TABLES

Table 1 Shrink fit model dimension parameters .....	14
Table 2 Shrink fit model contact parameters .....	14
Table 3 Material properties used in ATLAS simulations.....	22
Table 4 Maximum liner hoop stress for liner redesigns .....	39
Table 5 Maximum liner hoop stress for various degrees of elliptical out-of-roundness.....	40
Table 6 Dimensional parameters for Test Specimen #1.....	46
Table 7 Material properties for Test Specimen #1.....	47
Table 8 Comparison of LS-DYNA and shrink fit theory hoop and radial stress.....	48
Table 9 Dimensional parameters for Test Specimen #2.....	53
Table 10 Tolerances of Grade 2 (A+) gage blocks .....	56
Table 11 Dimensional parameters for Test Specimen #3.....	60
Table 12 Properties for new materials used in the ATLAS Generation II model .....	77
Table 13 Number of elements used in the ATLAS Generation II model.....	77
Table 14 Average stress magnitudes of compression ring elements on each interface .....	83
Table 15 Maximum radial separation between inner and outer cylinders in a composite liner $(\delta = 0.0008\text{in}, 20.32\mu\text{m})$ .....	89

## LIST OF FIGURES

Figure 1.1 Cross-section schematic of liner and glide planes (NTLX Shiva Star/ATLAS Configuration) .....	2
Figure 1.2 Directions of current flow, resulting magnetic field, and forces.....	6
Figure 1.3 Conductor motion in comparison to magnetic flux skin depth.....	7
Figure 1.4 Current flow between two conductors.....	10
Figure 2.1 ATLAS assembly illustrating partial shrink fits .....	12
Figure 2.2 Shrink fit assembly and extraction of mating cylinders .....	13
Figure 2.3 Outer cylinder radial displacement for shrink fit model (30 elements with 1 element through thickness) .....	16
Figure 2.4 Outer cylinder radial displacement for shrink fit models (30 elements with 1 element through thickness, and 4000 elements with 10 elements through thickness) ...	17
Figure 2.5 Convergence of radial displacement with an increasing number of elements....	18
Figure 2.6 Radial displacement for shrink fit model #2 with 2400 elements.....	19
Figure 2.7 Radial displacement for model #7 with 2400 elements.....	20
Figure 2.8 LS-DYNA mesh used for the ATLAS simulations.....	22
Figure 2.9 Glide plane temperature vs. time for preliminary ATLAS simulations .....	23
Figure 2.10 Zoomed view of liner radial displacement vectors .....	24
Figure 2.11 Full view of liner radial displacement vectors .....	25
Figure 2.12 Circular cylindrical shell with force ring applied on free end .....	26
Figure 2.13 Radial displacement of a cylinder subjected to a force ring on the free end ....	27
Figure 2.14 Radial displacement distribution along liner .....	28

Figure 2.15 Exaggerated curved liner geometry used to counteract radial deflections caused by the interference shrink fit .....	29
Figure 2.16 Post-assembly inner radius profile for original and curved liner designs .....	30
Figure 2.17 Locations of displacement specified upward motion .....	32
Figure 2.18 Time line for simulation involving vertical motion .....	32
Figure 3.1 Coordinates of liner and glide plane nodes for the Original Design located within the top interface .....	35
Figure 3.2 Liner feature redesigns in comparison with the original liner .....	36
Figure 3.3 Coordinates of liner and glide plane nodes for Liner Redesign #1 located within the top interface .....	37
Figure 3.4 Coordinates of liner and glide plane nodes for Liner Redesign #2 located within the top interface .....	37
Figure 3.5 Coordinates of liner and glide plane nodes for Liner Redesign #3 located within the top interface .....	38
Figure 3.6 Cross-sectional geometry of an elliptical out-of-round liner .....	40
Figure 3.7 Normalized graph of maximum hoop stress versus liner distortion .....	41
Figure 3.8 Finite element simulation of “pinch” loads on a thin-walled liner (a), and post-processor resultant displacement vectors (b) .....	42
Figure 3.9 Resulting maximum hoop stress due to increased “pinch” loads on a thin-walled liner .....	42
Figure 4.1 Test Specimen #1 after shrink fit assembly (left) and the corresponding axisymmetric finite element model (right) .....	47
Figure 4.2 Test Specimen #1 liner deflection due to a thermal shrink fit .....	49
Figure 4.3 Comparison of LS-DYNA (theoretical) and Test Specimen #1 (experimental) liner displacement values .....	50

Figure 4.4 Results of LS-DYNA simulation when modeled with less interference, in comparison to Test Specimen #1 liner displacement values .....	52
Figure 4.5 Apparatus used for measuring Test Specimen #2 components .....	54
Figure 4.6 Kinematic support used for test specimen measurements on the Zygō GPI Interferometer.....	57
Figure 4.7 Test Specimen #2 liner radial deflection values predicted by LS-DYNA.....	58
Figure 4.8 Comparison of LS-DYNA (theoretical) and Test Specimen #2 (experimental) liner displacement values.....	59
Figure 4.9 Schematic of an additional radial measurement technique.....	61
Figure 4.10 Diamond Turning Machine schematic (top view) for a centered tool used to machine Test Specimen #3 components.....	63
Figure 4.11 Zygō GPI Interferometer scan of a centering plug showing the ability of the software to automatically determine a tool's x-axis error in relation to the spindle centerline.....	65
Figure 4.12 Test Specimen #3 measured by the TalySurf Profilometer .....	67
Figure 4.13 Comparison of LS-DYNA (theoretical) and Test Specimen #3 (experimental) liner displacement values for one line of measurement.....	67
Figure 4.14 Comparison of LS-DYNA (theoretical) and Test Specimen #3 (experimental) liner displacement values for all three lines of measurement .....	68
Figure 4.15 Top view of the TalySurf Profilometer measuring a test specimen liner that is tilted in respect to the stylus motion, producing undesirable stylus drop-off.....	69
Figure 4.16 A schematic illustrating exaggerated TalySurf stylus drop-off .....	70
Figure 4.17 Test Specimen #3 surface profile before shrink fit .....	72
 Figure 5.1 Cross sectional drawing of ATLAS Generation II (Phase I).....	74
Figure 5.2 Zoomed view of ATLAS Generation II (Phase I).....	74
Figure 5.3 ATLAS Generation II finite element mesh (final design iteration) .....	76

Figure 5.4 Radial stress (x-stress) of liner/glide plane interface for ATLAS Generation II	79
Figure 5.5 Radial stress (x-stress) in the compression ring for ATLAS Generation II .....	81
Figure 5.6 Design changes suggested for the ring compressor's tooth geometry .....	82

Figure 6.1 Schematic of a composite liner, shown in configuration just prior to lockup .....	85
Figure 6.2 Schematic of a composite cylinder transition shape variation.....	87
Figure 6.3 Nodal coordinate locations after composite liner assembly for nodes falling along press fit interface ( $\delta= 0.0008\text{in}, 20.32\mu\text{m}$ ) .....	88
Figure 6.4 Radial deflection vectors for nodes on the inner and outer composite liner walls for Design #1 and Design #5 ( $\delta= 0.0008\text{in}, 20.32\mu\text{m}$ ).....	90
Figure 6.5 Radial deflection profiles for ID and OD of the inner and outer composite liner cylinders for Design #3 ( $\delta=0.0008\text{in}, 20.32\mu\text{m}$ ).....	91
Figure 6.6 Variation of maximum stress with each design ( $\delta= 0.0008\text{in}, 20.32\mu\text{m}$ ) .....	93
Figure 6.7 Maximum stress with a variation in radial interference (Design #3) .....	93

Figure A.1 Convergence of outer cylinder radial stress with an increasing number of elements .....	103
Figure A.2 Convergence of outer cylinder hoop stress with an increasing number of elements .....	103
Figure A.3 Outer cylinder radial stress distribution for shrink fit model #2 with 2400 elements .....	104
Figure A.4 Outer cylinder hoop stress distribution for shrink fit model #2 with 2400 elements .....	104
Figure A.5 Outer cylinder radial stress distribution for shrink fit model #7 with 2400 elements .....	105
Figure A.6 Outer cylinder radial stress distribution for shrink fit model #7 with 2400 elements .....	105

Figure A.7 Test Specimen #3 components fabricated using the ASG-2500 Diamond Turning Machine .....	106
Figure A.8 ATLAS Generation II glide plane/liner interface.....	106

## LIST OF SYMBOLS & ABBREVIATIONS

a	shrink fit inner radius of inner cylindrical component
$a_0$	speed of sound
b	shrink fit inner radius of outer cylindrical component
B	magnetic induction
c	shrink fit outer radius of outer cylindrical component
C	specific heat per unit volume
CMM	Coordinate Measuring Machine
d	parameter used in determining profilometer stylus drop-off
D	constant used in determining a radial deflection profile, $w(y)$
DTM	Diamond Turning Machine
E	elasticity of a material
$E_i$	shrink fit elasticity of inner cylindrical component
$E_o$	shrink fit elasticity of outer cylindrical component
$E_s$	electric field strength [V/m]
$f_\phi$	magnetic field characteristic constant
FEA	Finite Element Analysis
FG <sub>Readout</sub>	Federal gage readout
$F_{MF}$	compressional conductor force due to a magnetic field
h	parameter used in determining profilometer stylus drop-off
$h_{GB}$	gage block stack height
$h_s$	ASG-2500 DTM spindle centerline height above x-axis table
H	magnetic field strength [A/m]
in	inch (unit)
k	parameter used in determining profilometer stylus drop-off
kg	kilogram (unit)
km/s	kilometer per second (unit)
lb	pound (unit)
L	length of assembled composite liner
$L_E$	shrink fit inner cylinder extraction distance
$L_t$	length of radial taper for composite liner geometry
Lo	overall length of transition shape for composite liner geometry
mm	millimeter [ $m^{-3}$ ]
mm/min	millimeter per minute (unit)
m/s	meter per second (unit)
MA	megampere [ $A^6$ ]
Mbar	megabar [ $bar^6$ ]
MJ	megajoule [ $J^6$ ]
nm	nanometer [ $m^9$ ]
ns	nanosecond [ $s^9$ ]
N	Newton (unit)
p	shrink fit interface pressure

$p_m$	magnetic pressure
psi	pressure [lb/in <sup>2</sup> ]
P	pinch load applied to a thin-walled cylinder
PV	peak-to-valley
$Q_o$	cylindrical shell force ring magnitude
R	cylindrical shell nominal radius
$R_t$	radius of a diamond tool
s	second (unit)
$s_\phi$	magnetic flux skin depth
S	power flux density [W/m <sup>2</sup> ]
t	cylindrical shell thickness
$t_c$	critical time
T	Tesla (unit)
$T_{cond}$	conductor temperature
u	conduction motion speed
$(u_r)_{bo}$	shrink fit radial displacement for outer cylindrical component
$u_{vap}$	vapor propagation speed
w	width or circumference of current path
$w(y)$	radial deflection profile for a cylindrical shell on which a ring of force in the radial outward direction is imposed on the cylinder's end
W	Watt (unit)
$\alpha$	thermal expansion coefficient of a material
$\beta$	constant used in determining a radial deflection profile, $w(y)$
$\delta$	thermal shrink fit or mechanical press fit radial interference
$\delta^*$	varied radial interference for shrink fit out-of-roundness analysis
$\gamma$	specific heat ratio
$\eta$	electrical resistivity [ $\Omega\text{-m}$ ]
$\lambda$	test specimen tilt w.r.t. the motion of the TalySurf Profilometer stylus
$\mu$	magnetic permeability [H/m]
$\mu\text{in}$	microinch [in <sup>-6</sup> ]
$\mu\text{m}$	micrometer or micron [m <sup>-6</sup> ]
$\mu\text{s}$	microsecond [s <sup>-6</sup> ]
$\nu$	Poisson's ratio
$\nu_I$	shrink fit Poisson's ratio of inner cylindrical component
$\nu_o$	shrink fit Poisson's ratio of outer cylindrical component
$\Omega$	Ohm (unit)
$\theta$	characteristic temperature variable
$\rho$	mass density
$\sigma_{\text{nom}}$	nominal stress
$\sigma_{\text{max}}$	maximum stress
$\sigma_{rr}$	shrink fit radial stress (x-stress)

$\sigma_{YS}$	yield strength of a material
$\sigma_{\theta\theta}$	shrink fit hoop stress (z-stress)
$\tau$	sinusoidal current rise time

## 1.0 INTRODUCTION

There is a need to fabricate thin cylindrical components (called liners) for use in high-energy pulsed-power experiments at Los Alamos National Laboratories (LANL). The material, thickness, and shape of the liner are dictated by the physics experiments, and, as a result, the fabrication technique must be flexible. The base material for the liners is typically pure aluminum (commercial 1100 series) and the glide planes are copper. Early designs used a thermal shrink fit to assemble the liner and glide planes while the most recent designs use a mechanical press fit. It has also been proposed to employ composite liner structures, i.e., liners fabricated with nested cylindrical shells of dissimilar materials. The inner layer would normally be copper, but tantalum, stainless steel, or 6061 aluminum may be utilized.

These glide planes serve as a mechanism to transfer tremendous electrical currents ( $> 10\text{MA}$ ) to the liner, which leads to a cylindrical liner implosion. To optimize the results of these experiments, it is necessary for this cylindrical implosion to occur very uniformly. Therefore, manufacturing dimensionally precise liners with minimal surface flaws is essential. Unfortunately, the shrink fit process naturally results in residual stress and distortion in the liner walls, which need to be compensated. A schematic illustrating the assembly orientation of a single wall liner with glide planes is shown in Figure 1.1. The nominal diameter of the liner is 100mm, the height 59mm, the wall thickness 1.2954mm, and the nominal interference  $15.24\mu\text{m}$  (0.0006in).

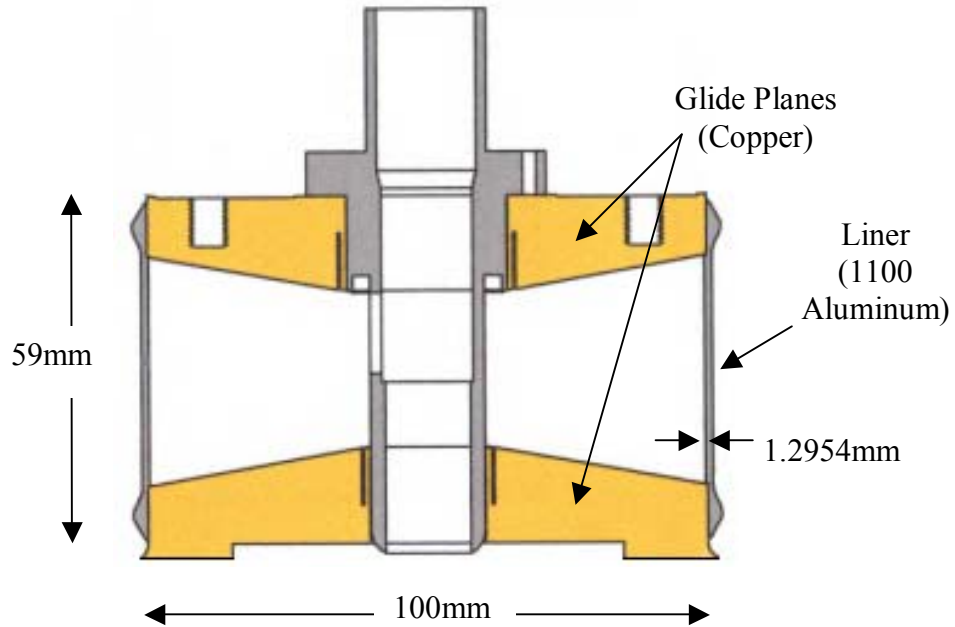


**Figure 1.1** Cross-section schematic of liner and glide planes (NTLX Shiva Star/ATLAS Configuration)

## 1.1 Pulsed-Power Technology

Pulsed-power technology involves the compression of energy in both time and space at levels not normally achievable by steady delivery of available power [1]. Traditional pulser systems utilize capacitive and inductive elements that temporarily store energy that is separated and then linked by switches to create shorter energy pulses. Extreme states of matter are created as a result of this tremendously dense concentration of energy. These temperatures can potentially achieve kilo-electron volt levels [2]. The creation of this matter can in turn be used for the study of material behavior, equations-of-state, and dynamic behavior [3]. The pulsed-power experiments use large radius, Z-pinch implosions of high atomic number plasmas to crush metal shells, or liners. The radial force created by this

working plasma is caused by axial current flow through the liners, which creates an azimuthal magnetic field in the radial direction. The result of the implosion is the creation of soft X-ray sources and the compression of magnetic flux, and conditions of very high pressure ( $>$  Mbar) and high speeds ( $>$  km/s) [1]. These implosions are followed by subsequent impact of the liners onto interior targets, driving strong shocks that have a variety of applications. It is important to note that these pulsed-power experiments have rise times associated with the build up of current on both the nanosecond and microsecond time scale, and selection of these rise times in conjunction with the geometry of mechanical components can effect the success of the experiments.

## 1.2 Background

In 1955, the use of pulsed-power, linear Z-pinch discharges was abandoned in quest for controlled thermonuclear fusion. However, the interest in these systems significantly increased for the purpose of space propulsion during the Space Age in 1963 [2]. Later at the Air Force Weapons Laboratory (AFWL) in 1971, P. J. Turchi and W.L. Baker proposed the idea of nuclear weapon effects simulations by using Z-pinch implosions of high atomic number plasma liners to generate multi-megajoule pulses of soft X-radiation [4]. This work inspired the development of the subsequent Shiva program at AFWL which concentrated on pulsed-power experiments with current rise times in the 50-100ns time regime, designed to power intense charged particle beams [2]. A discussion on the determination of current rise times can be found in latter seconds of this paper. The Shiva experiment led to the

production of a megajoule of soft X-radiation from the use of the Shiva Star capacitor bank (at 5MJ and 12MA) in conjunction with the so-called Plasma Flow Switch, which uses a plasma discharge. This discharge was combined with output pulses of a few microseconds, which is relatively slow but energy rich, and the result was a plasma liner imploding in a few hundred nanoseconds [2]. Today, work continues on the creation of soft X-radiation via the Z-pinch implosion of plasma liners at Sandia National Laboratories on the Z-machine. Pulses in the 50-100ns time regime have been used for this system, but longer implosion times of >200ns are now being used to reduce costs of future systems of higher energy [2].

### **1.3 Pulsed-Power Experiment Design Criteria**

There are many factors that need to be taken into consideration when designing the components and establishing the parameters necessary for conducting pulsed-power experiments. If these design criteria are not considered or determined properly, the experiments can potentially be extremely dangerous and possibly fatal. Peter J. Turchi, in his paper entitled “Problems and Prospects for Microsecond Pulsed Power Above Ten Megamperes” [2], explains the process and calculations involved in organizing and designing successful pulsed-power experiments. This section describes the pertinent issues at hand according to Turchi.

### 1.3.1 Current Rise Time Determination

Issues of cost and technical risk are evident when discussing distinctions between pulsers that produce energy in times of microseconds versus those that operate in the nanosecond regime. The latter family of pulsed-power systems operates at much higher voltages and can therefore achieve high currents in shorter time periods. Typically multi-megavolt systems, which correspond to systems operating in the nanosecond time regime, can cost upward of \$5-\$10 per joule of output energy. Conversely, microsecond systems that operate at tens of kilovolts can often cost less than \$1 per joule. Such a discrepancy in cost can potentially mean tens of millions of dollars, since energy outputs are typically on the megajoule scale. The combination of cost reduction and higher safety has encouraged programs to attempt development of systems that operate with rise times on the order of a few microseconds. The power flux density,  $S$ , with units of  $\text{W/m}^2$ , is given by the equation,

$$S = E_s \times H \quad (1)$$

where  $E_s$  is the electric field strength [ $\text{V/m}$ ] and  $H$  is the magnetic field strength [ $\text{A/m}$ ]. Of course, offsetting the reduction of the electric field strength (which is beneficial for the previously described reasons) requires an increase in the magnetic field strength in order to maintain an equivalent power flux density. Although the option to increase the magnetic field strength results in safer and more cost efficient pulsed-power experiments, there are many problems associated with this alternative. Large magnetic fields result from high currents being carried in a path with a relatively small width or circumference, and resistive heating and conductor motion (i.e., motion of any component carrying an electric current)

are often side effects of such high current densities. Conductor motion can often reach a magnitude that can interfere with electrical processes and current flow, which can be particularly troublesome in the microsecond time regime of pulsed-power experiments. Figure 1.2 shows the direction of current flow in relation to the liner and glide plane orientation. The result is a magnetic field around the liner and forces acting radially inward, which essentially implodes the liner.

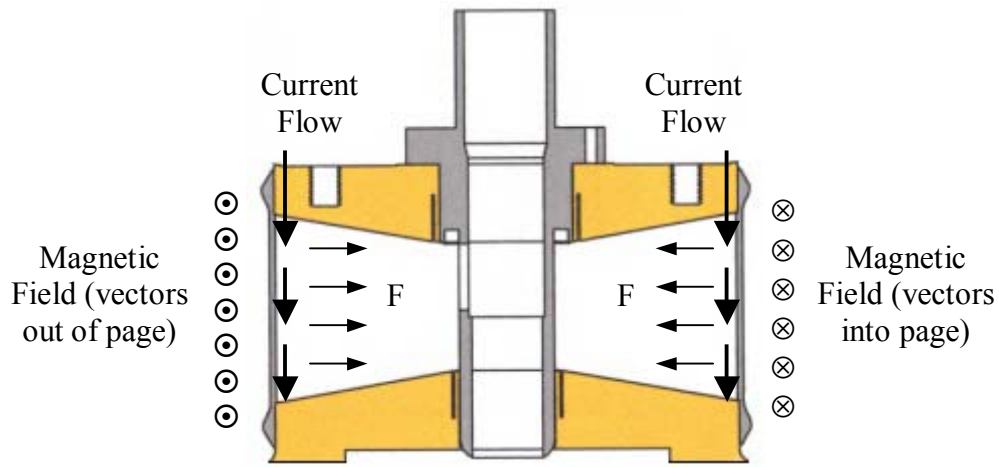


**Figure 1.2** Directions of current flow, resulting magnetic field, and forces

### 1.3.2 Conductor Motion

It is important to note that magnetic fields have forces associated with them, and these force densities act as a pressure,  $p_m$  [Pa], on the conductor surfaces, given by the equation

$$p_m = \frac{B^2}{2\mu} \quad (2)$$

where  $B$  is magnetic induction [T] and  $\mu$  is the magnetic permeability [H/m]. This pressure, which is applied during the fast-rising pulse, causes material motion by driving a compression wave into the conductor. This motion,  $u$  [m/s], is given by the equation

$$u = \frac{B^2}{2\mu\rho a_o} \quad (3)$$

where  $\rho$  is the mass density of the conductor material [ $\text{kg}/\text{m}^3$ ] and  $a_o$  is the speed of sound [ $\text{m}/\text{s}$ ]. The conductor motion is constant for a non-varying magnetic field of any magnitude, and thus the displacement of the conductor surface increases linearly with time. This motion can potentially be problematic because after a given period of time, the magnetic field can force conductor plates apart at a distance that exceeds the size of the magnetic field, thus ceasing conductivity through the circuit. Therefore, it is important to investigate the magnetic flux skin depth,  $s_\phi$  [m], which is essentially the size of the magnetic field. This quantity is given by the equation

$$s_\phi = f_\phi \sqrt{\frac{\eta\tau}{\mu}} \quad (4)$$

where  $\eta$  is the electrical resistivity [ $\Omega\cdot\text{m}$ ] and  $\tau$  is the current rise time [s]. The constant  $f_\phi$  depends on the variation of a given magnetic field in a vacuum, and is tabulated for various rise times. The general trend of the magnetic flux skin depth in comparison to the conductor motion is shown in Figure 1.3.

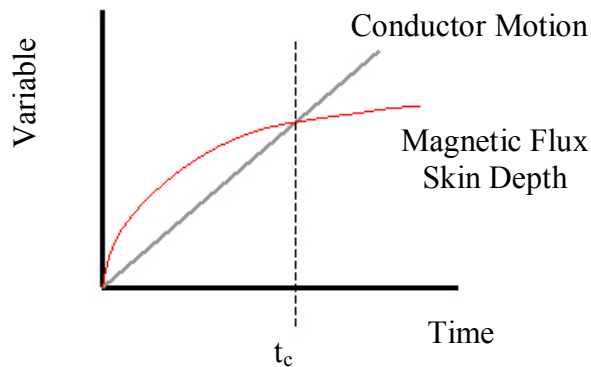


**Figure 1.3** Conductor motion in comparison to magnetic flux skin depth

It is obvious that after a certain time, the conductor motion exceeds the magnetic flux skin depth, meaning the conductor plates will separate to a distance such that conductivity through the two given conducting components will terminate. This critical time  $t_c$  is given by the equation:

$$t_c = \left( \frac{\eta}{\mu} \right) \left[ \frac{\rho a_o}{p_m} \right]^2 \quad (5)$$

The critical time is important to take into consideration as it can define the necessary rise times for certain system parameters. For example, at 50T this critical time is about  $16.7\mu\text{s}$  for copper and  $6.8\mu\text{s}$  for aluminum; for such a system, rise times of less than  $6.8\mu\text{s}$  would be highly desirable in order to avoid conductivity challenges.

### 1.3.3 Contact Design

The magnetic field's potential ability to separate conductor plates is a concern, as this can result in loss of conductivity between two components. There is a force  $F_{MF}$  [N] associated with the magnetic field separating conductors by overcoming the compressional stresses that hold the components in contact, and it is given by

$$F_{MF} = \left( \frac{B^2}{2\mu} \right) [3s_\phi w] \quad (6)$$

where  $w$  is the width or circumference of the current path [m]. Creating a robust system that can overcome these forces is important in design, and can usually be accomplished by simple arrangements in which adjacent conductors are bolted together, as shown in Figure 1.4. Press and shrink fit assemblies can be used as mechanisms to maintain contact as well.

#### 1.3.4 Thermal Difficulties

For conducting elements that have thickness and surface curvature radii that are considerably larger than the magnetic flux skin depth, the temperature  $T_{cond}$  [°C] scales according to the following equation:

$$T_{cond} = \frac{\theta B^2}{2\mu C} \quad (7)$$

In this equation,  $C$  is the specific heat per unit volume of the given material, and  $\theta$  is a dimensionless variable that has been tabulated for several time variations of the magnetic field application to the system (the selection of this factor is the value that corresponds to the rise time of the system). This temperature rise can be so significant that a phase change on of conductor surfaces can occur, thus complicating quantitative analysis. Additionally, current concentrations can increase the conductor temperature even further and therefore must be taken into consideration.

#### 1.3.5 Current Concentrations

At a region where a conductor surface (and therefore current path) changes direction, it is common for the local current density to greatly exceed that of the current flowing in a flat surface. An example of a typical current direction change seen at a concave corner is pictured in Figure 1.4.

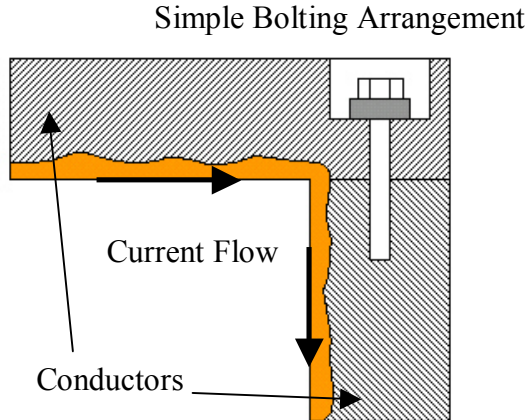


**Figure 1.4** Current flow between two conductors

If the configuration shown consisted of only one conductor with a similar current flow direction change, it would be useful to provide a radius of curvature that significantly exceeds the magnetic flux skin depth. Such a radius would prevent possible current concentration at that location. In addition, local imperfections can lead to current concentration. A phenomenon known as “magnetic sawing” occurs when current is forced to flow around surface nicks and gaps, thus calling for highly smooth surface finishes on all conducting surfaces.

### 1.3.6 Vapor Production

With an increase in temperature, even without a change of state, vapors can form on the conductor surface, thus interfering with current flow between transmission plates. This vapor can create pressures that tend to separate conductor surfaces, but more important is the speed at which the leading edge of this vapor can propagate through the system. This velocity  $u_{vap}$  [m/s] is given by

$$u_{vap} = \frac{2a_o}{\gamma - 1} \quad (8)$$

where  $\gamma$  is the ratio of specific heats between the vapor and the conductor material. Again, the distinction between operation in the microsecond and nanosecond time regimes becomes critical. Very short pulses may not allow sufficient time for the vapor to interfere with the current flow and cause electrical breakdown, depending on the speed of the vapor. Hence, pulse time parameters are often established at a level such that vapor propagation is not a problem.

## 2.0 FINITE ELEMENT MODELING

### 2.1 Standard Shrink Fit Modeling

For the current problem, the stresses and distortions resulting from slipping the glide planes into the liner would be impossible to calculate from analytical shrink fit formulas. These expressions exist for cylindrical systems in which the interference occurs along the entire length of the mating cylinders. In the ATLAS configuration, however, only a partial interference exists, since the glide planes only fit into the end portions of the liner, as shown in Figure 2.1.

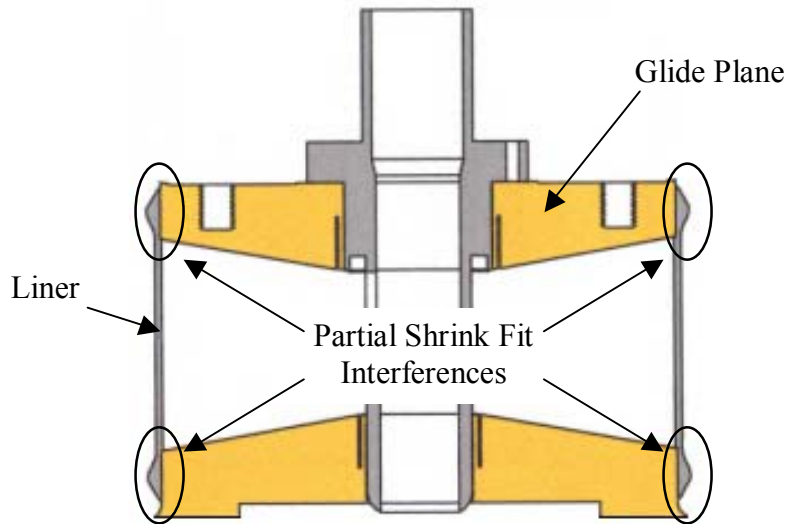


**Figure 2.1** ATLAS assembly illustrating partial shrink fits

Finite element analysis (FEA) provided an efficient method to determine whether standard shrink fit calculations corresponded to the actual response of such a system in which a partial shrink fit is entailed. A shrink fit assembly consisting of two cylindrical components

(of the same axial length) was created using LS-DYNA, a powerful FEA software package that was used for all simulations discussed in this thesis. Initially, models were constructed in which the two components' free ends were aligned with one another, and subsequent models were created in which the inner cylinder was incrementally extracted in the axial direction, as shown in Figure 2.2. The inner and outer cylinders were composed of copper and 1100 series aluminum, respectively.

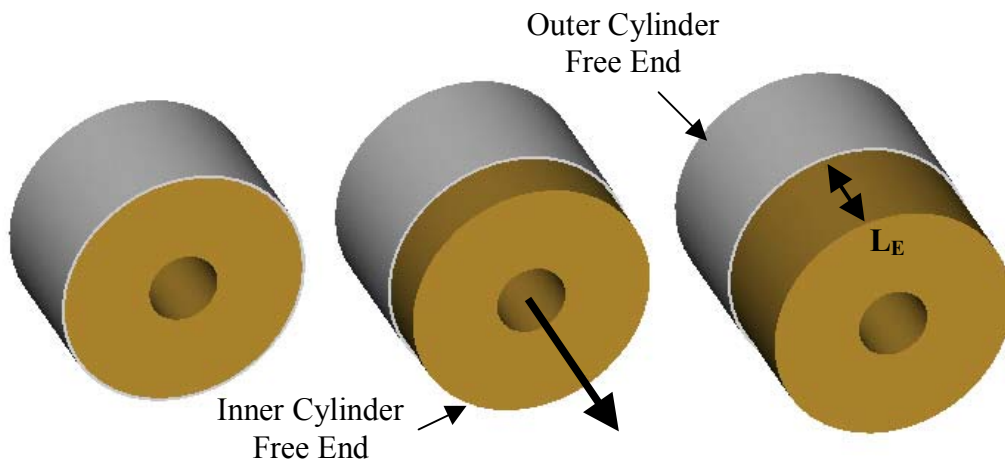


**Figure 2.2** Shrink fit assembly and extraction of mating cylinders

The thought behind this sequence of static simulations was to determine at what point, if any, the model results deviated from selected parameters calculated from analytical formulas. The wall thickness of the outer and inner cylinders was set at values that corresponded to the dimensions of the actual ATLAS liner and glide planes respectively (see Table 1). Both lengths were equivalent to the ATLAS liner length, and the shrink fit radial interference magnitude matched as well.

**Table 1** Shrink fit model dimension parameters

	<b>OD</b>	<b>ID</b>	<b>Thickness</b>	<b>Length</b>
<b>Outer Cylinder</b>	100.59mm (3.9602in)	97.99mm (3.8582in)	1.30mm (0.0510in)	58.98mm (2.3222in)
<b>Inner Cylinder</b>	98.03mm (3.8594in)	28.14mm (1.1080in)	34.94mm (1.3757in)	58.98mm (2.3222in)
<b>Radial Interference:</b> 15.24 $\mu\text{m}$ (0.0006in)				

Although not all pictured in Figure 2.2, there were seven static simulations performed in all. With each successive model, the sole difference occurred in the varying parameter  $L_E$ , which represented the extraction distance of the inner cylinder. The inner cylinder extraction resulted in an increasing length of the free, non-supported end of the outer thin-walled cylinder. Hence, the percentage of the outer cylinder length that remained in contact with its mating inner cylinder decreased with each successive model, as summarized in Table 2.

**Table 2** Shrink fit model contact parameters

	<b>Model Number</b>						
	# 1	# 2	# 3	# 4	# 5	# 6	# 7
<b><math>L_E</math> (mm)</b>	0.000	8.245	16.490	24.735	32.980	41.225	49.470
<b>% in contact</b>	100%	86%	72%	58%	44%	30%	16%

For model #7, it is important to note that the contact length between the two cylinders was 9.507mm (0.3743in), which corresponds to the actual contact length in the ATLAS configuration.

The three parameters that were examined included radial displacement, radial stress, and hoop stress, according to shrink fit theory formulas represented by Equations 9, 10, and 11, respectively [5]. Each parameter was calculated at the inner radius of the outer cylinder, i.e. at the interface.

$$(u_r)_{bo} = \frac{bp}{E_o} \left[ \frac{c^2 + b^2}{c^2 - b^2} + v_o \right] \quad (9)$$

$$\sigma_{rr} = -\frac{\delta}{b \left[ \frac{1}{E_o} \left( \frac{c^2 + b^2}{c^2 - b^2} + v_o \right) + \frac{1}{E_i} \left( \frac{b^2 + a^2}{b^2 - a^2} - v_i \right) \right]} \quad (10)$$

$$\sigma_{\theta\theta} = p \left( \frac{c^2 + b^2}{c^2 - b^2} \right) \quad (11)$$

The parameter  $a$  is the inner radius of the internal copper cylinder, and the parameters  $b$  and  $c$  are the inner and outer radii of the thin-walled aluminum cylinder. The material properties were set as follows:  $E_i = 15.95 \times 10^6$  psi,  $E_o = 10.01 \times 10^6$  psi,  $v_i = 0.35$ , and  $v_o = 0.33$ . Also, the interface pressure value  $p$  is simply the negative radial stress,  $\sigma_{rr}$ .

### 2.1.1 Number of Elements and Convergence

The finite element model was constructed in LS-DYNA using the aforementioned parameters and a randomly selected number of elements for the outer cylinder, and the radial displacement along the entire length was first plotted, as shown in Figure 2.3. This outer cylinder was composed of 30 elements, with a 1-element thickness.

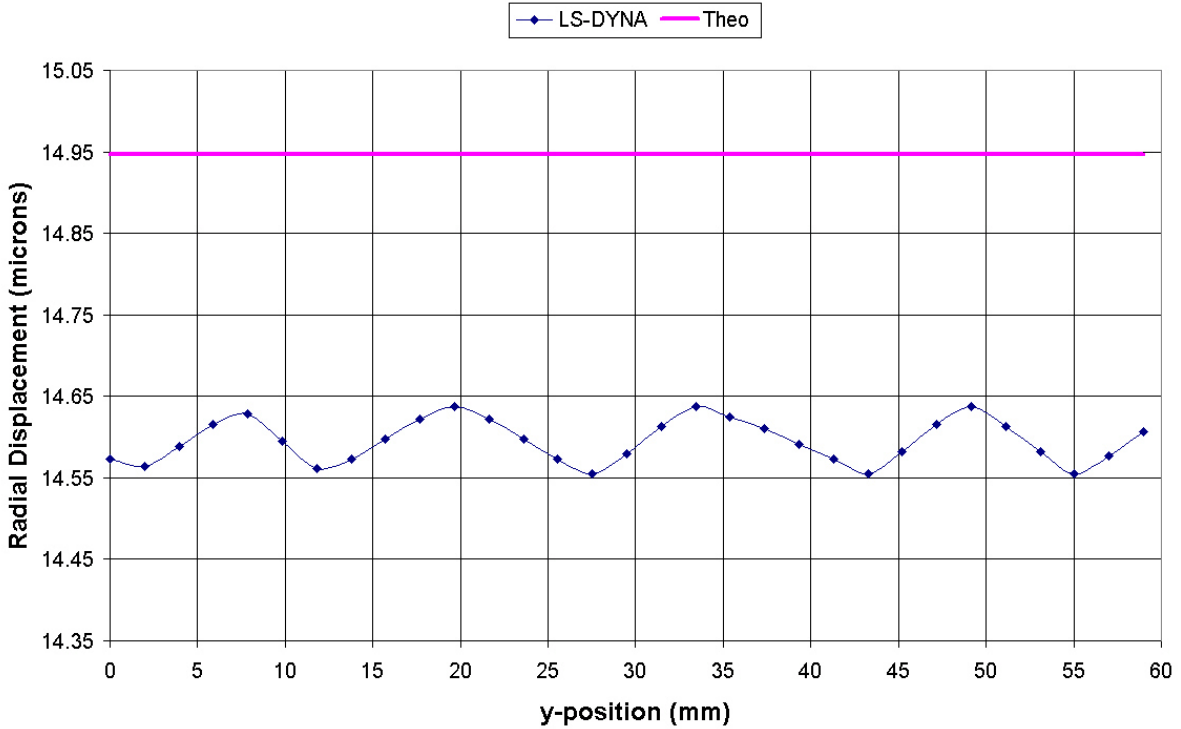


**Figure 2.3** Outer cylinder radial displacement for shrink fit model (30 elements with 1 element through thickness)

The two main concerns with this plot are the fluctuation in the radial deflection value according to LS-DYNA, and the difference between this plot's nominal value when compared to the theoretical value. Although the fluctuation is only 100nm and the percent difference is only 2.3%, it was believed that increasing the number of elements in the outer cylindrical component would improve these results. Thus, new models were constructed with an increased number of elements, and the results were plotted. Figure 2.4 shows the radial displacement for an outer cylinder with 4000 elements (10 elements through thickness) in comparison to the original plot shown in Figure 2.3.

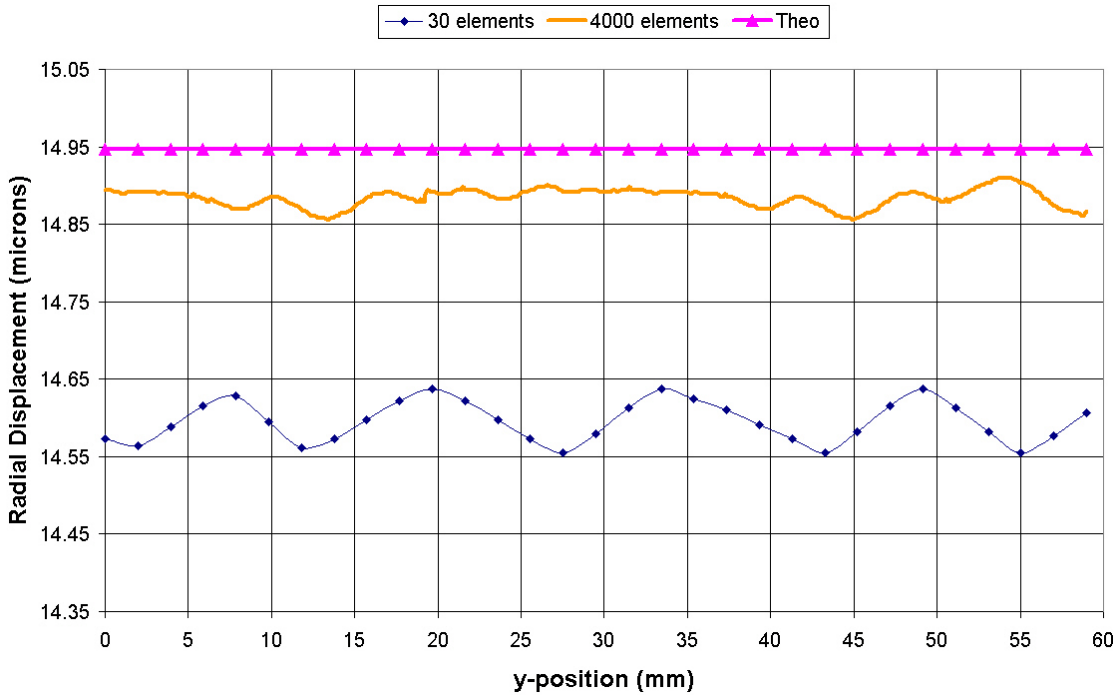


**Figure 2.4** Outer cylinder radial displacement for shrink fit models (30 elements with 1 element through thickness, and 4000 elements with 10 elements through thickness)

By increasing the number of elements in the outer cylinder, the fluctuation was reduced by 50% (peak-to-valley of approximately 50nm) and the nominal value more closely resembles the value predicted by shrink fit theory (percent difference of 0.3%). For various numbers of elements, the convergence in the radial displacement values is shown in Figure 2.5.

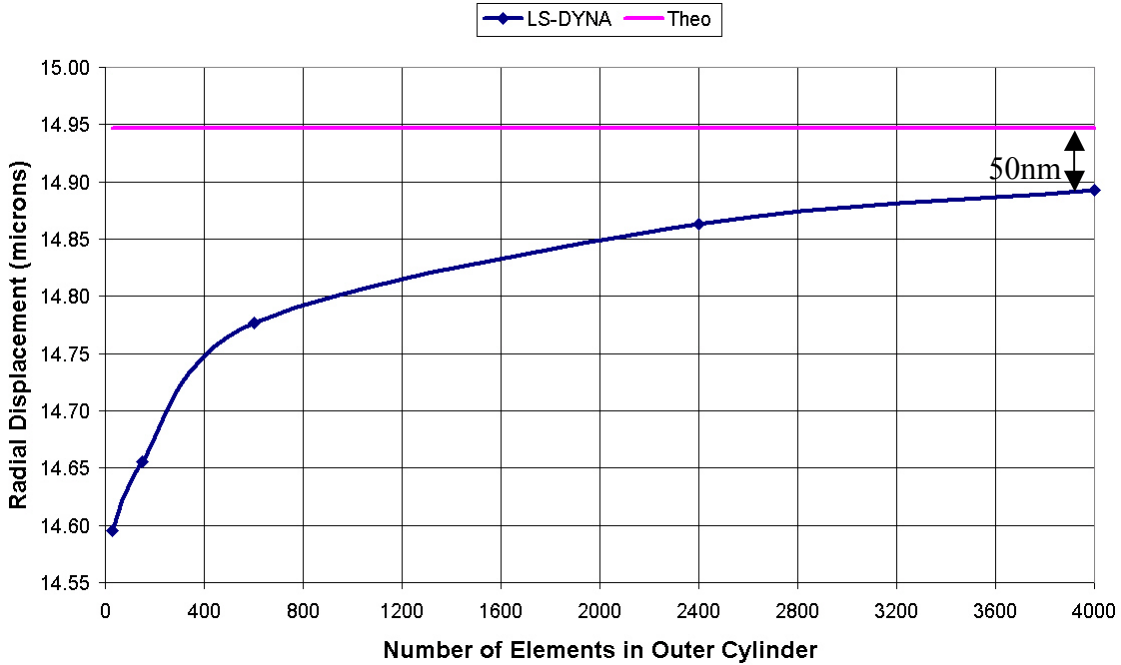


**Figure 2.5** Convergence of radial displacement with an increasing number of elements

For radial stress and hoop stress, similar convergence plots were produced and can be found in the Appendix in Figures A.1 and A.2, respectively. From these results, it is evident that using a large number of elements is beneficial in terms of the three pertinent parameters being investigated. For each successive simulation in which the inner cylinder was extracted, using 2400 elements was deemed sufficient for obtaining accurate model results.

## 2.2 Partial Shrink Fit Modeling

For model #2, the inner cylinder was extracted a distance of 8.245mm, and the static results were plotted. Figure 2.6 shows the distribution of radial displacement for the outer cylinder.

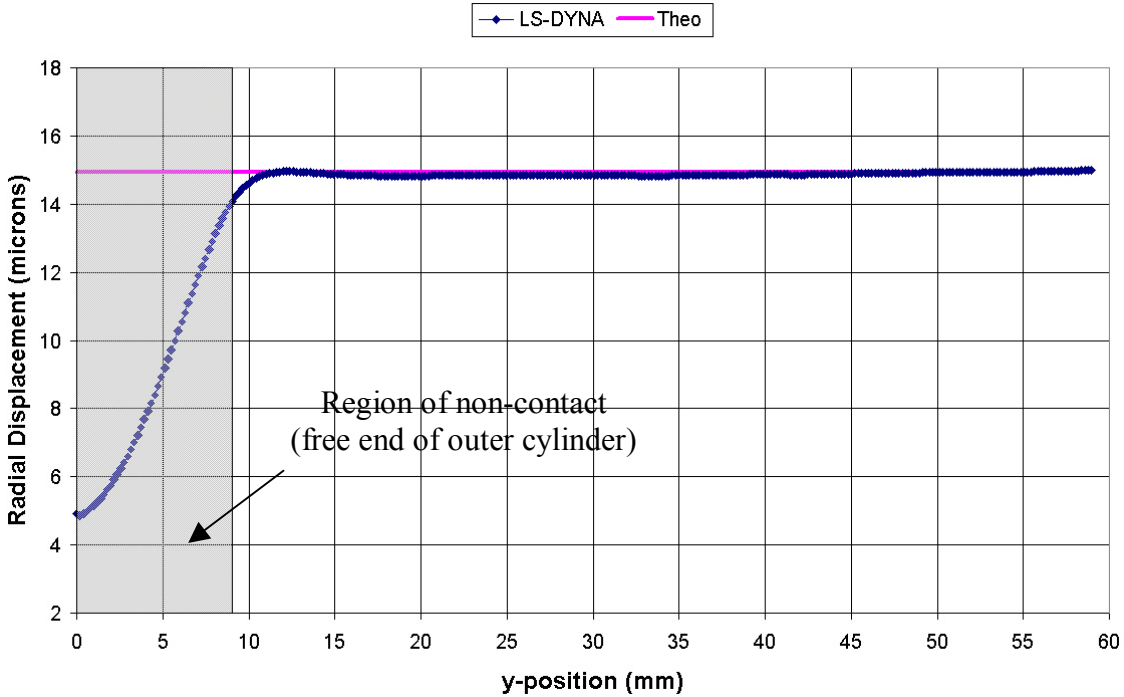


**Figure 2.6** Radial displacement for shrink fit model #2 with 2400 elements

As expected, the displacement plot drops off significantly at the region in which the outer cylinder is not supported by its mating component (since the inner cylinder has been slightly extracted). For this same model, the distributions of both radial stress and hoop stress can be seen in the Appendix in Figures A.3 and A.4, respectively. The edge of the inner cylinder against the ID of the outer cylinder acts as a radial direction stress riser, thus explaining the spike in the radial stress plot. The hoop stress trend corresponds with that of radial displacement as expected, because radial displacement or “stretch” directly affects hoop stress (and the equations for these parameters are proportional as seen in Equations 9 and 11).

Model #7 is of particular interest, since the contact length of approximately 9.5mm equals that of the interfaces found in the ATLAS prototype. The radial displacement for the outer cylinder in this model is shown in Figure 2.7.

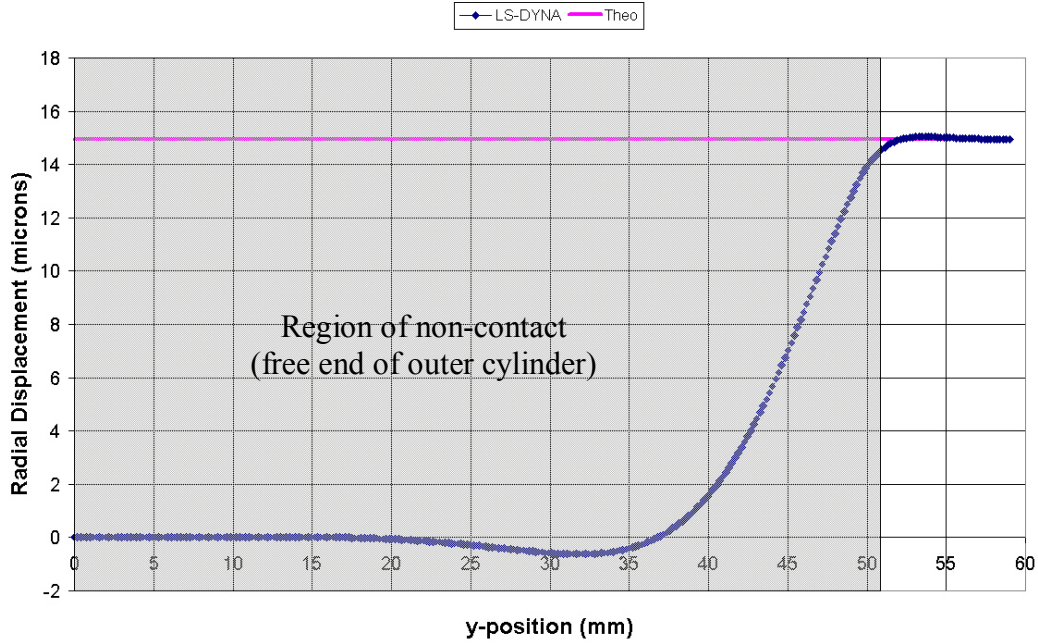


**Figure 2.7** Radial displacement for model #7 with 2400 elements

The outer cylinder maintains the theoretical radial displacement value in the small region in which it contacts its mating inner cylinder (on the right portion of the plot). The displacement in the non-contact region of this cylinder, however, does not correspond to displacement according to shrink fit theory, as expected. In fact, negative displacement (i.e., towards the cylinders' centerline) occurs in the middle portion of the overall length, a phenomenon that is discussed in the following chapter of this thesis. The radial stress and hoop stress distributions for this particular model can again be found in the Appendix (Figures A.5 and A.6). It is obvious that when investigating the entire length of the liner, the

stresses and distortions that result from slipping the glide planes into the end portions would indeed be impossible to predict using analytical formulas and shrink fit theory. Therefore, finite element analysis was used as a tool for analyzing the liner and other surrounding components in the ATLAS pulsed-power system.

## 2.3 Finite Element Analysis of ATLAS

### 2.3.1 Geometry and Material Properties

The geometry of this particular shrink fit interface, as well as the geometry of the actual liner itself, was expected to provide results that considerably deviate from those given by standard shrink fit calculations. LS-DYNA, a powerful FEA software package, was used to model the ATLAS prototype; this axisymmetric system can be seen in Figure 2.8. A sample code taken from an ATLAS simulation is shown in Appendix B. The axisymmetric modeling does ignore some details of the glide planes such as holes and ports, but this is not expected to impact the results of interest in any significant way.

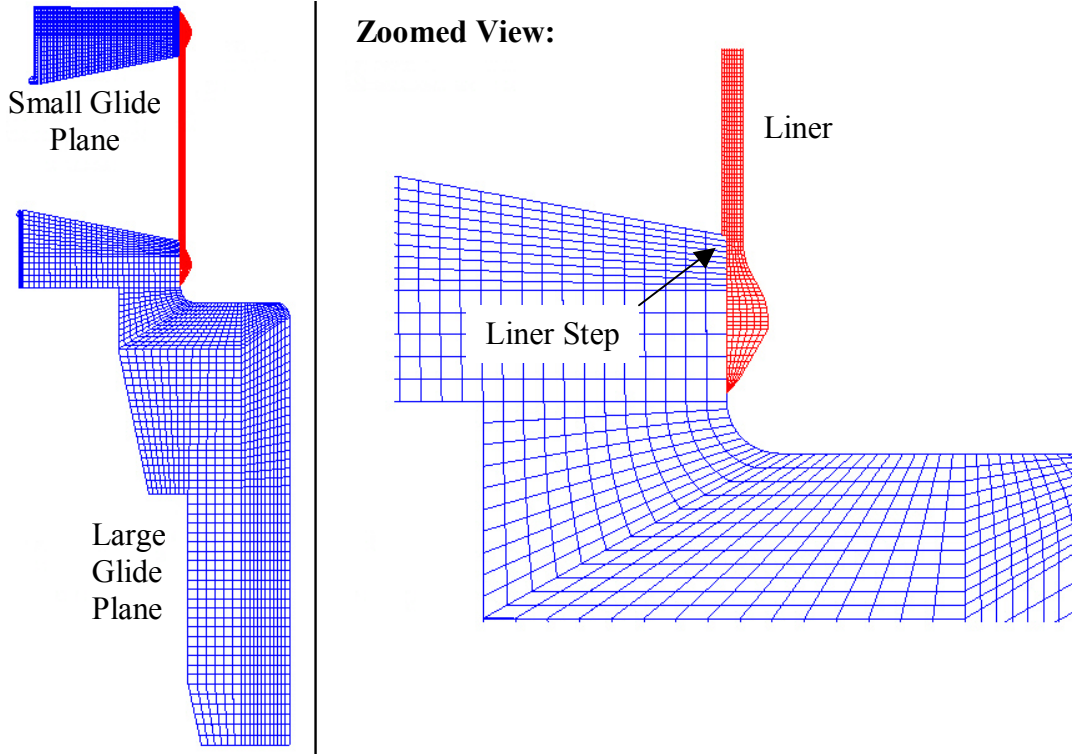


**Figure 2.8** LS-DYNA mesh used for the ATLAS simulations

The material properties used for the liner and both glide planes correspond to 1100 aluminum and copper, respectively. These properties are listed in Table 3.

**Table 3** Material properties used in ATLAS simulations

	<b>Copper Glide Planes</b>	<b>1100 Aluminum Liner</b>
Young's Modulus	$1.5954 \times 10^7$ psi	$1.0008 \times 10^7$ psi
Poisson's Ratio	0.35	0.33
Thermal Expansion Coefficient	$1.70 \times 10^{-5} (\text{ }^\circ\text{C})^{-1}$	$2.36 \times 10^{-5} (\text{ }^\circ\text{C})^{-1}$
Yield Strength	50,000 psi	5,000 psi

Each component was modeled in LS-DYNA as an elastic-plastic material, accounting for any potential yielding. Selecting the number of elements was based on results discussed in

Section 2.1.1 in this thesis. It was previously determined that shrink fit simulations involving thin walled cylinders with 8 elements through the thickness provided reliable, accurate results. Hence, the liner was composed of 1938 elements (with 8 elements through the thickness), and the large and small glide planes were composed of approximately 2000 elements each. For this preliminary FEA model in particular, a composite liner was *not* used.

### 2.3.2 Thermal Shrink Fit Assembly

Using 100 implicit pseudo-time steps, a uniform temperature change of  $-200^{\circ}\text{C}$  was imposed on the glide planes during the simulation. This temperature drop represented the effect of using liquid nitrogen to shrink the glide planes (which is used in the actual assembly process at LANL). The result of this glide plane temperature change was a reduction in radius sufficient enough to overcome the radial interference value of  $15.24\mu\text{m}$ . The parts were then slipped together, followed by a return to ambient temperature with the “contact modeling” between the parts activated during the transition to equilibrium, as shown in Figure 2.9.

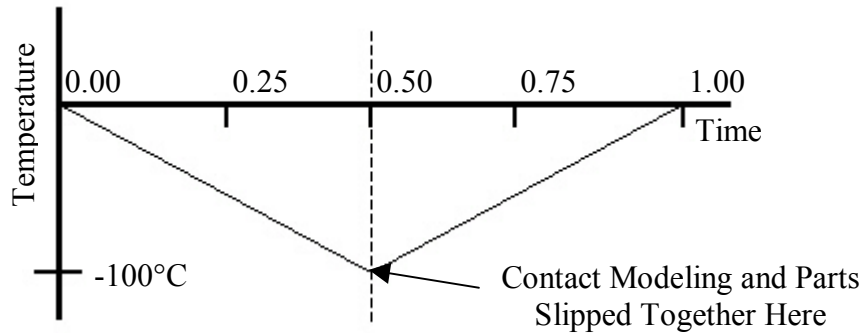


**Figure 2.9** Glide plane temperature vs. time for preliminary ATLAS simulations

### 2.3.3 Radial Deflection Results

While the glide planes expanded during the temperature rise phase, the liner deformed in the radial direction. A zoomed displacement vector plot for nodes within the liner is shown in Figure 2.10, and the overall displacement trend of these vectors can be seen in Figure 2.11. Note that the fringe levels are listed in units of inches. The maximum radial deflection experienced by the liner was  $5.958 \times 10^{-4}$  in or  $15.13\mu\text{m}$ .

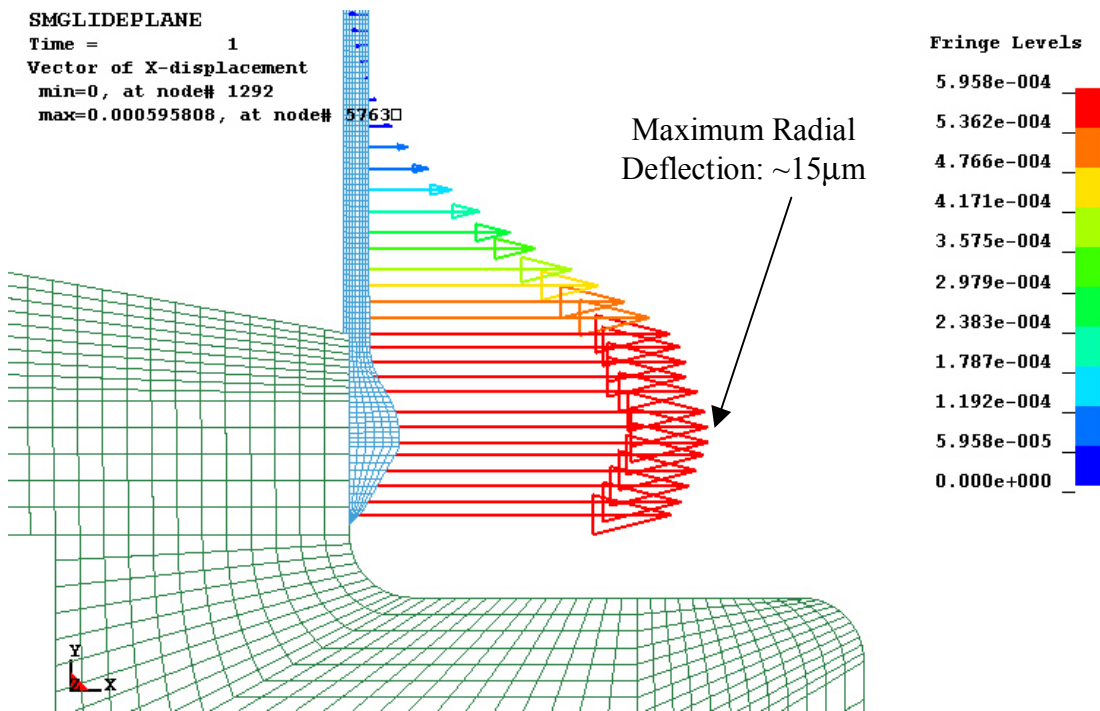


**Figure 2.10** Zoomed view of liner radial displacement vectors

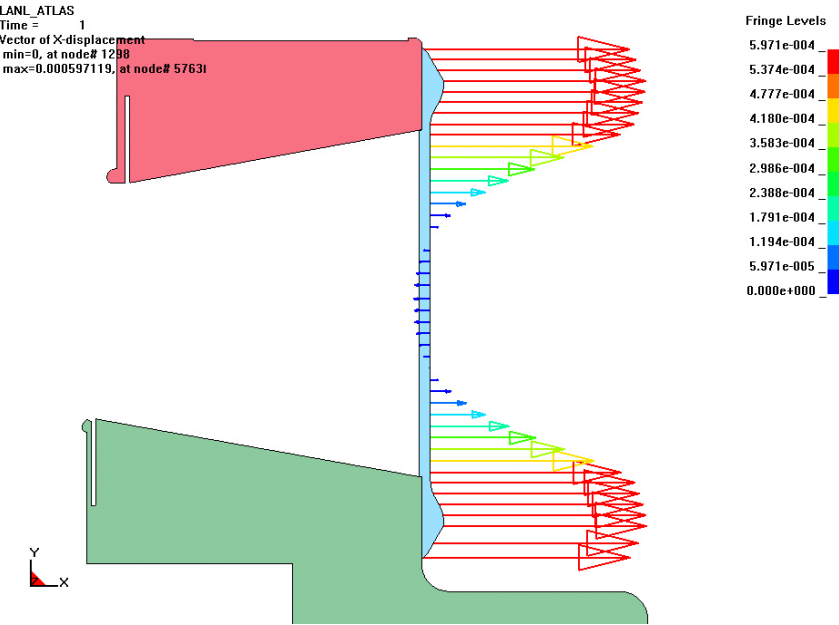


**Figure 2.11** Full view of liner radial displacement vectors

The lengths of the arrows indicate magnitude of radial displacement in the liner wall, with peak deflections occurring at either end of the liner. Note that the vectors are magnified for an enhanced visual representation of the displacement behavior. The displacement decays with distance from the liner ends and actually becomes negative, indicating inward radial movement at the mid-length position of the liner.

This negative displacement does not seem intuitively sound, since all force and pressure vectors imposed on the liner act radially outward in the positive x-direction. Further investigation, however, shows that these results are to be expected. In Timoshenko's book entitled "Theory of Plates and Shells" [6], an analysis can be found involving a circular cylindrical shell on which a ring of radial outward force is imposed at the cylinder's boundary end, as shown in Figure 2.12.

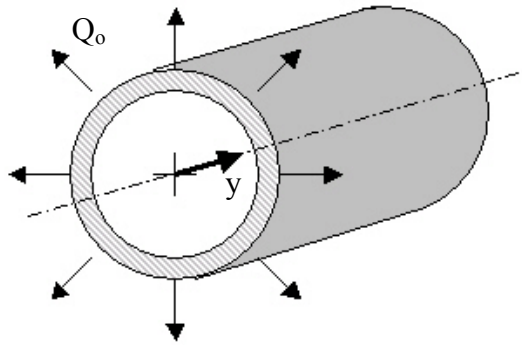


**Figure 2.12** Circular cylindrical shell with force ring applied on free end

Using the following three equations, the radial deflection profile,  $w(y)$ , of any cylindrical shell can be determined.

$$\beta = \left[ \frac{3(1-v^2)}{R^2 t^2} \right]^{1/4} \quad (12)$$

$$D = \frac{Et^3}{12(1-v^3)} \quad (13)$$

$$w(y) = -\frac{1}{2\beta^3 D} [Q_o (e^{-\beta y}) \cos(\beta y)] \quad (14)$$

The variable  $y$  is the axial distance from the applied force ring, with  $y=0$  representing the cylinder's free end. Using 1100 aluminum material properties, dimensional values representative of the ATLAS liner (nominal radius  $R=49.647\text{mm}$  and thickness  $t=1.2954\text{mm}$ ), and an arbitrary force magnitude  $Q_o$  of unity, a radial deflection plot was produced as shown in Figure 2.13.

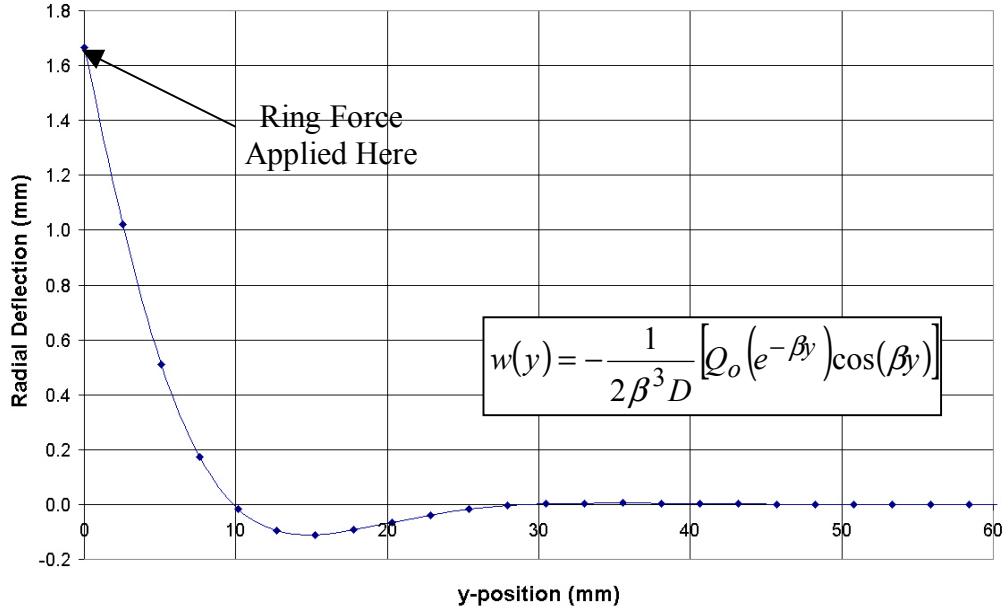


**Figure 2.13** Radial displacement of a cylinder subjected to a force ring on the free end

Of course, the deflection plot is a maximum at the point of force application, but becomes negative within close proximity to the cylinder's free end. Further down the cylinder's axial length, the radial deflection magnitude fluctuates between positive and negative values, following an exponentially decaying trend. Thus, the liner's region of negative radial deflection seen in Figure 2.11 is explained, since the loading is somewhat synonymous to this scenario described by Timoshenko [6]. The parabolic radial deflection profile seen in the liner occurs due to the combined effects of loading on *both* ends of this relatively short cylinder.

Figure 2.14 is a graph showing the distribution of radial displacement along the liner wall. The flat sections on the left and right extremities of this graph represent liner displacements

in the regions of contact with the large and small glide planes, respectively. In these end regions, the displacement magnitude ( $15.12\mu\text{m}$ ) closely matches that of the radial interference parameter ( $15.24\mu\text{m}$ ). Positive values represent liner displacements radially outward, while negative values represent displacements radially inward; note again that the liner undergoes negative radial displacement in the mid-length position of the liner.

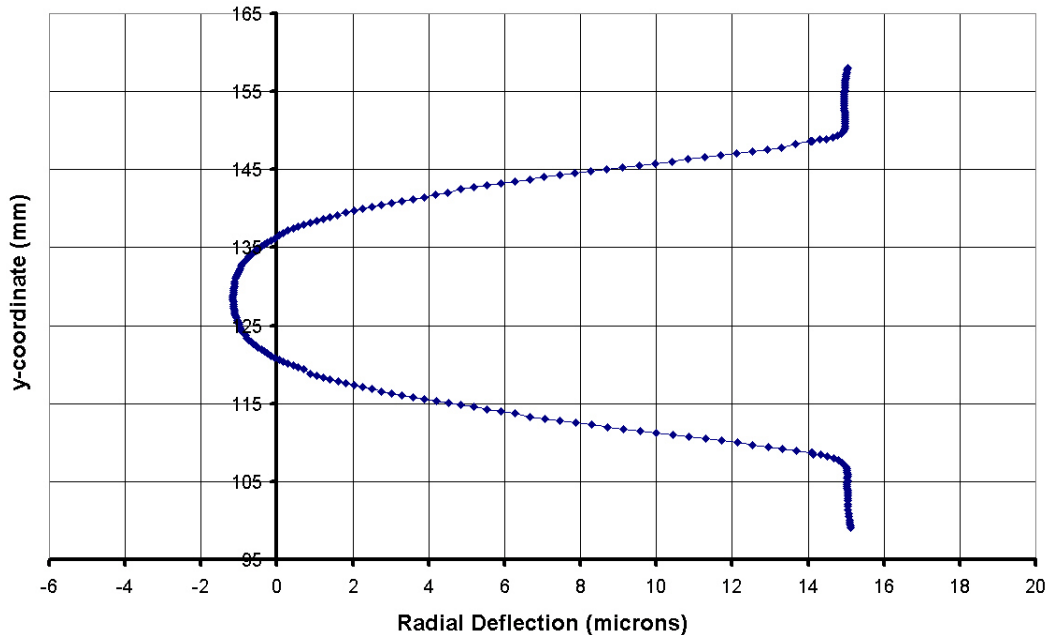


**Figure 2.14** Radial displacement distribution along liner

There is a stress concentration in the liner near the regions in which contact ends with the glide planes, mainly caused by the sharp corner of the glide planes in these regions. The maximum hoop and radial stress values in the liner were 4180psi and 508psi, respectively. Since the yield strength of 1100 aluminum is approximately 5000psi, yielding and permanent distortion of the liner were not expected.

#### 2.3.4 Radial Deflection Compensation

To improve the cylindrical implosion of the liner, it is surmised that having a uniform, straight walled cylinder *after* the shrink fit process is desirable. Therefore, the deflections caused by the interference, shown in Figures 2.10 and Figure 2.11, are potentially problematic. To implement the idea of creating a straight walled liner after the shrink fit process, a liner fabricated with pre-assembly shape variation was proposed. This variation would represent the negative of the calculated deflection magnitude along the liner length, which would expectantly result in a final shape after assembly that “counteracts” the deflections caused by the interference fit. An exaggerated representation of such a geometry is illustrated in Figure 2.15.

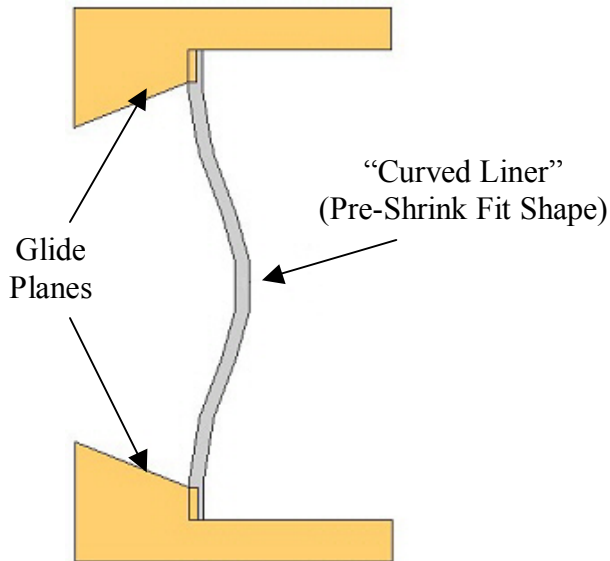


**Figure 2.15** Exaggerated curved liner geometry used to counteract radial deflections caused by the interference shrink fit

One such liner was simulated using FEA, and the results are shown in Figure 2.16 with a comparison to the original liner design.

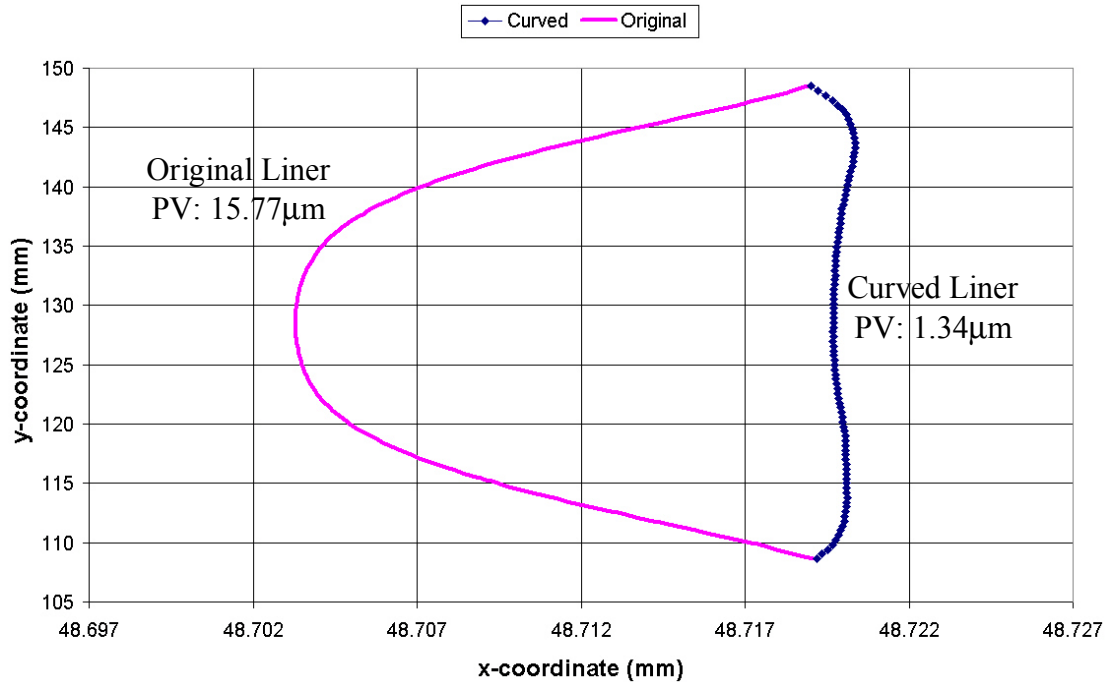


**Figure 2.16** Post-assembly inner radius profile for original and curved liner designs

This plot represents the surface profile of the liner wall (i.e., nodal coordinate locations) after the shrink fit assembly has occurred. The top and bottom plots represent the new curved and original liner designs, respectively.

Note that the flat sections of the radial displacement profile located at each end of Figure 2.14 have been removed from the representations shown in Figure 2.16. There is a radial step, or shoulder, in the liner geometry at the transition from the glide plane interfaces to the non-contact region that was included in the design for ease of liner positioning during the

assembly process. This geometry can be seen in the zoomed view of Figure 2.8. The step magnitude of approximately 0.3mm is much greater than the peak-to-valley magnitudes of either plot, which are both in the  $<20\mu\text{m}$  range. Since these plots are simply nodal coordinate locations, inclusion of the entire liner length (including this described step) would make it impossible to investigate the difference in the plots, as the region shown in Figure 2.16 would appear perfectly flat. A separate analysis on the liner ends (i.e., regions of glide plane interaction) shows identical shapes for the original and curved liner designs, thus suggesting that the latter has no effect on the glide plane/liner interfaces. The effect on the non-contact region, however, is remarkably pleasing.

The new curved liner design improved the overall x-coordinate peak-to-valley deviation of the liner wall from  $15.77\mu\text{m}$  ( $6.207 \times 10^{-4}\text{in}$ ) to  $1.34\mu\text{m}$  ( $5.290 \times 10^{-5}\text{in}$ ). Continuing to fine tune the new curved liner design could potentially further improve the flatness of the post-shrink fit liner surface, though this first iteration provides deviation from a perfect flat surface that is most likely acceptable.

### 2.3.5 Liner / Glide Plane System Integrity

The integrity of the liner/glide plane system is another concern that needs to be addressed. The small radial interference levels in conjunction with the relatively large weight of the copper glide planes could translate to static instability and slippage of any one of the components, particularly when lifted or transported. Hence, the LS-DYNA finite element code was altered to simulate such a scenario by implementing upward motion of the small

(upper) glide plane with nodal displacement specified in the positive y-direction. This motion was imposed on two single nodes, as shown in Figure 2.17.

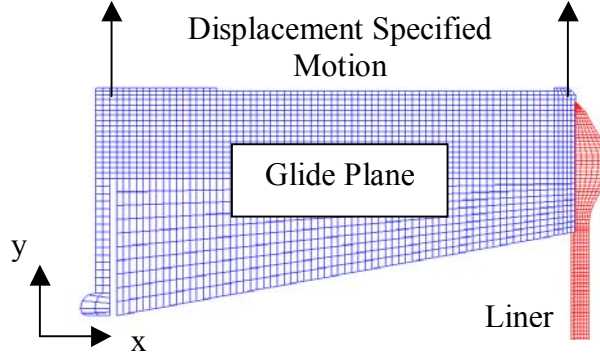


**Figure 2.17** Locations of displacement specified upward motion

The total weight of the liner and each glide planes was calculated and then uniformly distributed through the nodes of each respective component. A coefficient of friction equal to 0.30 was imposed on the interface, and motion constraints in the vertical direction that were utilized in the previous simulations were later removed to simulate vertical suspension. A summary of the simulation's time line is shown in Figure 2.18.

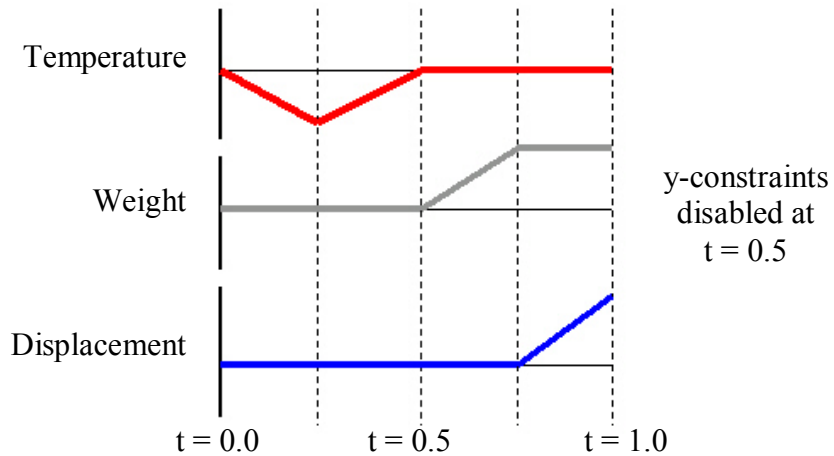


**Figure 2.18** Time line for simulation involving vertical motion

The temperature curve was adjusted so that all temperature variation was completed by the simulation's halfway point. The uniformly distributed loads on each node were then linearly increased until the specified weights of the liner ( $\sim 0.14\text{lb}$ ) and large glide plane ( $\sim 23\text{lb}$ ) were achieved. At this point the model was ready for nodal displacements to simulate the vertical lift. This particular simulation succeeded with no negative eigenvalues or errors, and converged for every implicit time step. Thus, the conclusion was made that slippage of components in this design is not a concern, and the system is statically stable as desired. The large glide plane is the heaviest of the components; hence, suspension of this part was used to determine if slippage would occur. To reinforce this conclusion, displacements were imposed on the large glide plane (thus suspending the small glide plane of  $\sim 2\text{lb}$ ) in a separate simulation that successfully converged as expected.

## **3.0 ADVANCED LINER ANALYSIS AND REDESIGN**

As previously discussed, liner deflection profiles are of great interest to those involved with experiment design parameters. However, other factors such as liner stress levels, joint behavior, and liner out-of-roundness on the precision scale are all valid issues that need to be brought to light.

### **3.1 Gap Analysis and Liner Design Changes**

Although the most significant and noticeable liner deformation occurs over the entire length of the liner (particularly in the non-contact region), there is indeed a localized liner deformation profile at each of the two joints. To maximize the flow of current at this interface between the glide planes and the liner, it is desirable to maximize the area of contact interface between these components. Therefore, it is necessary to investigate potential gaps or voids at the two liner-glide plane interfaces caused by the thermal shrink fit used for assembly. By plotting the coordinates of both the liner and glide plane nodes located within each of the given contact regions, gaps within the interfaces will become apparent. Figure 3.1 shows the nodal coordinates of the liner and glide planes located within the top contact region. The coordinates of these nodes correspond to the final time step of the LS-DYNA simulation, in which the components have reached thermal equilibrium. Since these are simply the coordinate locations of the interface nodes for both the liner and glide plane, any discrepancies in x-coordinate values at identical y-coordinate positions represent gaps. An example of such a gap can be seen in Figure 3.1.

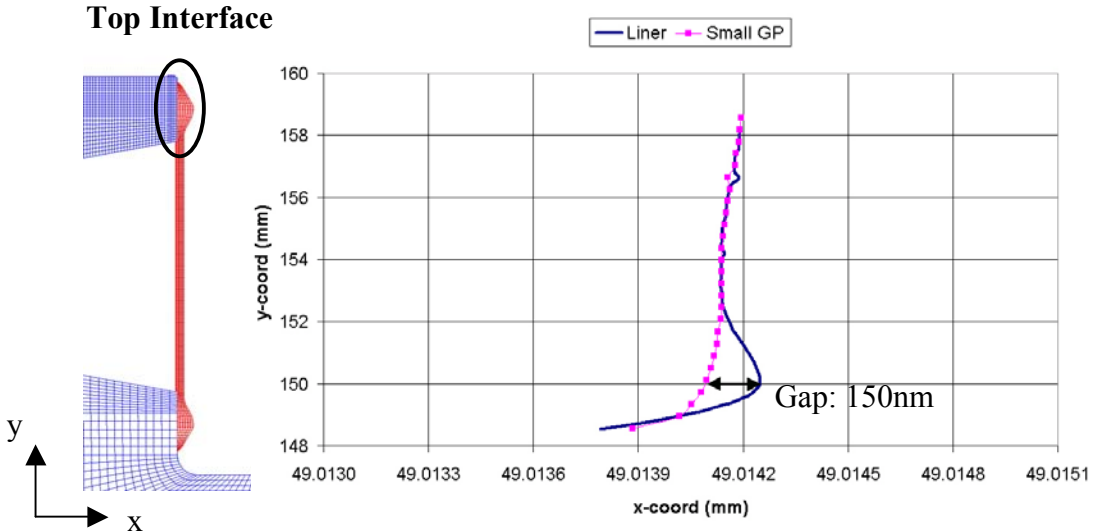


**Figure 3.1** Coordinates of liner and glide plane nodes for the Original Design located within the top interface

It is important to note that while the magnitude of the gap is only 150nm, the gap occurs over approximately one third of the entire contact length. This could be a significant factor in the overall performance of the ATLAS pulsed-power experiments, as it could potentially lower conductivity. Although not pictured, the bottom contact region results in a very similar gap profile.

To compensate for these gaps, simulations were conducted with hypothetical liner design changes. Particular attention was paid to the geometry of the bump features on either end of the liner. Figure 3.2 illustrates finite element meshes of three proposed liner redesigns in comparison to the original liner geometry.

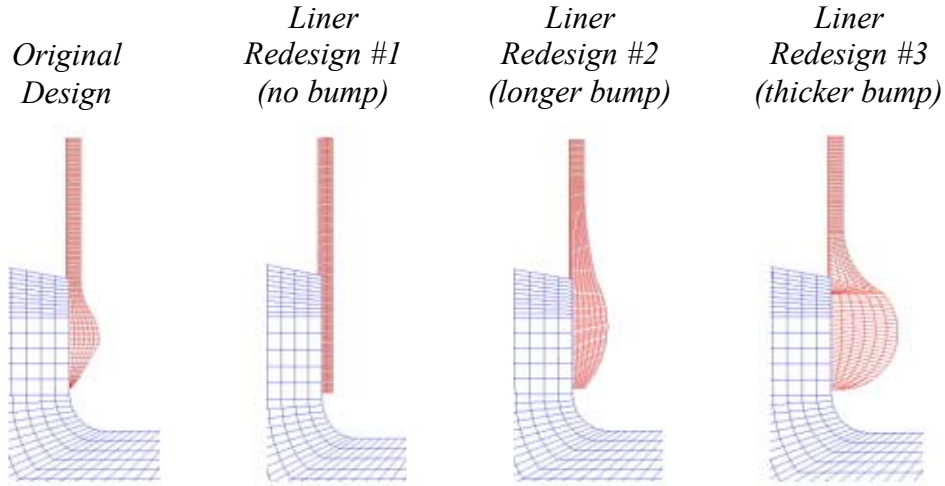


**Figure 3.2** Liner feature redesigns in comparison with the original liner

The three liner redesigns represent three extreme design alterations: no feature on the end of the liner (Liner Redesign #1), a longer smoother feature (Liner Redesign #2), and a thicker feature (Liner Redesign #3). The feature in Liner Redesign #2 contains the same width as the Original Design (2.525mm), while Liner Redesign #3 has a feature of slightly more than twice the thickness (5.619mm). Note that for each of the three redesigns, the thickness of the liner portion falling within the non-contact region is equal to that of the Original Design (1.295mm). Investigating any potential gaps in each of the redesigns was done once again by plotting the coordinates of the liner and glide plane nodes falling within the interface region at the final time step of the LS-DYNA simulation. The gap resulting from Liner Redesign #1 is shown in Figure 3.3. It is evident that removing the liner bump feature altogether results in a much wider void in the liner/glide plane interface. Even more important, however, is the fact that the void occurs over approximately half the total interface length.

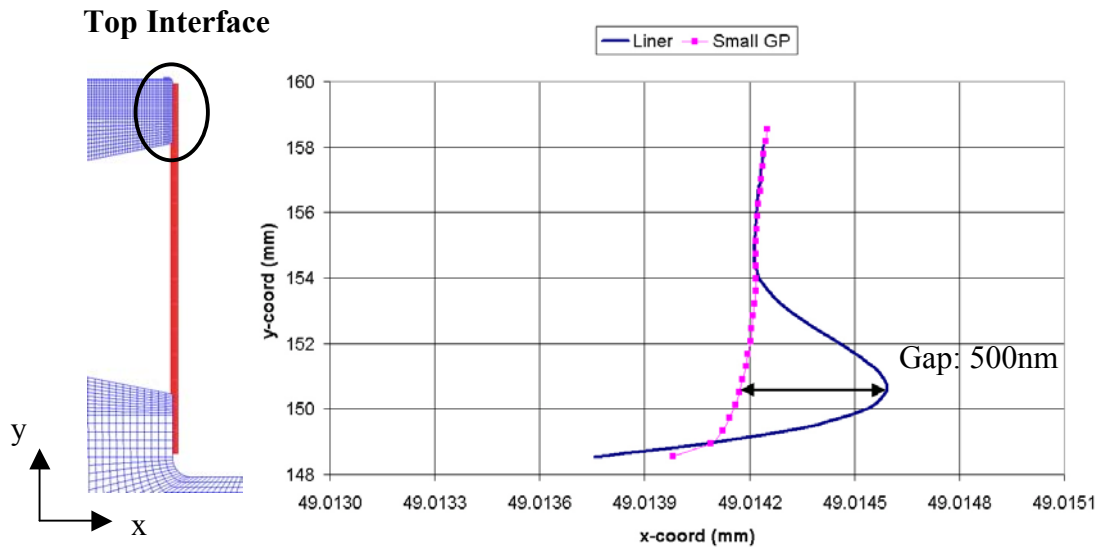


**Figure 3.3** Coordinates of liner and glide plane nodes for Liner Redesign #1 located within the top interface

Altering the liner bump feature to a longer, smoother geometry considerably decreases the size of the void, essentially eliminating it altogether, as shown for Liner Redesign #2 in Figure 3.4. Again, the bottom interface (not shown) gives very similar results.

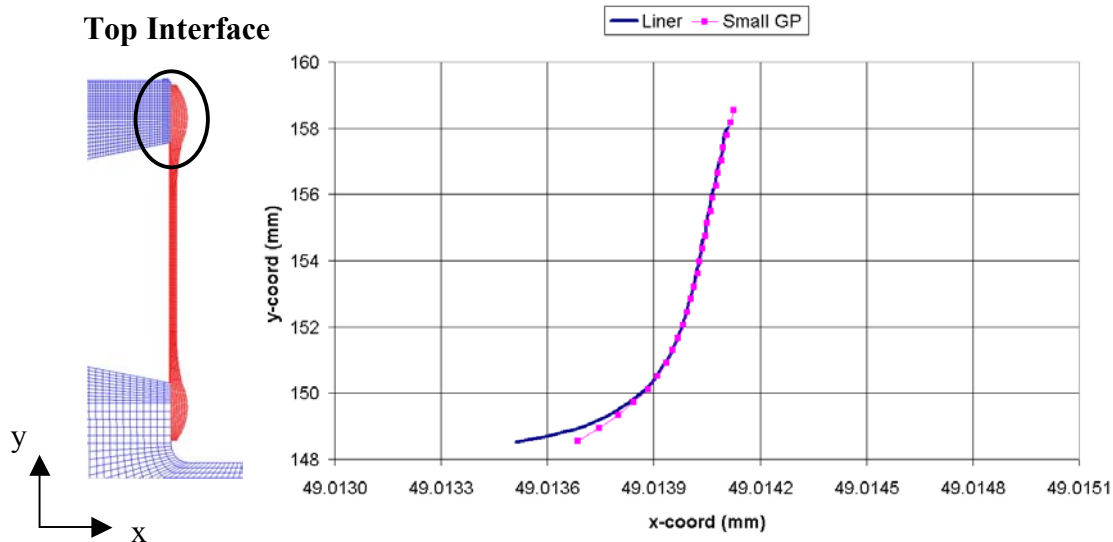


**Figure 3.4** Coordinates of liner and glide plane nodes for Liner Redesign #2 located within the top interface

Liner Redesign #3 produces similar void reduction. The favorable results can be seen in Figure 3.5, which shows the top interface. Again, the top interface was chosen for illustration but the bottom interface, although not shown, gave very similar results.

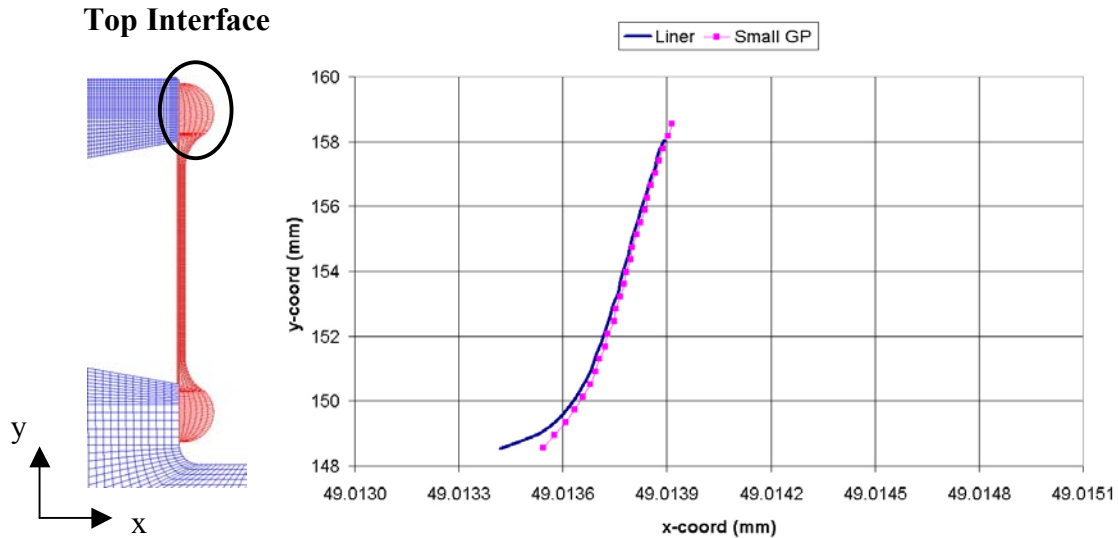


**Figure 3.5** Coordinates of liner and glide plane nodes for Liner Redesign #3 located within the top interface

As expected, the maximum stress levels in Liner Redesign #1 (5,350psi) exceeded the yield strength of the 1100 aluminum. This, coupled with the fact that the gap is greatly increased without the presence of the liner features, suggest that these liner features are crucial for the desired performance of the ATLAS pulsed-power experiments. The maximum stress levels found in the liner for each liner design are summarized in Table 4.

**Table 4** Maximum liner hoop stress for liner redesigns

Geometry	Maximum Liner Stress Level
Original Design	4,190 psi
Liner Redesign #1	5,350 psi
Liner Redesign #2	4,125 psi
Liner Redesign #3	3,400 psi

The maximum stress level in Liner Redesign #2 was similar to the Original Design, though this design reduced the size of the void considerably. Liner Redesign #3 significantly reduced both the maximum liner stress and the void magnitude.

### 3.2 Effects of an Out-of-Round Liner

Improper machining or handling of these thin aluminum liners could potentially cause distortion and therefore non-axisymmetric geometries. It is believed that this could potentially alter the stress levels and affect the deflection profile for the liner. To model this scenario, a 2D plain strain cross-sectional model at the liner's minimum wall thickness location was used for analysis. The shape of the non-axisymmetric liner was assumed to be elliptical, with the radial interference values being varied at two points located 180 degrees apart. The locations of the varied radial interference value,  $\delta^*$ , are shown in Figure 3.6.

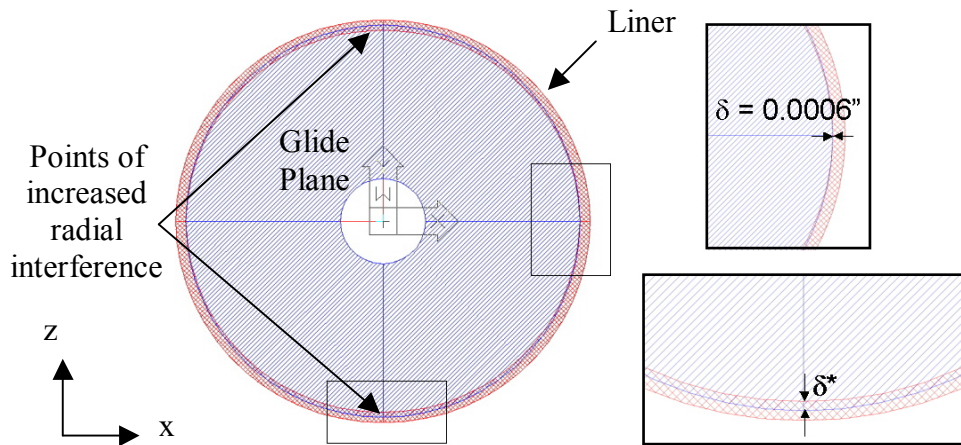


**Figure 3.6** Cross-sectional geometry of an elliptical out-of-round liner

Attention was focused on the maximum hoop stress and its dependency on the liner eccentricity. A list of the range of variation for the radial interference values and the corresponding maximum hoop stress is shown in Table 5, and a normalized graphical representation is shown in Figure 3.7.

**Table 5** Maximum liner hoop stress for various degrees of elliptical out-of-roundness

<b>δ* Value</b>	<b>δ* / δ Ratio</b>	<b>Maximum Liner Stress</b>	<b>Plastic Strain?</b>
7.62µm (0.0003in)	0.500	3,000 psi	No
15.25µm (0.0006in)	1.000	3,590 psi	No
20.30µm (0.0008in)	1.333	4,250 psi	No
25.40µm (0.0010in)	1.667	4,920 psi	No
30.50µm (0.0012in)	2.000	5,535 psi	Yes
38.10µm (0.0015in)	2.500	5,850 psi	Yes

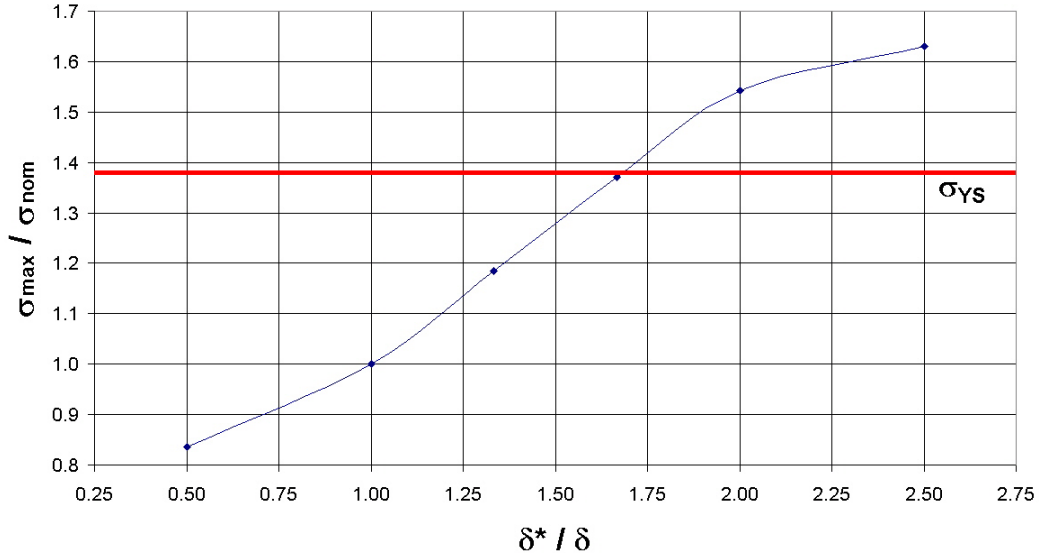


**Figure 3.7** Normalized graph of maximum hoop stress versus liner distortion

The radial interference value of  $15.24\mu\text{m}$  (0.0006in) represents the baseline value for the current round liner design. Improper handling is predicted to be the main source of concern for any distortions in the liner, rather than improper machining or Diamond Turning Machine axis stability errors. To simulate potential improper handling, two point loads (which simulate a pinching force that could be caused by two fingers) were imposed 180 degrees apart on the liner OD. This corresponds to the location of the varied radial interference values for the finite element model as shown in Figure 3.6. Such forces cause liner distortion and result in an elliptical shape, shown in Figure 3.8, which also coincides to the finite element model for non-axisymmetric geometries.

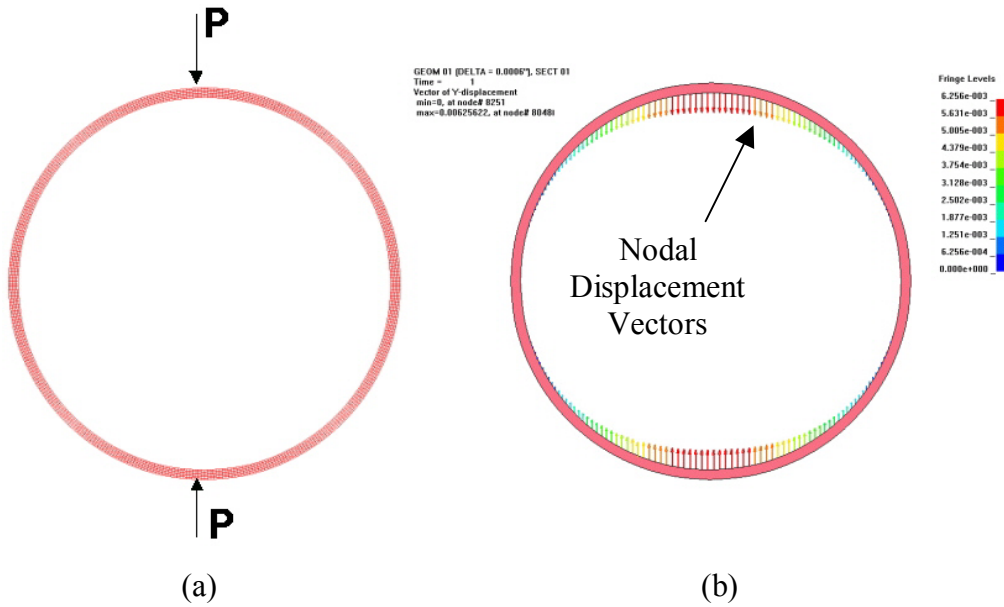


**Figure 3.8** Finite element simulation of “pinch” loads on a thin-walled liner (a), and post-processor resultant displacement vectors (b)

By incrementally increasing the load  $P$ , it was determined which load level the thin-walled liner could withstand prior to permanent plastic deformation. A graphical representation of this load increase is shown in Figure 3.9.

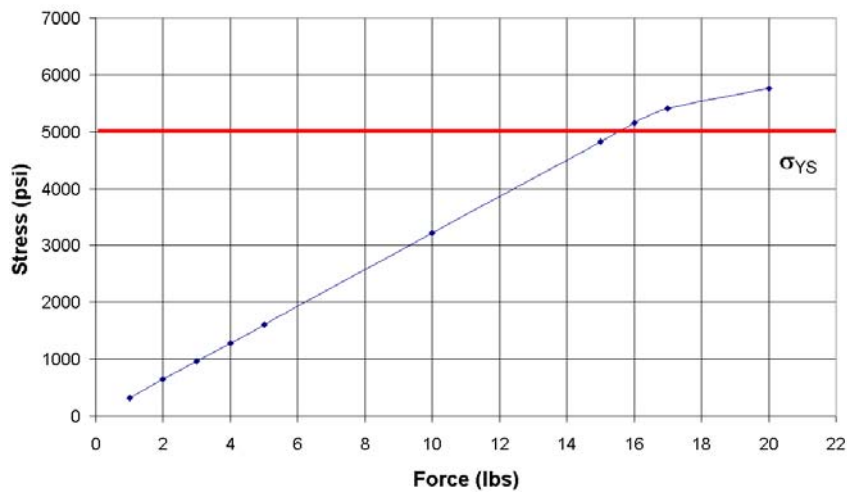


**Figure 3.9** Resulting maximum hoop stress due to increased “pinch” loads on a thin-walled liner

## **4.0 FINITE ELEMENT VERIFICATION**

After obtaining the previously described results, it was necessary to investigate LS-DYNA's ability to accurately model advanced contact problems such as the shrink fit assembly used in the ATLAS design. To verify the LS-DYNA code, three simplified shrink fit test specimens were fabricated. Each of these test specimens involved a thin-walled aluminum cylinder (liner) and a copper disk (glide plane) that was shrunk fit onto the cylinder's end portion, similar to the ATLAS geometry. The idea behind these test specimens was to measure the liner deflection (a quantifiable and measurable parameter) caused by the shrink fit and compare it to the deflection profile predicted by the corresponding LS-DYNA model. With each successive test specimen, iterative modifications were made for geometric design, fabrication, and measurement technique until sufficient data was obtained for the verification of the finite element code.

### **4.1 Shrink Fit Test Specimen #1**

#### **4.1.1 Test Specimen #1: Design**

The first test specimen consisted of a thin-walled 6061 aluminum cylinder (simulated liner) and a copper disc (simulated glide plane). These components were machined using the ASG-2500 Diamond Turning Machine (DTM). The liner was a simple, uniform cross-section cylinder with no features for fewer machining complications.

Prior to fabrication, calculations were performed to ensure sufficient pressure between the two components for maintaining the shrink fit, even with potential environmental temperature increases after assembly. The liner OD and ID were first selected such that thickness (0.993mm) closely matched that of the actual ATLAS liner (1.2954mm). The maximum test specimen liner thickness was limited only by the 1.2mm thickness of the original, as-received aluminum tubing from which the test liner was fabricated. Removing just enough material to ensure a perfectly cylindrical test specimen liner was crucial. The OD of the glide plane specimen was then varied using a spreadsheet, giving a wide range of possible interferences. Radial interference values ranging from approximately 2.5 $\mu\text{m}$  to 75 $\mu\text{m}$  were investigated.

Each value of interference was tested to determine whether the temperature of liquid nitrogen would provide sufficient shrinkage to allow the glide plane to slip into the liner end for assembly. Equation 15 was used to calculate the diametral reduction,  $\Delta D$ , of the copper glide plane.

$$\Delta D = \alpha D_{orig} \Delta T \quad (15)$$

Here,  $\alpha$  is the thermal expansion coefficient of copper ( $1.70 \times 10^{-5}$   $(^\circ\text{C})^{-1}$ ),  $D_{orig}$  is the glide plane OD dimension, and  $\Delta T$  is the temperature drop generated by the liquid nitrogen ( $-196^\circ\text{C}$ ). Then, using standard shrink fit theory, radial and hoop stress values were calculated (Equations 10 and 11, respectively) to prevent yielding of either component. Recall that from an earlier analysis, it was concluded that stress levels are difficult to predict for an *entire* cylinder length in a partial shrink fit configuration, but maximum stresses at the

interface closely correspond to stress values given by standard shrink fit formulas. The potential for a significant environmental temperature increase (+20°C), which could be experienced if the test specimen were to be taken outside on a hot day, was also a concern. Since the thermal expansion coefficient of aluminum is greater than that of copper, such a temperature increase could result in a reduced interference, as the liner would expand at a faster rate than the inner glide plane. For each of the radial interference values that were investigated, this temperature increase was analytically applied. With an increase in temperature comes reduced radial interference, and therefore reduced radial pressure. This pressure was calculated using Equation 16, where  $\delta_{new}$  represents the calculated reduced radial interference caused by an environmental temperature increase.

$$p = \frac{\delta_{new}}{b \left[ \frac{1}{E_o} \left( \frac{c^2 + b^2}{c^2 - b^2} + v_o \right) + \frac{1}{E_i} \left( \frac{b^2 + a^2}{b^2 - a^2} - v_i \right) \right]} \quad (16)$$

This radial pressure was translated into a radial force using the known interface surface area, and the resulting axial friction force was then determined with a friction coefficient of 0.30. The friction force, when compared to the weight of glide plane, determined whether the shrink fit would hold the components together even with this significant temperature increase. Based on these preliminary calculations addressing stresses, potential temperature increases, and the ability to provide clearance due to cooling, the dimensions for Test Specimen #1 were selected, and are summarized in Table 6.

**Table 6** Dimensional parameters for Test Specimen #1

Test Specimen Parameter	Parameter Value
Glide Plane OD	48.598 mm (1.9133 in)
Liner OD	50.544 mm (1.9899 in)
Liner ID	48.559 mm (1.9118 in)
Liner Wall Thickness	0.993 mm (0.0391 in)
Liner Length	43.000 mm (1.6929 in)
Interface Length	7.366 mm (0.2900 in)
Radial Interference	19.30 $\mu\text{m}$ ( $7.6 \times 10^{-4}$ in)

It is important to note that the overall length of the test liner was much greater than the length over which contact with the glide plane occurs. The system was assembled via a thermal shrink fit, with the glide plane cooled in liquid nitrogen to a temperature of approximately -196°C. The parts were then allowed to warm to ambient temperature. Figure 4.1 includes a photograph of the assembled test specimen. Note that the component at the left portion of the liner is a copper plug that was machined with a radial clearance, slipped onto the liner end, and secured with high-strength epoxy. This component provided a flat surface for attaching the liner to the vacuum chuck of the DTM.

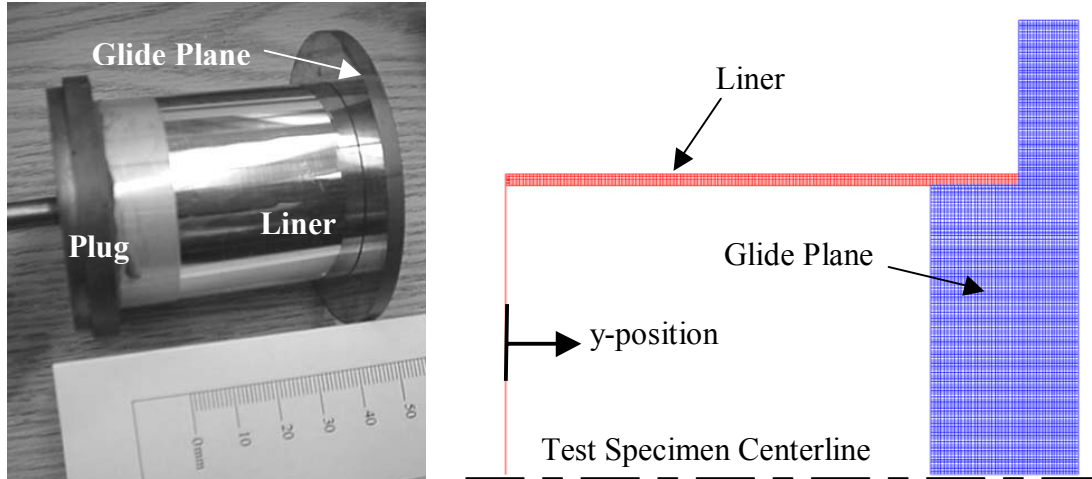


**Figure 4.1** Test Specimen #1 after shrink fit assembly (left) and the corresponding axisymmetric finite element model (right)

Using LS-DYNA, this test specimen was modeled (Figure 4.1) and the shrink fit assembly was simulated using an identical procedure described for the ATLAS model. The material properties for each component are listed in Table 7.

**Table 7** Material properties for Test Specimen #1

	<b>Copper Glide Plane</b>	<b>6061 Aluminum Liner</b>
Young's Modulus	$1.5954 \times 10^7$ psi	$1.0000 \times 10^7$ psi
Poisson's Ratio	0.35	0.33
Thermal Expansion Coefficient	$1.70 \times 10^{-5}$ ( $^{\circ}\text{C}$ ) $^{-1}$	$2.30 \times 10^{-5}$ ( $^{\circ}\text{C}$ ) $^{-1}$
Yield Strength	50,000 psi	40,000 psi

The liner consisted of 2004 elements with 6 elements through the wall thickness, and the copper glide plane contained 1996 elements. A comparison of the calculated stress values (Equations 9 and 10) to those given by LS-DYNA is given in Table 8. The LS-DYNA values represent the maximum stress in the interface region.

**Table 8** Comparison of LS-DYNA and shrink fit theory hoop and radial stress

	Hoop Stress, $\sigma_{\theta\theta}$	Radial Stress, $\sigma_{rr}$
Shrink Fit Theory	7789 psi	-286 psi
LS-DYNA	7743 psi	-273 psi
% Difference	0.6	4.5

The other important parameter is liner displacement. A plot of the radial displacement of the liner's outer wall is shown in Figure 4.2. Note that the vertical magnification is 2250 times that of the horizontal. The OD of the glide plane is  $\sim 19\mu\text{m}$  larger than the ID of the liner, and as a result, the maximum radial deflection of the liner is approximately the same magnitude for the right portion of this curve (the region in which the shrink fit exists). The flat region on the left represents the free end of the liner, which is neither in contact with the glide plane nor effected by the thermal shrink and therefore yields no displacement. Since the radial deflection is fully decayed in this region, it was unnecessary to include the machining plug in the model (Figure 4.1), as it has no effect on the radial deflection behavior.

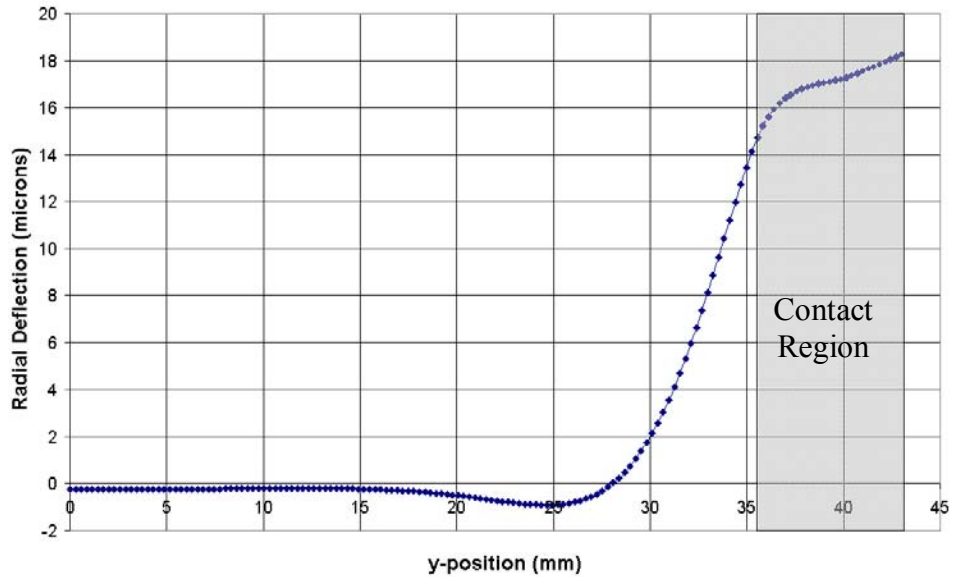


**Figure 4.2** Test Specimen #1 liner deflection due to a thermal shrink fit

Note that the maximum radial deflection ( $18.54\mu\text{m}$ ) in the contact region is slightly less than the radial interference ( $19.30\mu\text{m}$ ) caused by the difference between the glide plane and the liner radii. This is due to the fact that the glide plane is somewhat compressed as a result of the shrink fit.

#### 4.1.2 Test Specimen #1: Fabrication and Dimensional Measurements

From Table 8, it is clear that the LS-DYNA results for the contact region closely follow the results given by shrink fit theory. However, a comparison between LS-DYNA results and experimental results determines how well the simulation tool can be used to predict radial displacement and stress levels in systems such as ATLAS. After machining the liner and glide plane, the radial dimensions were measured with a micrometer using an iterative process of machining, measuring, and re-machining in order to achieve the desired

dimensions. Upon completion of both components, the shape of the test liner's outer surface was determined by measuring three lines on the outer surface of the cylinder, each 120 degrees apart in the circumferential direction. These measurements were performed using the Zygo GPI Interferometer. Post-shrink fit measurements of the liner's outer surface were also taken, again using the Zygo GPI Interferometer. The difference in these profiles provided the radial displacement values of the test liner due to the shrink fit interference.

#### 4.1.3 Test Specimen #1: Surface Measurements

The ability to obtain the actual test liner displacement values is dependent upon the completeness of the data collection for both before and after shrink fit surface measurements. Figure 4.3 illustrates the comparison of the LS-DYNA displacement values with actual displacement values determined using the Zygo GPI Interferometer data.

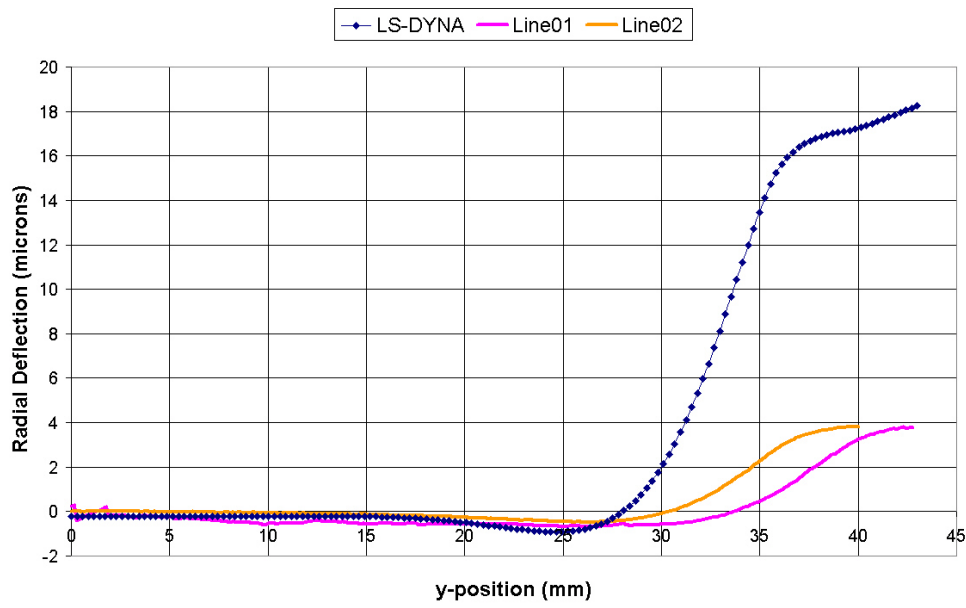


**Figure 4.3** Comparison of LS-DYNA (theoretical) and Test Specimen #1 (experimental) liner displacement values

There is clearly a discrepancy between the liner displacement caused by the glide plane and displacement predicted by FEA. As mentioned earlier, however, the LS-DYNA stress values corresponded well to the expected values. Therefore, it was concluded that the test liner or test glide plane (or both) components were fabricated with an effective interference much less than the target value of  $19.30\mu\text{m}$ . The curves in Figure 4.3 suggest an actual radial interference of approximately  $3.8\mu\text{m}$ . Assuming this is the case (which is reasonable based on the actual deflection data), a simulation model was created using the smaller radial interference of  $3.8\mu\text{m}$ .

Such a model predicts very similar magnitude and distribution of radial displacement values in comparison to the actual displacement values, as shown in Figure 4.4. This figure illustrates that the radial displacement values given by the LS-DYNA model lie slightly above the actual values for most points along the y-position of the liner. This particular FEA model did not account for friction effects within the contact region. Furthermore, any inconsistencies in the materials used may have altered the materials' properties to some extent. Such factors are possible causes of the discrepancy between FEA model and actual radial displacement data. A more likely explanation comes from the problems with the machining process. This particular test specimen became detached from the DTM vacuum spindle on two separate occasions, causing it to strike the x-axis table with considerable force. Such machining problems very well could have distorted the thin-walled cylinder, thus causing discrepancies between the actual and theoretical results at various positions around the circumference of the liner.

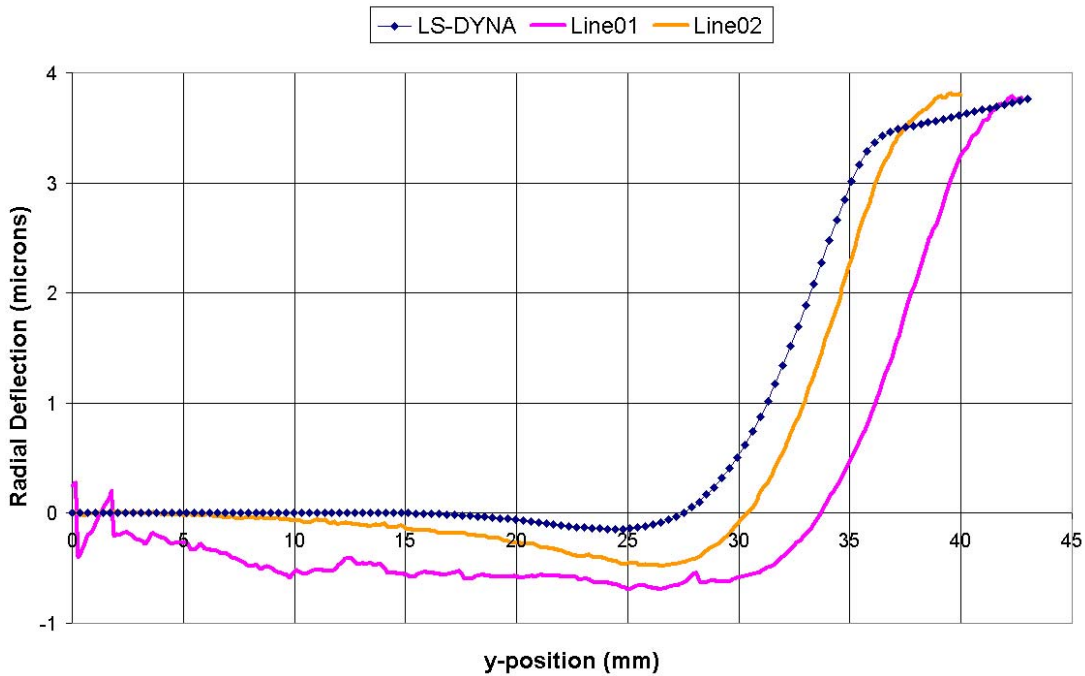


**Figure 4.4** Results of LS-DYNA simulation when modeled with less interference, in comparison to Test Specimen #1 liner displacement values

The first attempt of fabricating a test specimen for the purpose of validating the LS-DYNA code had some flaws. The machining process was not effectively performed as expected, and the measuring technique lacked the precision and resolution needed to obtain components with such a high demand for dimensional accuracy. An improved measurement technique was established, and a second test specimen was machined in hopes of obtaining more promising data.

## 4.2 Shrink Fit Test Specimen #2

### 4.2.1 Test Specimen #2: Design

Once again, preliminary shrink fit analytical calculations were performed to determine maximum hoop and radial stress levels and dimensions were selected to avoid yielding of either component as a result of the shrink fit assembly. A smaller radial interference value was selected simply to investigate test specimens with various parameters. These dimensions are listed in Table 9.

**Table 9** Dimensional parameters for Test Specimen #2

Test Specimen Parameter	Parameter Value
Glide Plane OD	48.593 mm (1.9131 in)
Liner OD	50.549 mm (1.9901 in)
Liner ID	48.562 mm (1.9119 in)
Liner Wall Thickness	0.993 mm (0.0391 in)
Liner Length	48.000 mm (1.8898 in)
Interface Length	6.350 mm (0.2500 in)
Radial Interference	15.50 $\mu\text{m}$ ( $6.1 \times 10^{-4}$ in)

### 4.2.2 Test Specimen #2: Fabrication and Dimensional Measurements

After determining the dimensions for this test specimen, the ASG-2500 DTM was used to machine both components with very high surface finishes. A major goal of this test specimen was to obtain a higher degree of precision, particularly for radial dimensions. As previously explained, components for Test Specimen #1 were measured with calipers and micrometers, which did not have the resolution necessary to ensure such accurate dimensions. The B&S Coordinate Measuring Machine (CMM) was thought to be a good

alternative, but upon measuring various gage blocks to validate the accuracy of the CMM, it was found that the errors were too large for the purposes of machining and measuring these particular components. Using 0.500in, 1.000in, and 2.000in gage blocks, the average measurement variation along a single axis was found to be approximately  $3\mu\text{m}$ . Such an uncertainty could result in two components that do not mesh correctly when assembled by means of a shrink fit process.

Since the CMM was not sufficiently accurate for measuring each component, the ASG-2500 DTM with a Federal gage and a gage block stack was used to measure the diameter of each mating component for Test Specimen #2. The apparatus is shown in Figure 4.5.

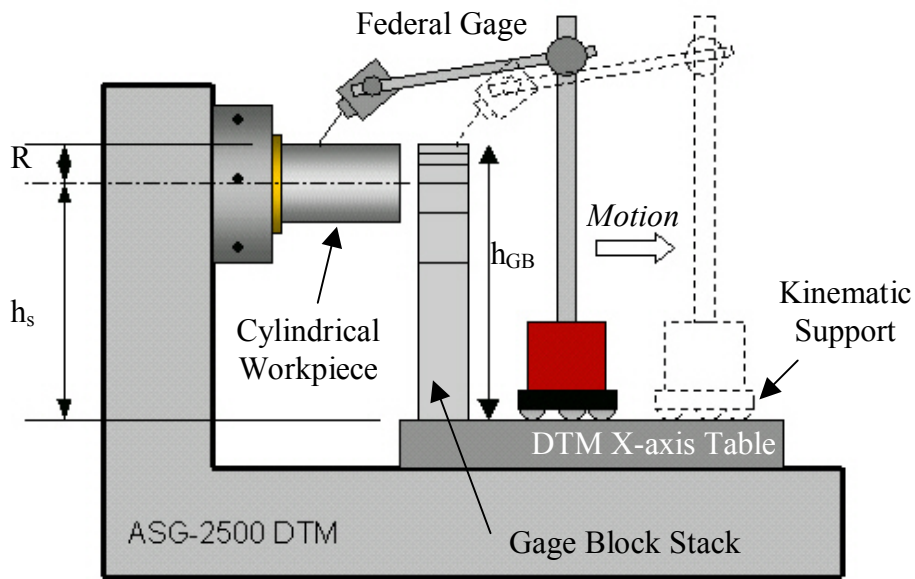


**Figure 4.5** Apparatus used for measuring Test Specimen #2 components

The technique consisted of moving the Federal gage from the highpoint of the cylindrical workpiece to the slightly lower surface of the gage block stack. The difference in height

was indicated by the Federal gage readout ( $FG_{Readout}$ ). Theoretically, if the precise height of the gage block ( $h_{GB}$ ) and the spindle height ( $h_s$ ) were both known, the radius of the workpiece,  $R$ , could be determined using Equation 17.

$$R = h_{GB} - h_s + FG_{Readout} \quad (17)$$

The DTM spindle centerline is published to be precisely 152.622mm (6.00874in) above the x-axis table. However, frequent use and wear on the spindle can cause this value to slightly change over time. Thus it was necessary to validate this parameter. A centering plug was used to establish the diamond tool position in correspondence to the spindle centerline. Upon measuring the centering plug using the Zygo GPI Interferometer, it was determined that the tool was centered to within a height of +27nm. Using a Federal gage and a gage block stack, the procedure previously described in this section was used for first verifying spindle centerline height above the x-axis table,  $h_s$ , since this was an essential parameter for this measurement technique. The difference between the centered tool's height and the gage block was determined, and hence the spindle centerline height could be determined. It was deduced that the spindle centerline was approximately 4 $\mu\text{m}$  lower than published and so a value of 152.418mm (6.00858in) was used for the spindle centerline  $h_s$  in Equation 17.

Since multiple gage blocks were used for verifying the spindle centerline height and also for the actual radial measurement technique itself, it is important to note that there are tolerances associated with each gage block. For measuring the radius of each component, six gage blocks of various dimensions had to be used to achieve the spindle height of

6.00858in plus the radius of the workpiece. The published values for the Grade 2 (A+) gage blocks that were used are listed in Table 10.

**Table 10** Tolerances of Grade 2 (A+) gage blocks

Gage Block Length	Positive Tolerance	Negative Tolerance
$L \leq 1$ in (4 used)	0.1016 $\mu\text{m}$ (4 $\mu\text{in}$ )	0.0508 $\mu\text{m}$ (2 $\mu\text{in}$ )
$L = 2$ in (1 used)	0.2032 $\mu\text{m}$ (8 $\mu\text{in}$ )	0.1016 $\mu\text{m}$ (4 $\mu\text{in}$ )
$L = 4$ in (1 used)	0.3048 $\mu\text{m}$ (12 $\mu\text{in}$ )	0.1524 $\mu\text{m}$ (6 $\mu\text{in}$ )

Using statistical analysis, the following equations were used to determine the overall uncertainty associated with this stack of six gage blocks.

$$+Tolerance = +\sqrt{(+Tol_1)^2 + (+Tol_2)^2 + (+Tol_3)^2 + \dots} \quad (18)$$

$$-Tolerance = -\sqrt{(-Tol_1)^2 + (-Tol_2)^2 + (-Tol_3)^2 + \dots} \quad (19)$$

It was calculated that the overall positive and negative gage block stack tolerances were +420nm and -210nm, respectively. Using the Federal gage, it was determined that the height of the gage block's top surface was repeatable to approximately one micrometer, which was attributed to non-flat gage blocks causing slight tilt. Additionally, the film thickness of the oil in between each gage block effects the measurement, essentially making the gage block height larger than desired. Hence it was concluded that the uncertainty of this measurement technique was approximately 2 $\mu\text{m}$ , mainly due to the gage blocks.

#### 4.2.3 Test Specimen #2: Surface Measurements

Again, the deflection profile of the test specimen liner was measured using an interferometer, and this profile was compared to a FEA model of corresponding geometry. As explained earlier, the difference in the before and after shrink fit measurement liner profiles provides the radial deflection profile. With the first test specimen, this subtraction of data sets was done manually using a spreadsheet, but the magnitude of these data sets made them tedious to organize. It was later discovered that the software package for the Zygo GPI Interferometer contains a convenient “subtract data” function for two sets of data. In order for this to be useful, however, the data sets must contain identical pixel locations. There are no fiducials on the interferometer base with which to align a workpiece. Therefore, a kinematic support was designed and developed for the purpose of maintaining the same position of the test specimen for measurements before and after the shrink fit. The kinematic support illustrating the test specimen orientation is shown in Figure 4.6.

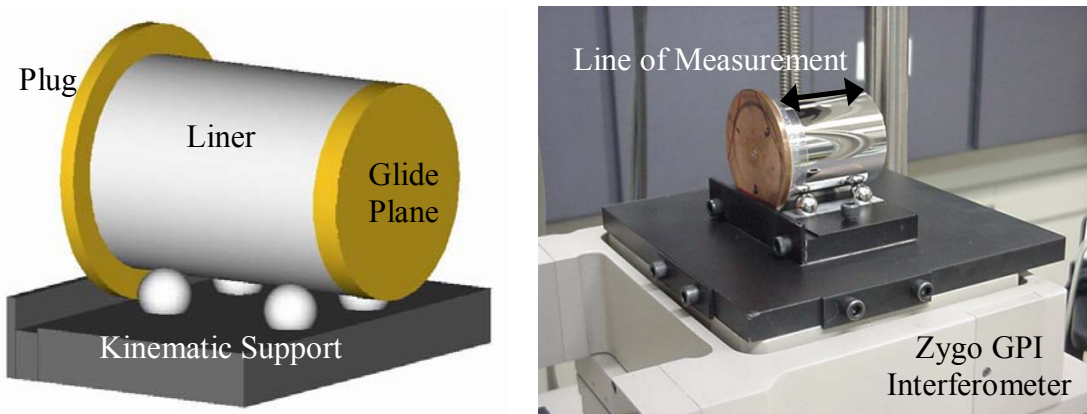


**Figure 4.6** Kinematic support used for test specimen measurements on the Zygo GPI Interferometer

Once again, the right hand portion of the deflection profile (Figure 4.7) represents the region in which the shrink fit occurs, and therefore the region subjected to the largest deflection. The large slope in the deflection curve ( $y$ -position  $> 35\text{mm}$ ) resulted in a region that could not be measured using the interferometer since it is unable to resolve fringes for surfaces with significant slope. Therefore, no data was obtained near the shrink fit interference end of the liner.

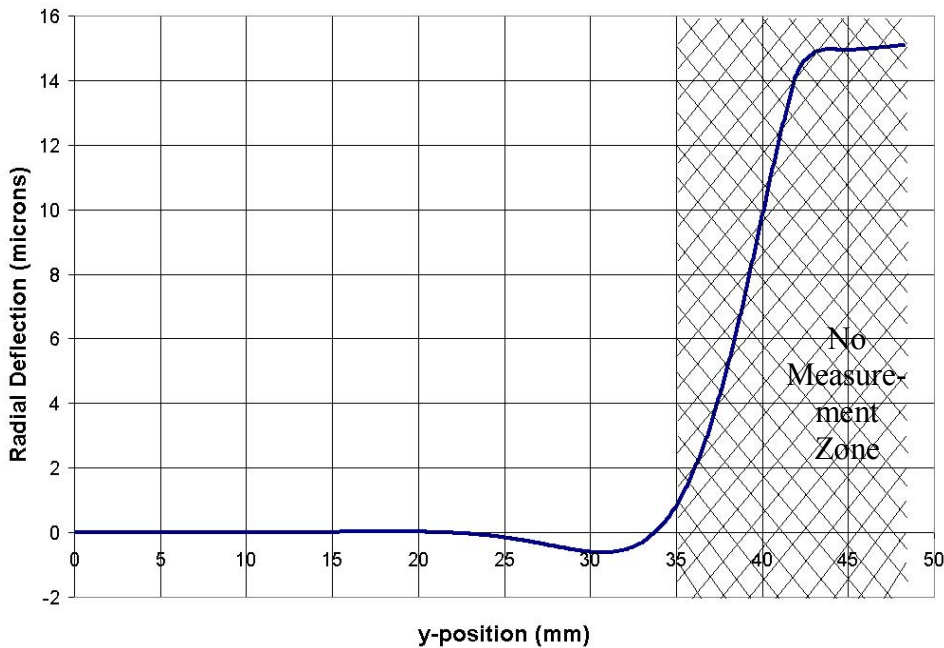


**Figure 4.7** Test Specimen #2 liner radial deflection values predicted by LS-DYNA

For the measurable portion of the liner ( $y$ -position  $< 35\text{mm}$ ), the experimental deflection curves are shown in Figure 4.8 in comparison with the deflection curves predicted by LS-DYNA. These graphs represent experimental deflection profiles located at three different circumferential locations around the liner.

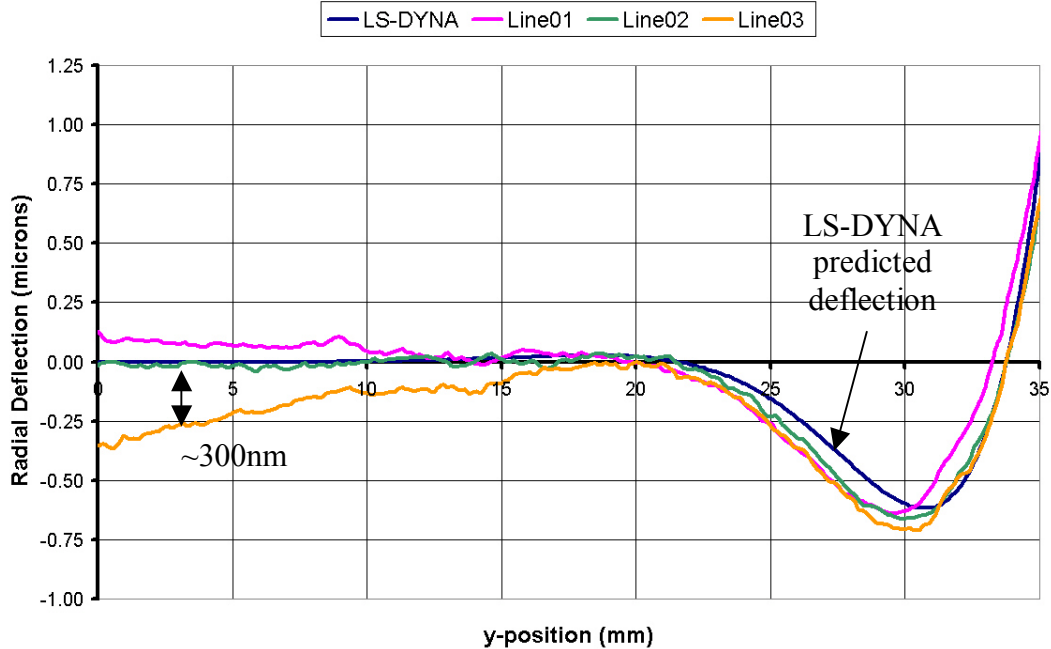


**Figure 4.8** Comparison of LS-DYNA (theoretical) and Test Specimen #2 (experimental) liner displacement values

As seen in Figure 4.8, the maximum difference between experimental and simulated liner deflection plots for any given region is approximately 300nm. This difference can be attributed to the uncertainty in the measurement technique. The gage block combination had a maximum uncertainty range of 630nm and the repeatability error was approximately 1 $\mu$ m. Both uncertainties are greater than the experimental error. This second test specimen was deemed moderately successful in that the experimental data corresponded well to the LS-DYNA simulated results. However, data was not obtained for the shrink fit end of the liner, a region of high interest for the purpose of investigating these partial shrink fit configurations. Hence a third test specimen was designed and fabricated with modifications that could potentially solve this problem.

## 4.3 Shrink Fit Test Specimen #3

### 4.3.1 Test Specimen #3: Design

The magnitude of radial interference was reduced even further to avoid large slopes in close proximity to the shrink fit region. Many parameters including liner length and thickness, liner OD and ID, and the interface length remained approximately equal to those values for the previous test specimens. These parameters are listed in Table 11.

**Table 11** Dimensional parameters for Test Specimen #3

Test Specimen Parameter	Parameter Value
Glide Plane OD	48.454 mm (1.9077 in)
Liner OD	50.414 mm (1.9848 in)
Liner ID	48.447 mm (1.9074 in)
Liner Wall Thickness	0.984 mm (0.0387 in)
Liner Length	51.000 mm (2.0079 in)
Interface Length	6.350 mm (0.2500 in)
Radial Interference	3.50 $\mu\text{m}$ ( $1.4 \times 10^{-4}$ in)

### 4.3.2 Test Specimen #3: Fabrication and Dimensional Measurements

Measuring dimensions accurately to within a few micrometers was considered sufficient for shrink fits with radial interference magnitudes of 15 to 20 $\mu\text{m}$  (similar to the first two test specimens). For these cases, such errors could possibly not be a factor, as the shrink fit assembly would more than likely still “work”. However, with smaller radial interference values on the order of 3.50 $\mu\text{m}$  (corresponding to this test specimen), it is desirable to develop measurement techniques that ensure even higher dimensional accuracy. Dimensional errors on the order of a few micrometers would most likely result in

components that don't properly mesh together, if at all. Therefore, two additional methods were evaluated.

The first method also uses the Diamond Turning Machine and a Federal gage. However, instead of using a stack of gage blocks, as used with Test Specimen #2, a single gage block is attached to the workpiece by means of a rubber band. As usual, the diamond tool height (y-position) is adjusted to match the DTM spindle centerline height using the micro-height adjuster (not shown). A schematic of this measurement technique setup is shown in Figure 4.9.

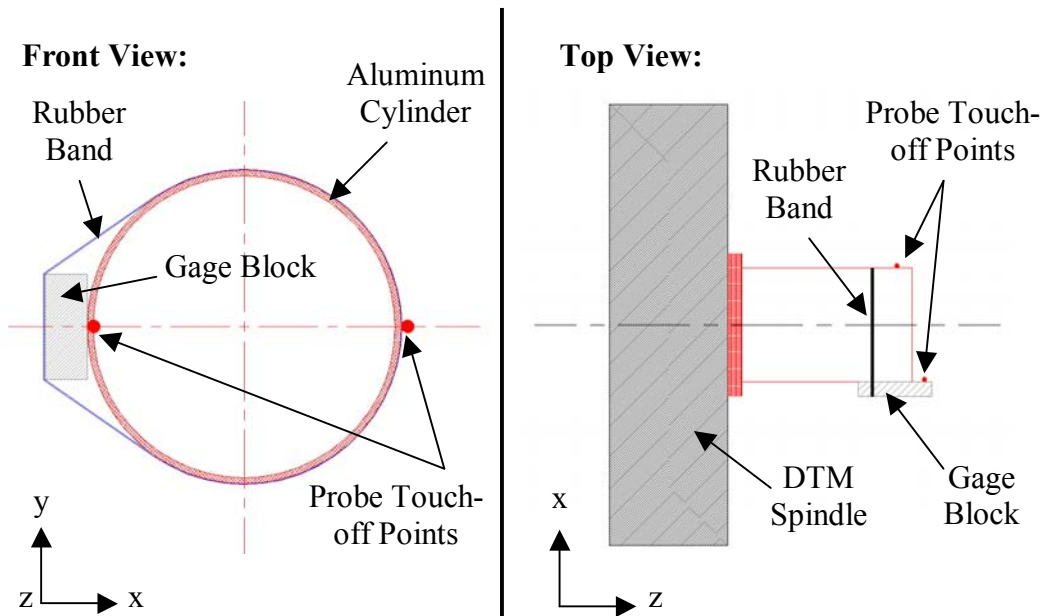


**Figure 4.9** Schematic of an additional radial measurement technique

Using this method, the Federal gage is attached to the x-axis table of the DTM using a magnetic base. By jogging the x-axis slowly, the Federal gage probe is touched off on both the inner edge of the gage block (which is essentially the outer edge of the cylindrical

workpiece at the point of contact) and on the outer diameter of the cylindrical workpiece on the opposite side. It is necessary to touch off using the same directional approach since the Federal gage is spring loaded in a single direction. Traversing at  $\sim 1\text{mm/min}$  or less can give coordinate touch off points accurate to within a few nanometers. Recording the change in x-coordinates between each touch off gives the outer diameter of the cylindrical workpiece. Since the tool height can be adjusted to match the height of the spindle centerline to within a micrometer using a machined centering plug, it is then trivial to machine the cylindrical workpiece ID to a desired dimension using the DTM coordinates. Such small errors in height have negligible error effects on the outcome of the actual workpiece radius. The relatively gradual curvature of a 2in OD cylindrical workpiece allows for some discrepancy between the tool height and the spindle centerline height without remarkably sacrificing dimensional accuracy. However, there are problems associated with this technique. It is imperative for the gage block to be exactly perpendicular to the x-axis table of the DTM, and for the Federal gage probe height to closely match that of the spindle centerline. As just explained, there is some allowable height error in the Federal gage probe. Regardless, adjusting the height of the probe tip to within a small range of desirable levels ( $<25\mu\text{m}$ ) is not necessarily a trouble-free procedure. Furthermore, touching a diamond turned surface with a gage block would undoubtedly result in a scratched workpiece. While the rubber band would not produce forces high enough to permanently deform the thin-walled cylinder (refer to Figure 3.9), it could distort the thin-walled aluminum workpiece while in use, thus tainting the diametral measurement. At any rate, it is generally not good precision engineering practice to handle a diamond turned workpiece while attached to the spindle, as

it could result in movement or disconnection from the vacuum chuck. Based on these issues, this measurement technique was not used. However, this technique shows promise and may be beneficial to other research projects, and was therefore included in this thesis.

Another measurement technique involved a simple solution: center the diamond tool. The tool height was iteratively centered in both the horizontal and vertical directions (x- and y-directions, respectively) by machining centering plugs and examining them under the Zygo GPI Interferometer and high-resolution microscopes. With a centered tool, the  $x=0$  point can be established at the spindle centerline. But as shown in Figure 4.10, the diamond tool uses a different cutting edge for the centering plug and test specimen components.

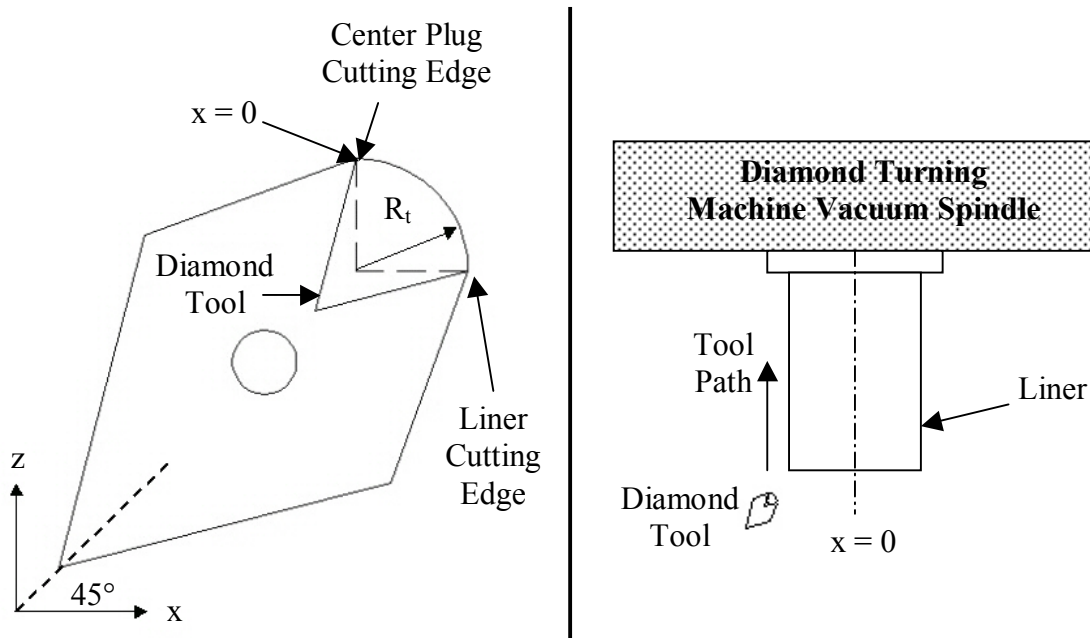


**Figure 4.10** Diamond Turning Machine schematic (top view) for a centered tool used to machine Test Specimen #3 components

Since these cutting edges vary by 90 degrees, the current radius of a cylindrical workpiece was actually the x-axis coordinate *minus* the tool radius,  $R_t$ .

To accurately compensate for the radius of the tool when determining the current cutting x-coordinate, it was necessary to measure the tool radius. To do this, the diamond tool was examined under the Zygo NewView. A set of points falling along the edge of the tool was taken, and a curve was fit to this set of points. The radius of the fitted curve was the tool radius, determined to be  $R_t = 0.4808\text{mm}$ . After measuring the tool, it could then be centered in correspondence to the spindle centerline by machining what is known as a “centering plug”. The Ogive error [7] and resulting feature of this centering plug were measured to determine the tool’s x- and y-position errors, respectively, in relation to the spindle centerline. The tool position was adjusted accordingly using an iterative process and was eventually centered to within  $2\mu\text{m}$  of the spindle height and  $270\text{nm}$  of the spindle x-axis centerline. Whereas the height error was determined by simply resolving the feature diameter using the Zygo NewView (not shown), the Ogive error was determined using the Zygo GPI Interferometer software package. After measuring the machined centering plug under the interferometer and specifying its anticipated radius of curvature, the software package was able to determine the form error and calculate the tool offset automatically, as circled in Figure 4.11.

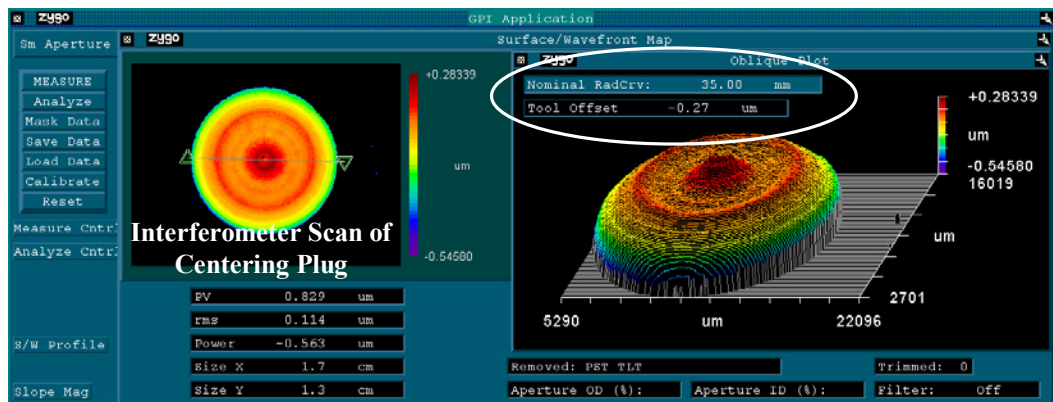


**Figure 4.11** Zygo GPI Interferometer scan of a centering plug showing the ability of the software to automatically determine a tool's x-axis error in relation to the spindle centerline

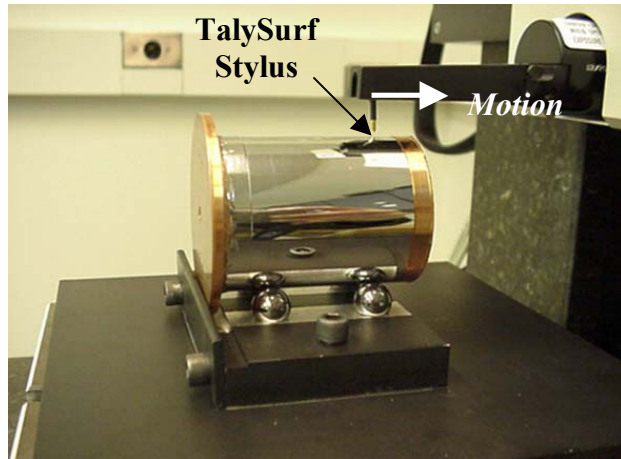
Although the tool's height error was larger than that of the x-axis, the workpiece diametral error resulting from the slightly mis-positioned tool height was negligible. For an OD of 50.414mm, the diametral discrepancy resulting from a tool that is high or low by 2 $\mu$ m is a mere 0.15nm.

Regardless of the accuracy of the tool centering procedure, there is one true advantage behind this measurement technique. Assuming the same tool setup is used for machining each component (which was the case for Test Specimen #3), it ensures that the desired radial interference value can easily be achieved. Even if there were a discrepancy between the centered tool's position and the spindle centerline, such a discrepancy would apply to each of the mating parts, thus maintaining a desired radial interference value. One slight disadvantage of this technique is that there are no *direct* dimensional measurements of the finished components. However, by measuring the shape and features of the machined centering plug, the position of the tool in relation to the spindle centerline can be determined

with a very high degree of certainty. Thus, these centering plug measurements are indirectly applied to determine the radii of each test specimen component. The diamond turned components that were fabricated and measured using this technique are shown in the Appendix in Figure A.7. The graphic portrays the unassembled test specimen components. Note that the copper piece glued to the bottom end of the liner is simply the plug used to attach the aluminum cylinder to the vacuum chuck of the DTM, as explained earlier.

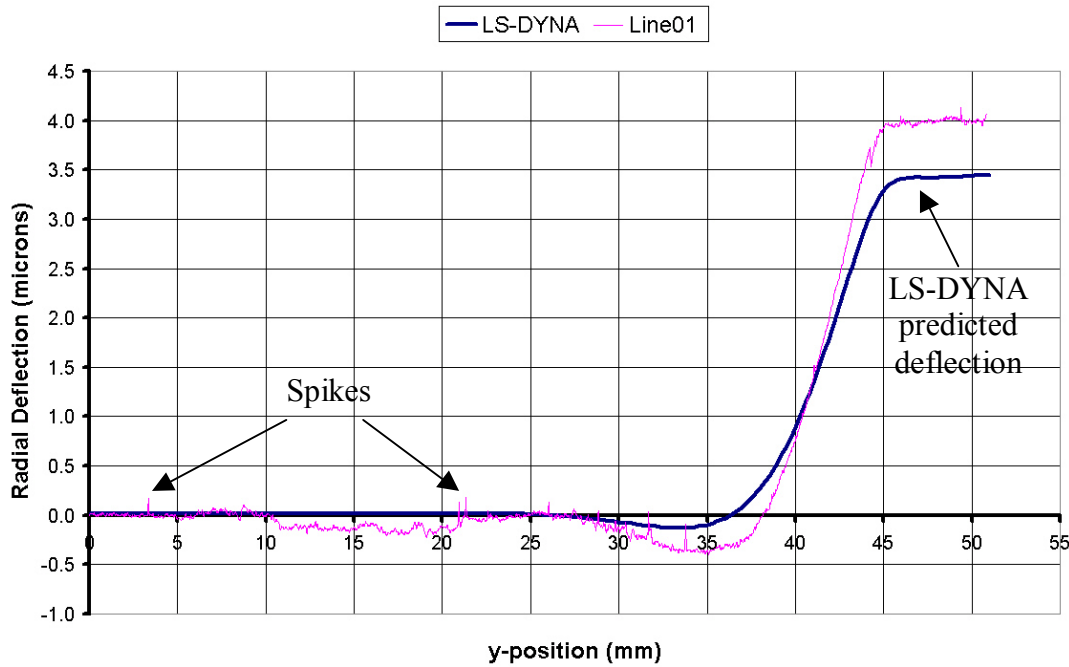
#### 4.3.3 Test Specimen #3: Surface Measurements

It was predicted that the Zygo GPI Interferometer would resolve fringes for this test specimen due to its smaller radial interference value (and therefore a smaller slope in the deflection profile). However, it was found that the interferometer was still unable to gather data for the entire liner length due to the slope of the liner after shrink fit assembly. Thus, the TalySurf Profilometer was used to gather both before and after shrink fit liner profiles, and the difference in these profiles gave the *entire* liner deflection profile. Three lines of measurements were taken around the circumference, each 120 degrees apart in the circumferential direction. Unlike the Zygo Interferometer software, the TalySurf software package does not contain a function that subtracts two data sets, and therefore maintaining the same position of the test specimen was not necessary. A spreadsheet was used to subtract the before and after liner profiles, which were axially translated to align absolute endpoint coordinates, with the liner's free end represented by  $y=0$ . Nonetheless, the kinematic support was still used to hold the test specimen in place while measurements were taken. The TalySurf measurement setup is shown in Figure 4.12.



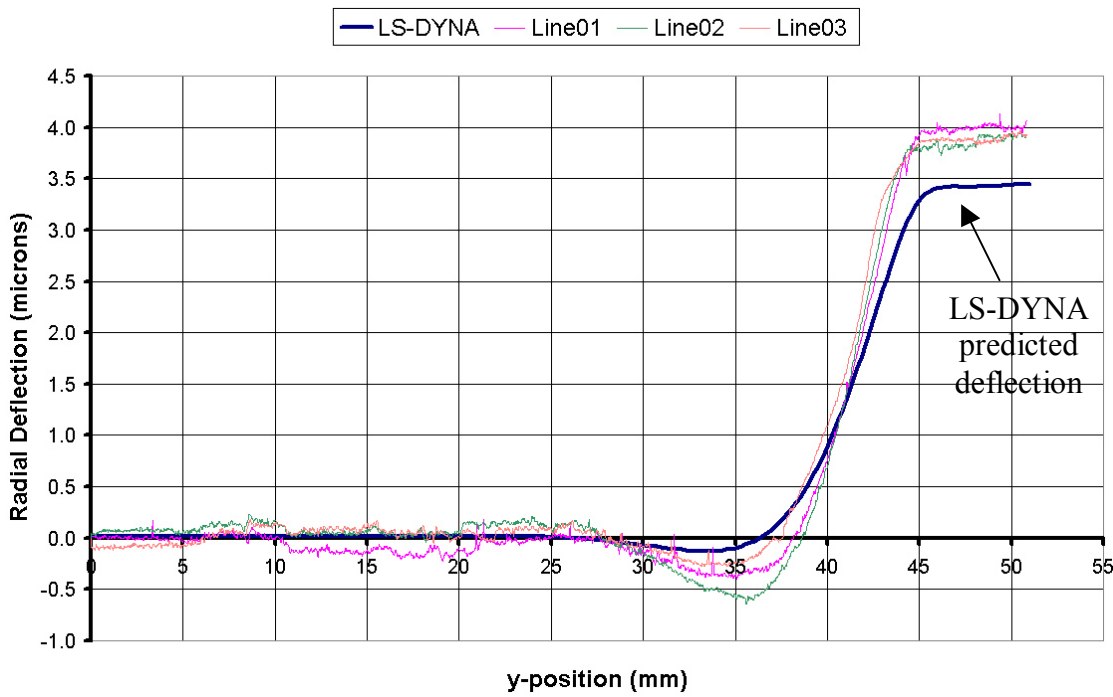
**Figure 4.12** Test Specimen #3 measured by the TalySurf Profilometer

Figure 4.13 shows data taken from one of the measurement lines in comparison to the LS-DYNA liner deflection profile of a model with geometry identical to that of this particular test specimen.



**Figure 4.13** Comparison of LS-DYNA (theoretical) and Test Specimen #3 (experimental) liner displacement values for one line of measurement

It is obvious that the discrepancies between the experimental (“Line01”) and theoretical (“LS-DYNA”) data sets are located at the regions of minimum and maximum liner deflection ( $y$ -position = 35mm and  $y$ -position > 45mm, respectively). However, these are sub-micrometer variations and therefore the data is considered to be excellent. The large, non-periodic spikes seen throughout the length of the experimental liner deflection profile are due to particles that had collected on the diamond turned surface over time. The other two lines of measurement produced very similar favorable results, as seen in Figure 4.14.



**Figure 4.14** Comparison of LS-DYNA (theoretical) and Test Specimen #3 (experimental) liner displacement values for all three lines of measurement

Note that any discrepancies between the experimental and theoretical data sets are within approximately  $0.5\mu\text{m}$ . The  $0.5\mu\text{m}$  difference in experimental and theoretical profiles can be partially attributed to the  $0.27\mu\text{m}$  uncertainty in the x-axis centering of the tool, as described

earlier. It was believed that the orientation of the test specimen on the base of the TalySurf Profilometer could potentially be a source of error as well. Any tilt in the liner,  $\lambda$ , with relation to the motion of the TalySurf stylus would result in undesirable stylus drop-off and therefore inaccurate data. An exaggerated example of a tilted test specimen is illustrated in Figure 4.15.

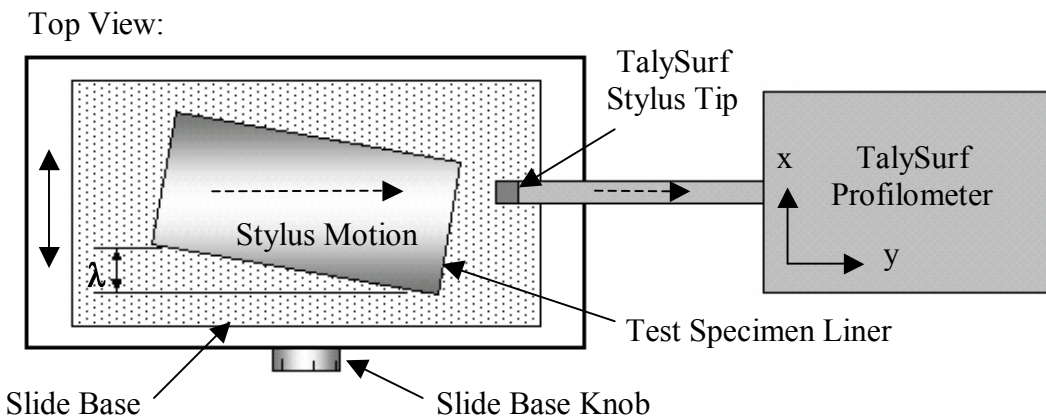


**Figure 4.15** Top view of the TalySurf Profilometer measuring a test specimen liner that is tilted in respect to the stylus motion, producing undesirable stylus drop-off

The test specimen position was adjusted by hand and the orientation of the liner was determined using the following method. After touching off with the stylus on one end of the liner, it was translated in the appropriate x-direction using the adjustable slide base upon which the kinematic support and test specimen were placed (see Figure 4.15). The point of maximum upward stylus deflection represented the peak, or crest, of the liner at that end. The x-position value of the slide base was then recorded. This slide base position was simply defined by the current numeric value of the knob that was used to adjust the x-position. The stylus was then touched off on the opposite end of the liner, and the position

of the slide base corresponding to the liner crest was again recorded. Any discrepancies in the two position values indicated by the knob represented a tilt in the test specimen as indicated by  $\lambda$  in Figure 4.15. The kinematic support that held the liner was then slightly rotated by hand using an iterative procedure to align the y-axis of the liner with the motion of the TalySurf stylus. For each line of measurement that was taken, the locations of the peaks on either end of the liner were aligned to within half of a numeric increment on the slide base knob. Using a Federal gage touching the side wall of the slide base, it was determined that each numeric increment represented  $150\mu\text{m}$  of translation in the x-direction. Simple geometric equations were applied to determine what effect a liner tilted at  $150\mu\text{m}$  would have on the stylus deflection.

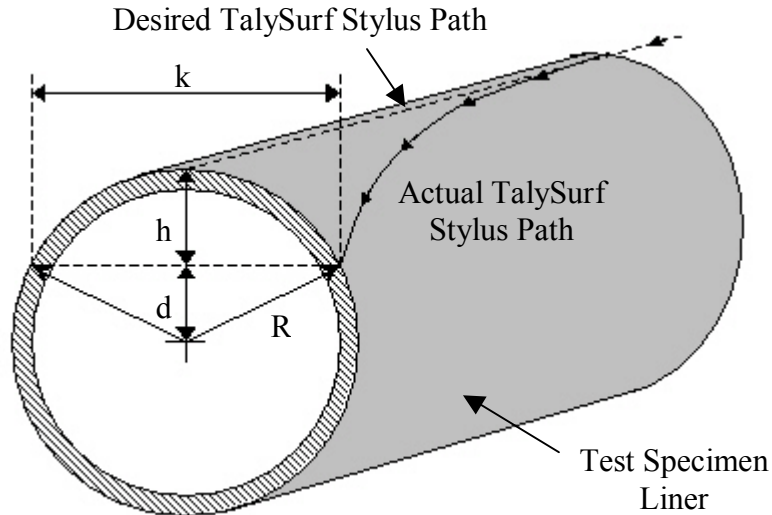


**Figure 4.16** A schematic illustrating exaggerated TalySurf stylus drop-off

$$d = \frac{1}{2} \sqrt{4R^2 - k^2} \quad (20)$$

$$h = R - d \quad (21)$$

Using Equations 20 and 21 with  $R$  equal to the test specimen liner outer radius of 25.207mm and  $k$  equal to 150 $\mu\text{m}$ , the maximum potential drop-off error  $h$  was calculated to be 0.44 $\mu\text{m}$ . Although such a stylus drop-off would have an effect opposite to that of the error shown in Figures 4.13 and 4.14, this was still investigated and considered as a potential measurement error.

Other potential discrepancies between the theoretical and experimental deflection curves include surface finish, material defects, and initial liner shape. The LS-DYNA model consisted of components with perfectly smooth surfaces, which in reality is impossibly to achieve even with the most technologically advanced equipment. The copper and 6061 aluminum that were machined were most likely not isotropic and could also cause localized differences in the deflection plots due to some possible residual stresses. Finally, the initial liner was shape was measured before the shrink fit assembly, as previously explained. The liners were not perfectly cylindrical, with a peak-to-valley (PV) of 0.200 – 0.300 $\mu\text{m}$  in certain lines of measurement along the liner's outer surface for Test Specimen #3 in particular. Such a surface profile from one of the lines of measurement is shown in Figure 4.17, where the PV is 0.205 $\mu\text{m}$ .

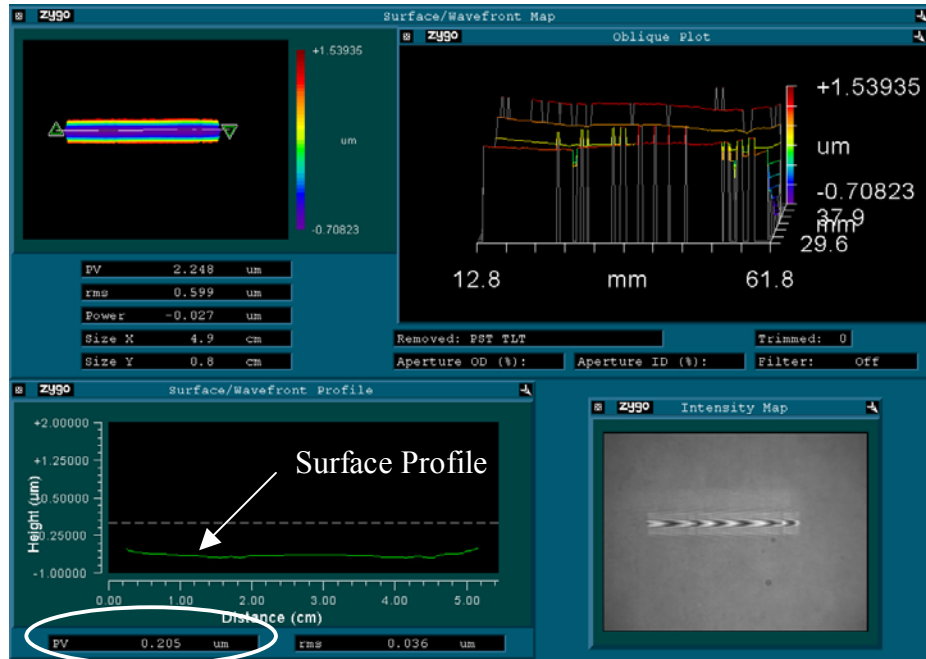


**Figure 4.17** Test Specimen #3 surface profile before shrink fit

All of these were issues for each of the three test specimens that were fabricated. The third and final test specimen provided the most enlightening results, with errors in the sub-micron range over the entire liner length. This error had a handful of potential causes, some of which cannot be resolved. Regardless, the results for the last test specimen in particular provided tremendous aid in validating the LS-DYNA code for modeling partial shrink fits such as the ones seen in the ATLAS design.

## **5.0 ATLAS GENERATION II**

After running several pulsed-power experiments using the ATLAS design previously described, problems were encountered and thus design changes were needed. There were minor complications with the axial alignment of components during the shrink fit assembly, but more important were the problems associated with axial stability during the experiments themselves. The ATLAS Generation I shrink fit geometry lacked support for various components (namely the liner and glide planes) in the axial direction. This often resulted in slippage during the high-energy experiments, sometimes completely separating electrical connections. There was a need for a more robust geometry, and thus ATLAS Generation II was developed.

### **5.1 Finite Element Analysis of ATLAS Generation II**

The conceptual fundamentals behind ATLAS Generation II are identical to the design of Generation I. Large current pulses ( $> 10\text{MA}$ ) are passed through the liner, resulting in a radial implosion. The liner implodes at speeds on the order of 10-20km/s, contacting a target contained within the liner. Major differences in this design include the following: the use of a mechanical press fit rather than a thermal shrink fit for liner/glide plane assembly, modified liner dimensions and overall geometry, and a new mechanism through which current flows from the liner. A cross section of the original design (Phase I) of ATLAS Generation II is shown in Figure 5.1 and Figure 5.2.

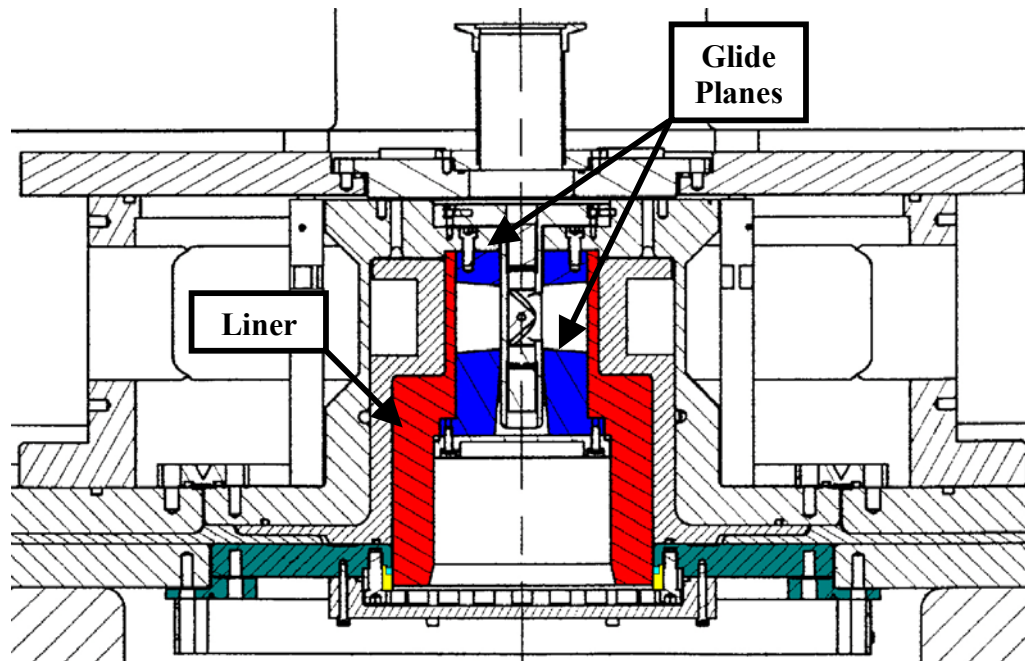


**Figure 5.1** Cross sectional drawing of ATLAS Generation II (Phase I)

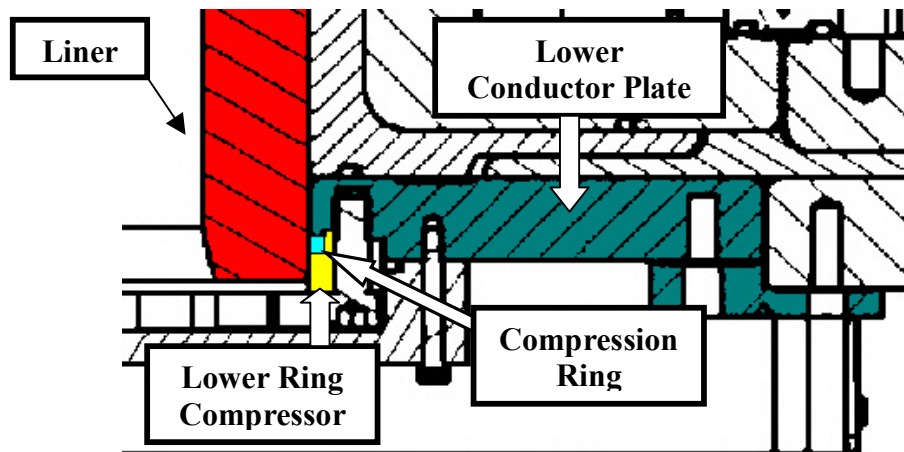


**Figure 5.2** Zoomed view of ATLAS Generation II (Phase I)

One of the major differences of this design is the liner shape. The geometry is no longer cylindrical and lacks the “bump” features on each liner end. The liner dimensions, namely thickness, are easily adjustable during fabrication to meet performance demands determined

by experimental parameters (current magnitude, sinusoidal rise-times, etc). Secondly, the upper glide plane is brought into contact with the liner via a mechanical press fit rather than a thermal shrink fit, as in ATLAS Generation I. Such a design change makes assembly considerably less complicated, and is further explained in Section 5.1.1. Finally, the compression ring acts as the new mechanism to transfer current from the liner to the return conductor plates, where the current circuit is completed. The ATLAS Generation I design used the lower glide plane as the current exit route from the liner. Here, the compression ring is slipped over the end of the liner with 0.254mm (0.010in) of radial clearance. This clearance is compensated for by a sharp tooth on the conductor plate, which distorts the compression ring from the top, thus forcing contact with the liner. The integrity of this interface is vital to the success of the experiments, and therefore the design of the compression ring and its surrounding components (i.e., the liner, ring compressor, and lower conduction plate) are critical. The details of these components are discussed in Section 5.1.2. For directional control of current flow, LANL places a high strength insulation tape around the liner OD in areas of close proximity to the lower conduction plate to ensure that the current flows *only* to the compression ring immediately after exiting the liner.

Once again the system was modeled with LS-DYNA using axisymmetric elements. The parts surrounding the compression ring were slightly altered by LANL to overcome problems with the experiments, mainly unwanted distortion of other components. One such modification was placement of the tooth on the lower ring compressor that distorts the compression ring from the bottom rather than from the top as described earlier. The

geometry of the upper glide plane and liner remained the same through this design transition. The LS-DYNA model of the most recent component geometry is seen in Figure 5.3.

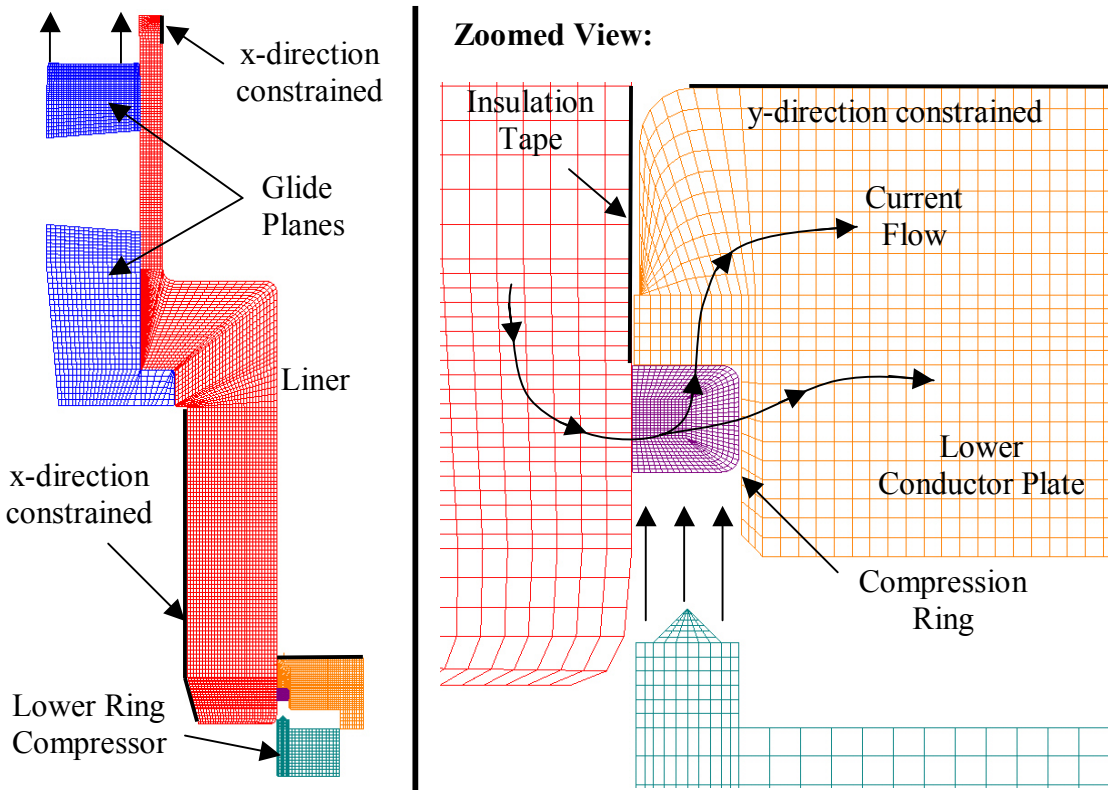


**Figure 5.3** ATLAS Generation II finite element mesh (final design iteration)

The glide planes are composed of copper, the liner and compression ring are 1100 aluminum, the lower conductor plate is 6061 aluminum, and the lower ring compressor is composed of 304 stainless steel. The pertinent properties for these materials are listed in Table 1 (Section 2.3.1) and Table 12.

**Table 12** Properties for new materials used in the ATLAS Generation II model

	<b>304 Stainless Steel</b>	<b>6061 Aluminum</b>
Young's Modulus	$2.850 \times 10^7$ psi	$1.000 \times 10^7$ psi
Poisson's Ratio	0.29	0.33
Yield Strength	31,200 psi	40,000 psi

The six components shown in Figure 5.3 are the ones of greatest interest for analysis, and the number of elements used for each of these components is listed in Table 13.

**Table 13** Number of elements used in the ATLAS Generation II model

<b>Component</b>	<b># of Elements</b>
Liner	5,002
Small Glide Plane	1,179
Lower Conductor Plate	1,155
Compression Ring	775
Large Glide Plane	774
Lower Ring Compressor	471
<i>Total Elements</i>	9,356

As seen in Figure 5.1 there are several other surrounding components that were not modeled. The particular version of LS-DYNA that was used allows for only 10,000 elements to be included for each model. Since this limit for the maximum number of available elements is quickly approached with these six components, x- and y-directional constraints (radial and axial constraints, respectively) were used as an alternative for simulating the presence of the surrounding parts. The locations of these constraints are illustrated in Figure 5.3. The radial constraint located at the bottom of the liner represents

the lower glide plane's new geometry, which is not depicted in Figure 5.1. The most recent ATLAS design extends the lower glide plane to the bottom end of the liner. This glide plane is slipped into the liner with a slight clearance and simply provides radial support to prevent undesirable implosion in this bottom region (the liner is designated to only implode in the region between the two glide planes). To provide the opportunity to include the other surrounding parts, the number of elements could have been reduced for each of the six components listed. But doing so could have sacrificed simulation accuracy since it was previously determined that finer meshes provide superior results.

### 5.1.1 Upper Glide Plane / Liner Interaction

During the assembly process, a ring of bolts executes the small glide plane's upward motion and torque specifications are used to indicate the final axial position of the glide plane. A geometric interference created by a radially tapered liner ensures contact with this upper glide plane, which is essential for proper current flow from the glide plane into the liner. The geometric overlap between these two components can be seen in the Appendix in Figure A.8.

To simulate the glide plane's upward motion, a displacement was imposed on a node corresponding to the location of the bolt centerline. An additional, equivalent displacement was imposed on the top node located at the inner radius of this glide plane to prevent detrimental rotation in the FEA model. The locations of these displacement vectors are shown in Figure 5.3, and the magnitude of these displacements was such that the final axial

position of the glide plane mimicked that of the actual assembly. A plot of the radial stress contour for this region can be seen in Figure 5.4. Note the highly localized stress concentration, which coincides with the relatively small region of radial interference between the two components (Figure A.8). Also note the equilibrium of the stress distribution between the two components near this interface.

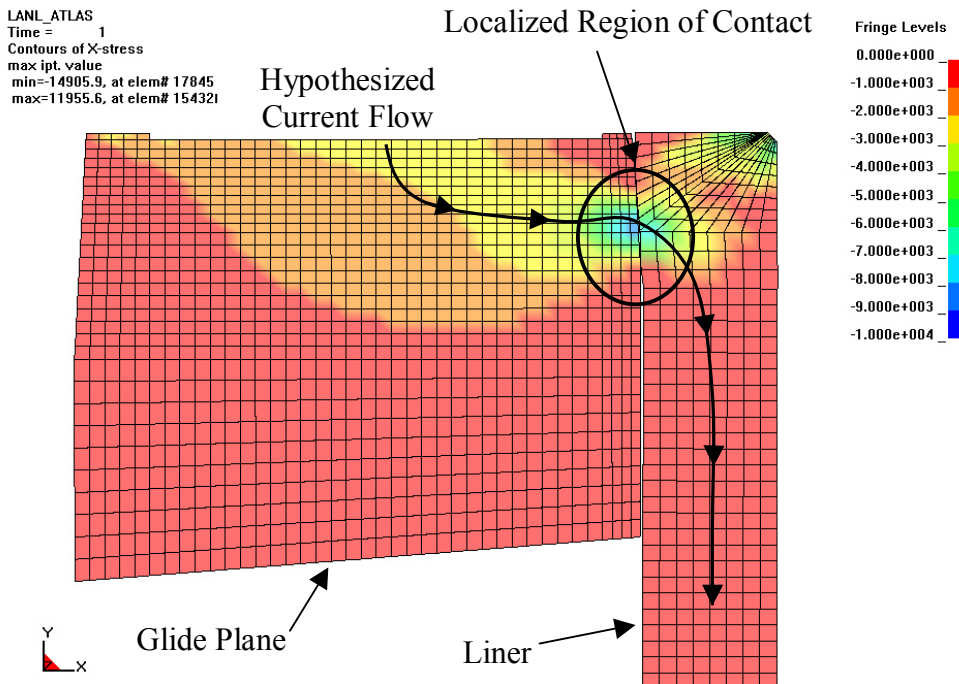


**Figure 5.4** Radial stress (x-stress) of liner/glide plane interface for ATLAS Generation II

The maximum radial stress is approximately 9,500psi. The hoop stress contour plot has a very similar distribution (though not shown) and suggests a maximum hoop stress of approximately 7,700psi. Therefore, some localized yielding occurs in the 1100 aluminum liner, but not in the mating glide plane.

It was believed that LS-DYNA might not accurately model the shearing action of these two components, as some material loss could be experienced on the surface of the liner and/or glide plane. It is likely that such a situation would not be correctly modeled by the LS-DYNA code. Therefore, as an alternative for modeling ATLAS Generation II, a thermal shrink fit was simulated with this same geometry. Imposing a temperature change of -200°C on the glide plane was not sufficient for overcoming the radial interference of this particular geometry, so an increased temperature gradient of -1000°C was used instead. This temperature drop is not feasibly achievable in reality but was not a concern since this particular simulation was used simply for comparison with the mechanical fit assembly simulation. This was not a suggestion to alter the assembly process. The shrink fit simulation yielded very similar results, with almost identical stress contour plots, and similar maximum radial and hoop stresses of 10,500psi and 7,800psi, respectively. Thus, for the top liner/glide plane interface it was concluded that the method of modeling (whether press or shrink fit) bears no significant effect, and the results were presumed to be accurate.

### **5.1.2 Compression Ring Modeling**

During these pulsed-power experiments, the current flows from the top glide plane to the liner, and exits the liner via the compression ring. The integrity of the contact between the compression ring and the liner is contingent on the action of the lower ring compressor. A sharp tooth located on the ring compressor acts as a mechanism to distort the compression ring, thus forcing contact with the adjacent liner. A contour plot of the radial stress is shown in Figure 5.5. The stress distribution and magnitude in the radial direction were used to

gauge the contact integrity of the compression ring's y-faces (interfaces ① and ②), whereas the axial stress distribution and magnitude were used to gauge contact of the ring's x-face (interface ③).

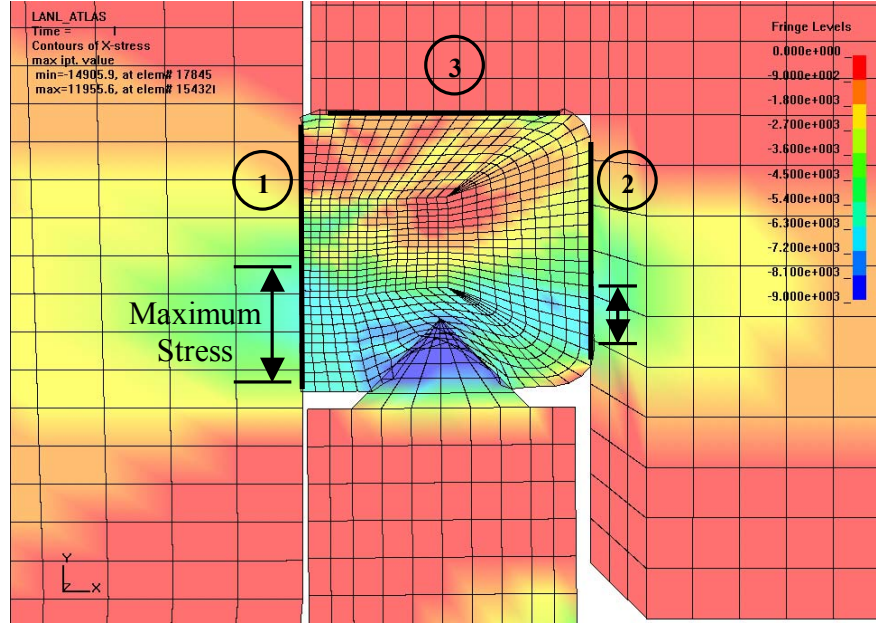


**Figure 5.5** Radial stress (x-stress) in the compression ring for ATLAS Generation II

Although the grayscale image of the contour plot is not adequately indicative of the stress behavior, the stress level in the y-faces of the compression ring is a maximum at the regions near the tooth of the ring compressor. Moving in the positive y-direction along these same faces yields smaller radial stresses. Such a trend suggests a tapered compression ring, which indeed coincides with the shape of the ring compressor's tooth. It is clear that the tooth directly affects the stress levels along each interface, and therefore alternative shapes for this feature were investigated. Since current flows through each of these three interfaces as illustrated in Figure 5.3, it is important to maximize the level of contact in these regions. By

altering the shape of this tooth and investigating the average stress x-stress along interface ① and ②, and the average y-stress along interface ③, it can be determined which geometry changes should be made. This investigation could be used to possibly enhance the effectiveness of these pulsed-power experiments.

### 5.1.3 Suggested Geometric Changes in the Lower Ring Compressor

Three new geometries of the lower ring compressor were modeled for the purpose of investigating which models, if any, improved contact on the three pertinent interfaces of the compression ring. These geometries included a sharper, narrower tooth (Redesign #1); a tooth with a flat top surface (Redesign #2); and a shorter, wider tooth (Redesign #3). These geometries were chosen arbitrarily to investigate the effects of such alterations. They are shown in Figure 5.6.

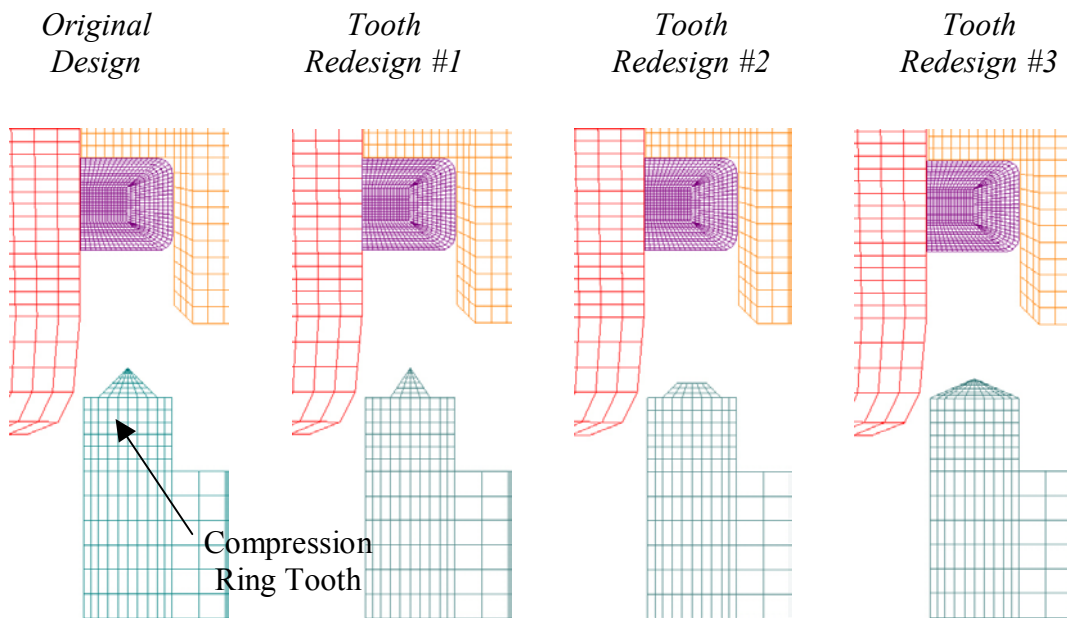


**Figure 5.6** Design changes suggested for the ring compressor's tooth geometry

As explained in the previous section, the average stress values of elements along each interface were determined. The stress direction normal to the give surface direction was used. Average radial stress (x-stress) was calculated for the inner and outer vertical faces of the compression ring, and average axial stress (y-stress) was calculated for the top, horizontal surface. A larger average stress over a given interface would suggest enhanced contact with the mating component on that particular surface. Stresses of the different designs in comparison to values obtained from the original geometry are summarized in Table 14.

**Table 14** Average stress magnitudes of compression ring elements on each interface

	<b>Radial Stress (inner)</b>	<b>Radial Stress (outer)</b>	<b>Axial Stress (top)</b>
Original Design	-3300 psi	-2850 psi	-4500 psi
Redesign #1	-3500 psi	-3000 psi	-4050 psi
Redesign #2	-2900 psi	-2700 psi	-4150 psi
Redesign #3	-2050 psi	-1850 psi	-4250 psi

Whereas the average stress magnitude is quantifiable, it is difficult to quantify the actual level of contact for each interface. The stress levels between each design do not considerably fluctuate, but they do indeed vary. This suggests that the tooth geometry does affect the compression ring interfaces to some extent. Determining which interface integrities are of utmost importance would be vital to determining which redesign, if any, should be implemented in ATLAS Generation II. Regardless, finite element analysis provides the opportunity to further explore alternative geometric designs without the concerns associated with cost and safety.

## **6.0 COMPOSITE LINERS**

Composite liners, i.e. liners composed of two dissimilar materials, have been proposed for use in certain experiments. These liners consist of inner and outer thin-walled cylinders that are press fit together, though cooling is sometimes used to assist the assembly process. The motivation behind the use of composite liners comes from the machining process. Problems can arise when machining thin-walled cylinders, with vibration often encountered during the final tool passes. The current fabrication process for composite liners is such that the inner cylinder wall thickness is much greater during the initial assembly process than the required final dimension, which may also be true for the outer cylinder. The proposed configuration contains an outer cylinder composed of 1100 aluminum with an inner cylinder composed of copper, tantalum, stainless steel, or 6061 aluminum (Figure 6.1). For assembly, a nominal slip fit exists between the mating cylinders over most of their length. The OD of the inner cylinder is machined oversize at one end in order to form a tight joint. This is also the case with the ID of the outer cylinder on the opposite end. Upon completion of this initial machining process, the two components are slipped together using a minimal press force over the final few millimeters of insertion. The ID of the inner component and the OD of the outer component can then be machined with fewer complications, as the press fit joint carries much of the torque induced by the machining process. The final liner product can then be assembled with the glide planes via a shrink fit, as previously described in this thesis.

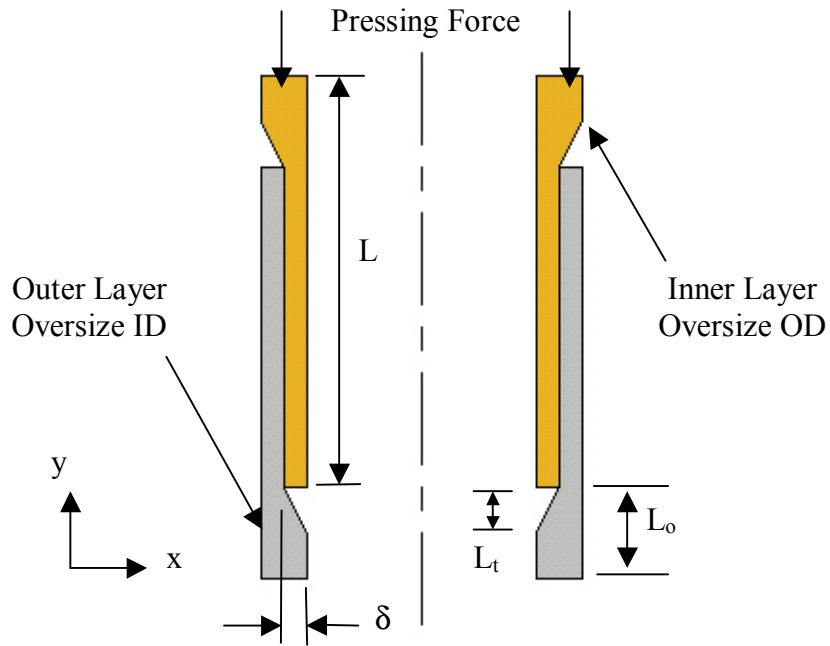


**Figure 6.1** Schematic of a composite liner, shown in configuration just prior to lockup

There were several questions that arose when considering the use of composite liners. Such concerns included: the shape of the transition region and its effect on the contact interface between the two mating components, tradeoffs between press fits and thermal shrink fits, and prevention of yielding with the use of desirable geometric dimensions.

## 6.1 Composite Liner Geometry Effects

There are three main parameters that can be varied in geometry of the composite liners: the overall length of the transition region  $L_o$ , the length of the taper within the transition region  $L_t$ , and the radial interference  $\delta$  that is created by this taper. Each of these parameters was expected to affect the results of interest, and the geometric representations can be seen in

Figure 6.1. To investigate the effects of these varying parameters, LS-DYNA was utilized once again. Axisymmetric models were composed of 8 elements through the thickness of each mating cylinder, thus providing 16 elements through the thickness of the assembled composite liner. Copper and 1100 aluminum were used as the materials for the inner and outer components, respectively. The nodes along the horizontal boundary at the bottom end of the outer cylinder were constrained in the y-direction, allowing for radial displacement only. The nodes along the horizontal boundary at the top of the inner cylinder were subjected to nodal displacements specified in the negative y-direction, which mimicked the pressing action. The displacement occurred over the entire simulation using 100 implicit time steps, and the magnitude of the displacement was such that the cylinder ends were perfectly aligned at the conclusion of the simulation. The moving inner cylinder was also able to deflect in the radial direction, as it was not constrained in any way. Thermal cooling was initially *not* used. It was decided that cooling would only be used if problems arose during the simulation due to excessive interference or sudden surface directional changes that were too extreme to model (i.e., a very short taper length).

The assembled length  $L$  was a constant 51.445mm (2.0254in), similar to the ATLAS Generation I liner length. The inner component had a constant ID of 97.409mm and the outer component had an OD of 100.000mm. The thickness of each component was equal to a constant 0.645mm in the slip fit sections. The overall length of the transition shape  $L_o$  was established at  $\sim$ 7.5mm and also remained constant. Prior to this analysis, very few guidelines for the dimensional range for each of the varied parameters were provided; hence

0.0008in (20.32 $\mu$ m) was chosen as the baseline interference value  $\delta$ . This value closely matched the interference value of  $\sim 15\mu$ m for the liner/glide plane interface in the ATLAS Generation I design. The design analysis began by first altering the taper length. For the selected interference value, five models of varying taper length were generated. A schematic of this shape variation is shown in Figure 6.2.

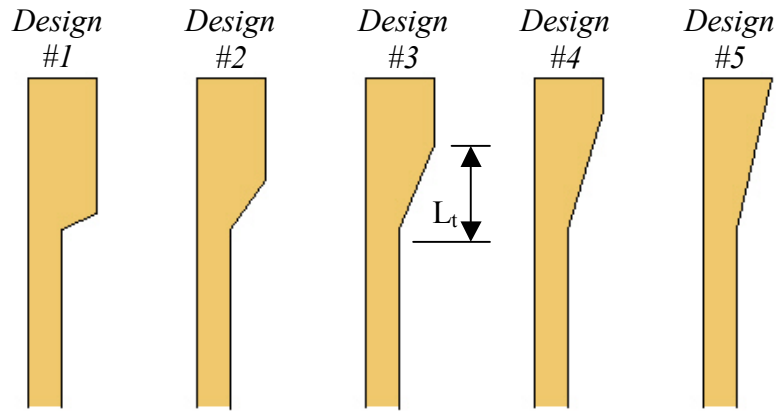


**Figure 6.2** Schematic of a composite cylinder transition shape variation

### 6.1.1 Radial Gap Analysis

The interfaces of each of the assembled composite liner designs were first investigated. Gaps between the mating components were deemed undesirable, as they would obviously limit contact and therefore lower the integrity of the press fit. To do this, final x- and y-coordinate locations of the nodes along the interface (along the inner cylinder OD and the outer cylinder ID) were plotted for the final time step in the simulation, which represented the state of completed assembly. Plots for three of these designs are shown in Figure 6.3.

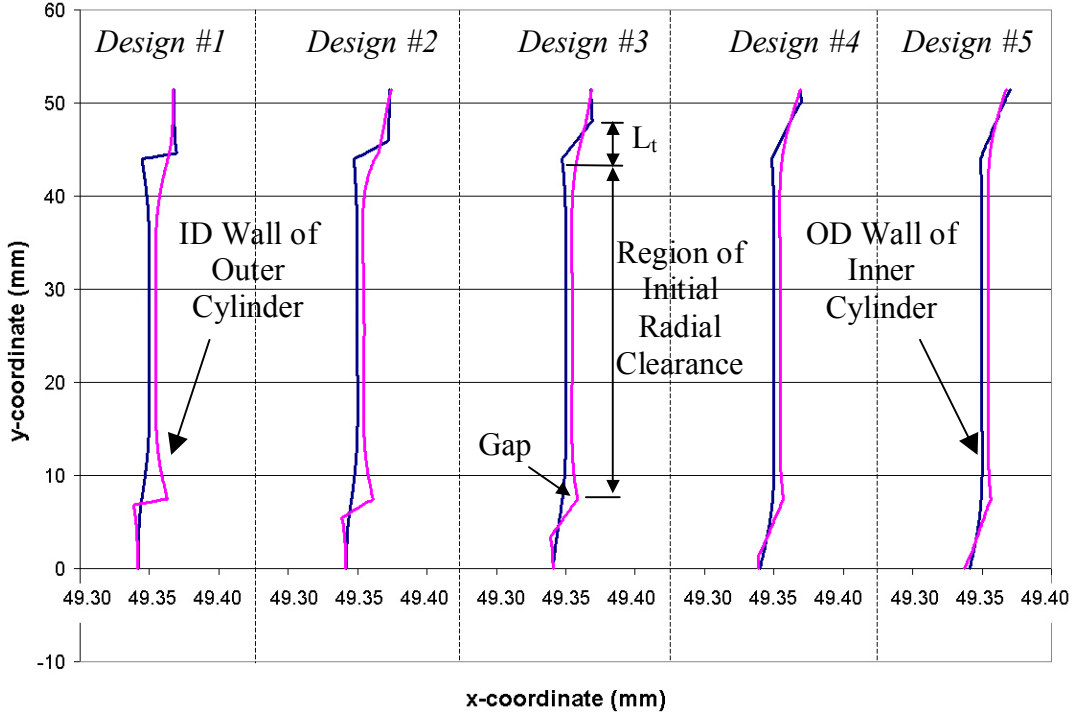


**Figure 6.3** Nodal coordinate locations after composite liner assembly for nodes falling along press fit interface ( $\delta = 0.0008\text{in}$ ,  $20.32\mu\text{m}$ )

Similar to an actual composite liner, the LS-DYNA model included an initial radial clearance ( $5\mu\text{m}$ ) between the inner and outer cylinder walls. This clearance existed in the region between the transition shapes located at either end, which is somewhat evident in the plots in Figure 6.3. It is clear from these plots that with a shorter taper length  $L_t$  comes a larger gap. To quantify this, the maximum radial distance between the inner and outer components was determined. This maximum separation was consistently located at the point where the radial taper begins, when moving from the cylinder's mid-length position towards the free end. These gap sizes are summarized in Table 15.

**Table 15** Maximum radial separation between inner and outer cylinders in a composite liner ( $\delta = 0.0008\text{in}$ ,  $20.32\mu\text{m}$ )

	Design Number				
	#1	#2	#3	#4	#5
Gap Size	20.1 $\mu\text{m}$	15.0 $\mu\text{m}$	12.5 $\mu\text{m}$	7.6 $\mu\text{m}$	5.0 $\mu\text{m}$

The results are indeed intuitively sound. A more gradual taper allows for the mating cylinders to remain in contact over a greater percentage of the overall length, thus reducing the gap size. Such a reduction in gap provides a stronger composite liner that can carry more torque induced by the final machining of both components.

### 6.1.2 Radial Deflection Analysis

Another important aspect is the radial deflection profile for both the inner and outer cylinders. During assembly, a great deal of precision is needed to slip the glide planes into the ends of the liner, and therefore dimensional accuracy is essential. Aligning the components is not trivial, as the radial clearance provided by glide planes' shrinkage is in the sub-millimeter regime. Liners having radial symmetry are beneficial for previously described reasons, but axial symmetry is equally as important. Since there are two glide planes involved in the assembly process, having identical liner shape profiles on either end would be ideal. For example, consider an incorrectly machined liner (not necessarily composite) whose final dimensions are slightly skewed thus giving effective interferences that are not equal at each end. This would undoubtedly result in a warped liner whose radial deflection profile is not symmetric about the liner mid-length, which could very well effect the radial implosion of the liner during the pulsed-power experiments.

With the composite liners, it is conceivable that the radial deflection profile would *not* be symmetric about the liner mid-length for certain designs. The thickness of both the inner and outer cylinder is not consistent through the length in these designs. The thicker end of each component is slightly stiffer, thus resulting in a decreased radial deflection. The effect of the transition shape on the radial deflection profile was investigated with the finite element models. The radial deflections for the ID and OD walls of the inner and outer cylinders, respectively, were analyzed for each successive design with  $\delta=20.32\mu\text{m}$ . Illustrations of the radial displacement vectors for nodes along the inner and outer wall of the assembled liner are shown for Design #1 and Design #5 in Figure 6.4.

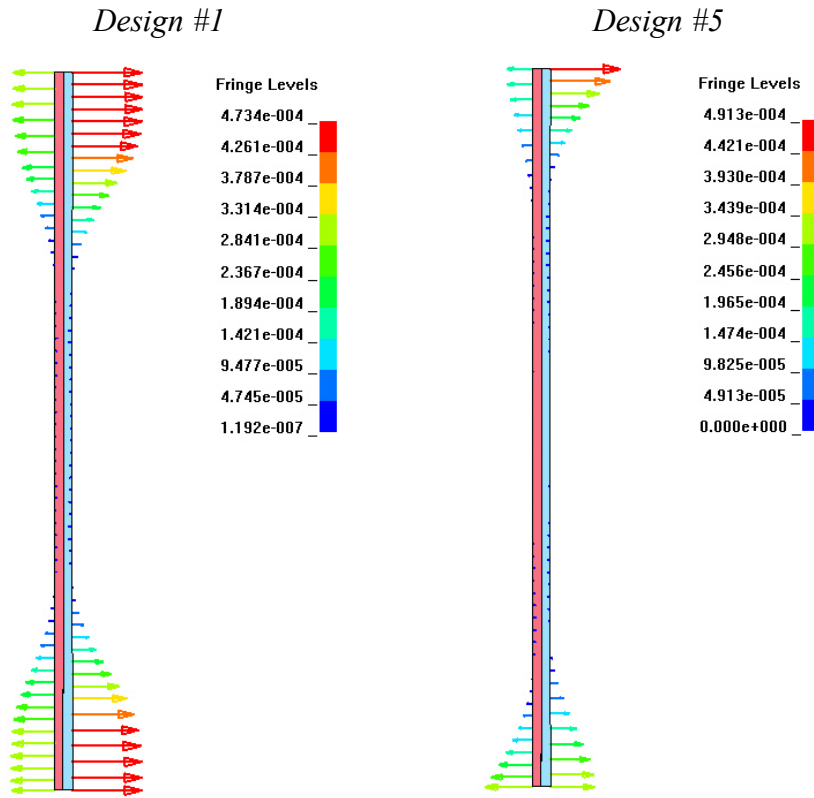


**Figure 6.4** Radial deflection vectors for nodes on the inner and outer composite liner walls for Design #1 and Design #5 ( $\delta= 0.0008\text{in}$ ,  $20.32\mu\text{m}$ )

Note that the fringe levels are in units of inches. In Design #1, both the inner and outer walls exhibit excellent symmetry about the liner mid-length, whereas Design #5 does not. This lack of symmetry seen in Design #5 could pose problems as explained earlier. Although the symmetry seen in Design #1 is favorable, recall that the gap created by this same design was the largest of all designs, in fact 300% more than in Design #5. An unbiased balance of these results was concluded to be reasonable, and therefore Design #3 was chosen for the purposes of an acceptable gap magnitude *and* axial symmetry of radial deflection. The quantitative plot of the radial deflection is shown in Figure 6.5. For aesthetic purposes, the negative of the inner radial deflection curve was plotted even though the deflections occur in opposite directions, similar to what is illustrated in Figure 6.4.

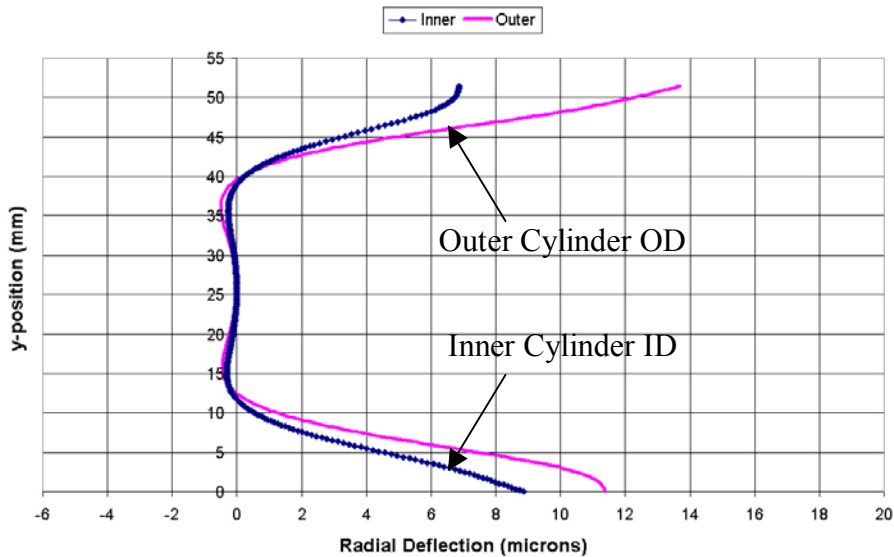


**Figure 6.5** Radial deflection profiles for ID and OD of the inner and outer composite liner cylinders for Design #3 ( $\delta=0.0008\text{in}$ ,  $20.32\mu\text{m}$ )

Since the ID of the inner cylinder and the OD of the outer cylinder are initially straight with no radial variation, these deflection plots essentially represent the final shape of each wall

after assembly. The variation in deflection for the nodes located at the ends of the outer cylinder (at  $y$ -position = 0mm and  $y$ -position = 51.445mm) is 2 $\mu\text{m}$ , and the inner cylinder end deflection variation is approximately the same. This limited variation, along with the relatively small gap of 12.5 $\mu\text{m}$  (when compared to designs with more desirable radial deflection symmetry), suggested that a design of this type is most desirable. However, it was still necessary to investigate one final aspect: stress distribution.

### 6.1.3 Stress Analysis

Determining the peak stress in these designs is important to ensure no yielding of either component. Once again the hoop stress component was determined to be the maximum stress, and thus was used as the design criteria to determine if there is indeed material yielding. Design #3 with a radial interference value of 20.32 $\mu\text{m}$  was chosen to be the most desirable design thus far and was therefore analyzed. As expected, the maximum stress (2,773psi) occurred in the outer aluminum cylinder at the region of maximum radial deflection, located at the top end (see Figure 6.5). This is considerably lower than the yield strength of 1100 aluminum (5,000psi) and therefore yielding does not occur. This suggested that Design #3 remained satisfactory, but the effect of the transition shape on stress levels was still unknown. Each of the five designs for this particular radial interference value was analyzed, and the results of maximum hoop stress are plotted in Figure 6.6. Similar to Design #3, the maximum stress values occurred in the outer aluminum cylinder at the region of maximum deflection for each design.

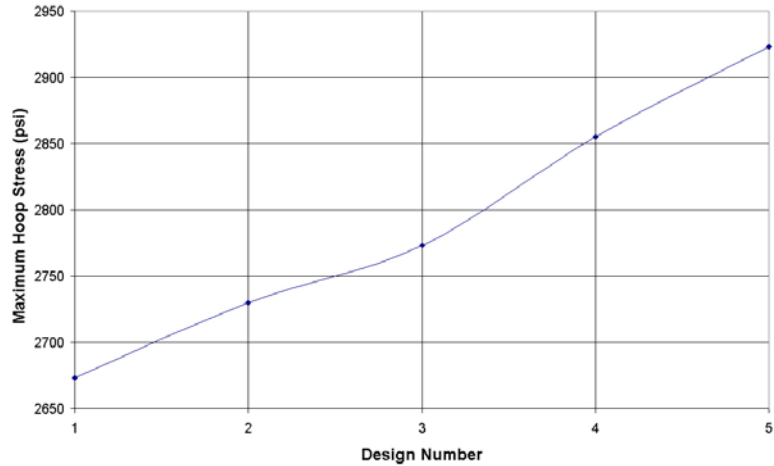


**Figure 6.6** Variation of maximum stress with each design ( $\delta = 0.0008\text{in}$ ,  $20.32\mu\text{m}$ )

The trend is approximately linear, with very little variation in each design for this particular radial interference. Although the stress levels did not play a role in the selection of a suitable design, Design #3 was still chosen for reasons based on gap size and radial deflection symmetry. The final geometric parameter that affects these results is radial interference magnitude. For various interference values, Design #3 was investigated and a summary of results is shown in Figure 6.7.

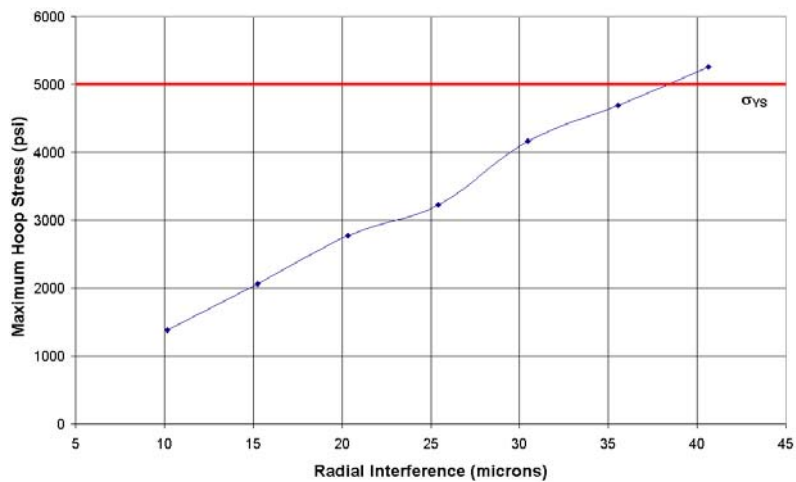


**Figure 6.7** Maximum stress with a variation in radial interference (Design #3)

Clearly, smaller radial interference values cause less deflection and less stress. However, there is a tradeoff between this and the integrity of the joints, as larger interference values create more robust composite liners that would be able to carry more torque during the machining process. Machining parameters such as tool selection and spindle speed were not provided, but these parameters could be used to determine cutting forces and induced torque magnitudes. From these, the proper radial interference value could be selected. It should be noted that the cylinders themselves are very light; hence the weights alone were not predicted to create slippage in the axial direction for the range of radial interference values that was investigated (approximately 10 to 40 $\mu$ m). A balance between tolerable radial deflection, maximum stress in comparison with the material yield strength, and machinability would be used to select an appropriate radial interference value. Nonetheless, it is strongly suggested that Design #3 would produce the most desirable results, regardless of the selected interference.

## **7.0 CONCLUSIONS**

### **7.1 Standard Shrink Fit Modeling**

From the shrink fit simulations in which the inner cylinder was incrementally extracted, it was determined that stress and deflection profiles are indeed difficult to predict, as expected. Analytical formulas should not be used, though deflection and stress values in the regions of contact with mating cylinders closely resemble results given by these formulas (less than 10% difference). For shrink fit problems modeled in LS-DYNA, the use of more elements provides more accurate results. Therefore, it is suggested to fully utilize the number of elements available in the given LS-DYNA version whenever possible, particularly concentrating on the use of fine meshes in regions of interest (i.e., in shrink fit contact regions and in thin-walled components).

### **7.2 ATLAS Modeling**

#### **7.2.1 Radial Deflection Prediction and Compensation**

The radial deflection of the liner behaves such that the maximum deflection occurs at the liner ends where the shrink fit joints are located, and decays in an exponential fashion when approaching the mid-length position. At this point the deflection is slightly radially inward, which is understandable based on analytical models that closely resemble the pressure distribution experienced in the liner. It was determined that this radial deflection can be

compensated by using a liner that is not cylindrical before the shrink fit assembly. Machining a liner that has a pre-assembly shape that “counteracts” the predicted radial deflection profile produces excellent post-assembly results. Implementing such a liner reduces the post-assembly peak-to-valley from  $15.77\mu\text{m}$  to  $1.34\mu\text{m}$  in the radial direction. It is surmised that having a much straighter liner wall after assembly (which is true with this suggested design) would result in improved ATLAS performance, as the liner implosion would occur more uniformly.

### **7.2.2 Interface Gap Prediction and Compensation**

The bump features on the liner ends were found to serve a very useful purpose. Removing these features results in liner yielding and significantly increases radial gaps seen in liner/glide plane interfaces. The liner design for ATLAS Generation I results in gaps of approximately 150nm whereas removing the features creates gaps of 500nm. These voids are singular in each liner/glide plane interface and occur at the glide plane corners where the liner shears and separates during the pulsed-power experiments. Using a longer, more slender feature or a thicker feature essentially eliminates these gaps. It is predicted that gap reduction or elimination could be beneficial in that conductivity between the liner and glide planes could be maximized.

## **7.3 Finite Element Verification**

### **7.3.1 Radial Measurement Techniques**

The finite element models were adequately verified. Three partial shrink fit test specimens that closely resembled the ATLAS liner were fabricated, and the radial dimensional measurement technique was improved for each successive test specimen. For shrink fit systems with small radial interferences ( $<20\mu\text{m}$ ), measuring radial dimensions with calipers or micrometers (Test Specimen #1) is extremely unreliable as they lack the resolution necessary to achieve such precise dimensions. Radial dimension uncertainties were concluded to be on the order of tens of micrometers. The measurement technique for Test Specimen #2 that employed the ASG-2500 DTM, a gage block stack, and a Federal gage was much more accurate, with radius measurement uncertainty of approximately  $2\mu\text{m}$ . It was concluded that this was still not adequate, particularly for systems with radial interferences of approximately  $2\mu\text{m}$ . Test Specimen #3 used an indirect measurement technique that involved centering the diamond tool and using the DTM x-axis coordinate of the final pass to determine the radius of each component. The tool was centered to within 270nm of the spindle centerline, with the dimensional uncertainty falling in the sub-micron regime.

### **7.3.2 Radial Deflection Measurements**

The TalySurf Profilometer and Zygo GPI Interferometer were both concluded to be sufficient for liner surface measurements. The TalySurf lacks the software ability to

automatically subtract before and after data profiles (which is necessary to obtain the radial deflection profile) but the interferometer is unable to resolve fringes for test specimens with larger slopes due to increased radial interference magnitudes. Thus, there are tradeoffs between instrument selection.

Discrepancies between experimental and theoretical deflection profiles were attributed mainly to errors in radial dimensions of the test specimen components. Test Specimen #1 yielded a difference in these curves of approximately 14 $\mu$ m. Test Specimen #2 exhibited tremendous improvement with a maximum difference of 300nm at any point along the deflection profile. However, the complete range of this deflection profile was not available due to the interferometer's inability to resolve fringes (this particular test specimen liner slope was too large). Test Specimen #3 successfully verified the liner deflection predicted by an LS-DYNA model of corresponding geometry. The maximum difference in experimental and theoretical radial deflection profiles for this test specimen was approximately 500nm. Although this difference is slightly more than that of Test Specimen #2, the entire deflection profile was indeed obtained. In addition, achieved repeatability is higher with centering the tool, as the uncertainty is lower. From Test Specimen #3 in particular, it was concluded that LS-DYNA is able to model partial shrink fit systems such as ATLAS with a high degree of accuracy and reliability.

## 7.4 ATLAS Generation II Modeling

### 7.4.1 Small Glide Plane / Liner Interface

For the current ATLAS design, the liner interface created by the small glide plane was modeled with success. The glide plane's upward motion induced by torque specified bolt tightening was mimicked well with nodal displacements in the axial direction. The radial and hoop distributions were intuitively sound, with highly localized symmetry around the region of interference cased by the inward taper of the liner. The maximum stress of 9,500psi indicates yielding in the 1100 aluminum liner, but no yielding is experienced in the mating copper glide plane. This yielding is not expected to effect performance, as contact is maintained in this interface.

### 7.4.2 Compression Ring Distortion

LS-DYNA successfully modeled the deformation of the compression ring, though more time steps (1000 instead of 100, as used in the ATLAS Generation I simulations) were needed. The radial stress in the compression ring and its surrounding components is a maximum at the bottom of the vertical interfaces, where the compression tooth is located. A decaying stress distribution in the positive y-direction suggests a radially tapered compression ring after deformation, which agrees with the shape of the compression tooth. This radial stress decay suggests weakened contact with the adjacent components, and hence could affect current flow. Tooth geometry redesigns were analyzed and average stress values of elements along each of the three interfaces were determined. Comparison of average stress was deemed a reasonable way to quantify and compare contacts within each interface. It

was concluded that a sharper, narrower tooth slightly increases the contact for the inner and outer vertical compression ring walls. Such a redesign slightly reduces the contact for the top horizontal interface. Therefore, determining the importance of each interface could provide aid in determining which tooth redesign, if any, is most desirable.

## 7.5 Composite Liners

For the composite liners, it was concluded that Design #3 is most desirable regardless of the selected radial interference value. This design contains an average liner taper length when compared to the other four designs. While Design #1 exhibits superior radial deflection symmetry about the liner mid-length, Design #5 produces the smallest gaps along the interface of the nested cylinders. It is concluded that having an assembled composite liner shape that is axially symmetric about the mid-length position would lessen assembly complications when the glide planes are inserted. Smaller gaps suggest joints with increased strength, which is important for the post-assembly machining process involved with composite liners (joints with smaller gaps can carry more torque induced by machining). Hence, Design #3 is selected based on its balance between gap size and radial deflection symmetry.

For this design, the other parameter that can be altered is radial interference magnitude. Conclusions related to the selection of interference were not made, since machining parameters were not provided. From these parameters, torque loads along the composite liner interface could be determined. With this, a radial interference magnitude could be

selected, as composite liners with greater interferences could carry more torque, and vice versa. Once again, there is a tradeoff between the ability to carry large torques and the undesirable increased radial deflection that comes with a greater interference magnitude. It is evident that the dimensions of the transition shape greatly influence these results of interest, and FEA proves to be a tremendous aid for investigating composite liners along with various other components involved in ATLAS.

## LIST OF REFERENCES

- [1] Turchi, Peter J., et al. "Design, Fabrication, and Operation of a High-Energy Liner Implosion Experiment at 16 Megamperes." *IEEE Transactions on Plasma Science* 30.5 (October 2002): 1777-88.
- [2] Turchi, Peter J. "Problems and Prospects for Microsecond Pulsed Power Above Ten Megamperes." *IEEE Transactions on Plasma Science* 28.5 (October 2000): 1414-21.
- [3] Kanzleiter, R.J., et al. "Using Pulsed Power for Hydrodynamic Code Verification." *IEEE Transactions on Plasma Science* 30 (2002): 1755-63.
- [4] Turchi, Peter J., and W.L. Baker. "Generation of High Energy Plasmas by Electromagnetic Implosion." *Journal of Applied Physics* 44 (1973): 4936-44.
- [5] Budynas, Richard G. *Advanced Strength and Applied Stress Analysis*. 2<sup>nd</sup> ed. Boston: McGraw Hill, 1999.
- [6] Timoshenko, S. *Theory of Plates and Shells*. New York: McGraw-Hill Book Company: 1959.
- [7] Gerchman, Mark. "Fundamental Axial Spindle Motions and Optical Tolerancing." *SPIE Proceedings* 1573 (1992): 49-52.

## APPENDIX A

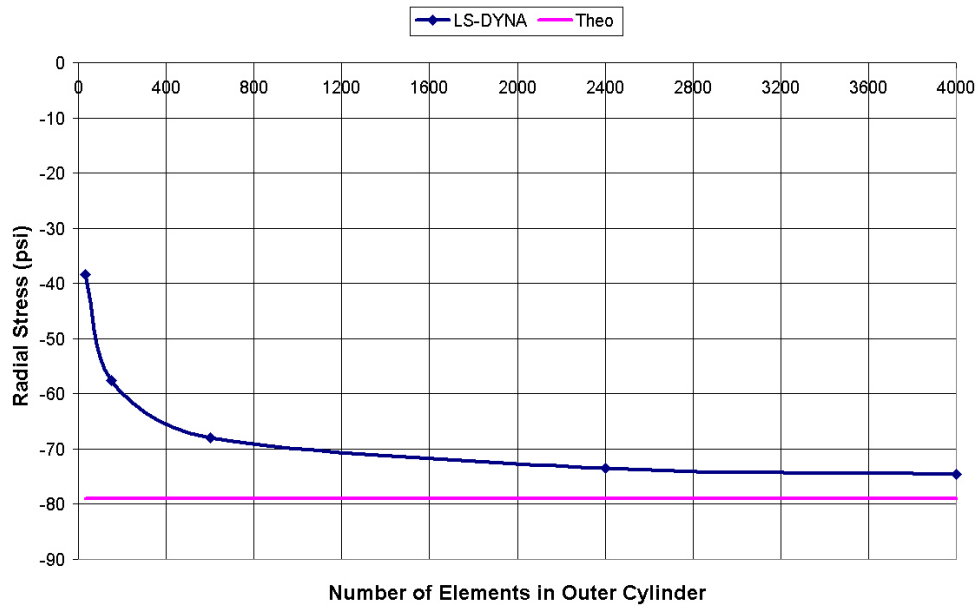


**Figure A.1** Convergence of outer cylinder radial stress with an increasing number of elements

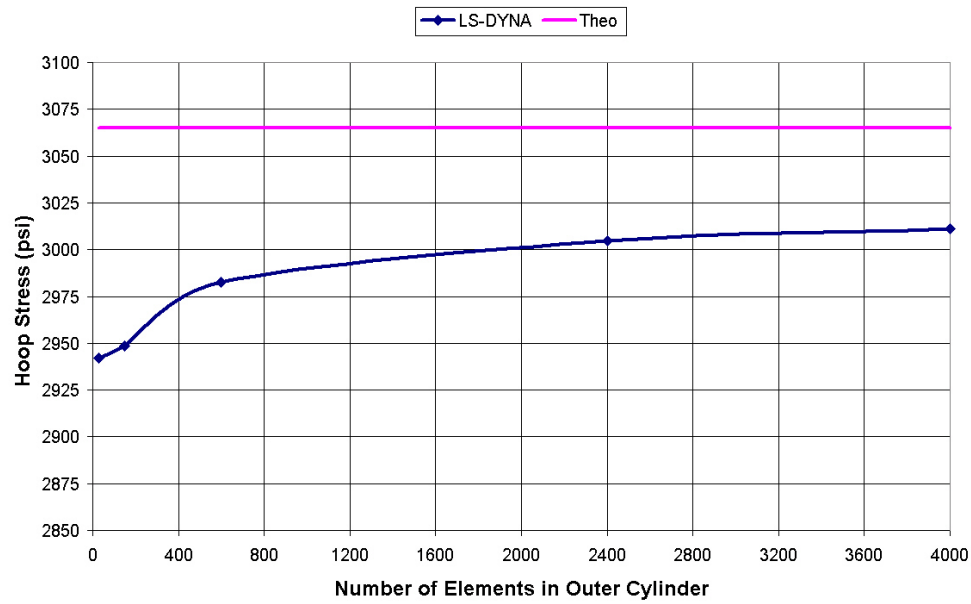


**Figure A.2** Convergence of outer cylinder hoop stress with an increasing number of elements

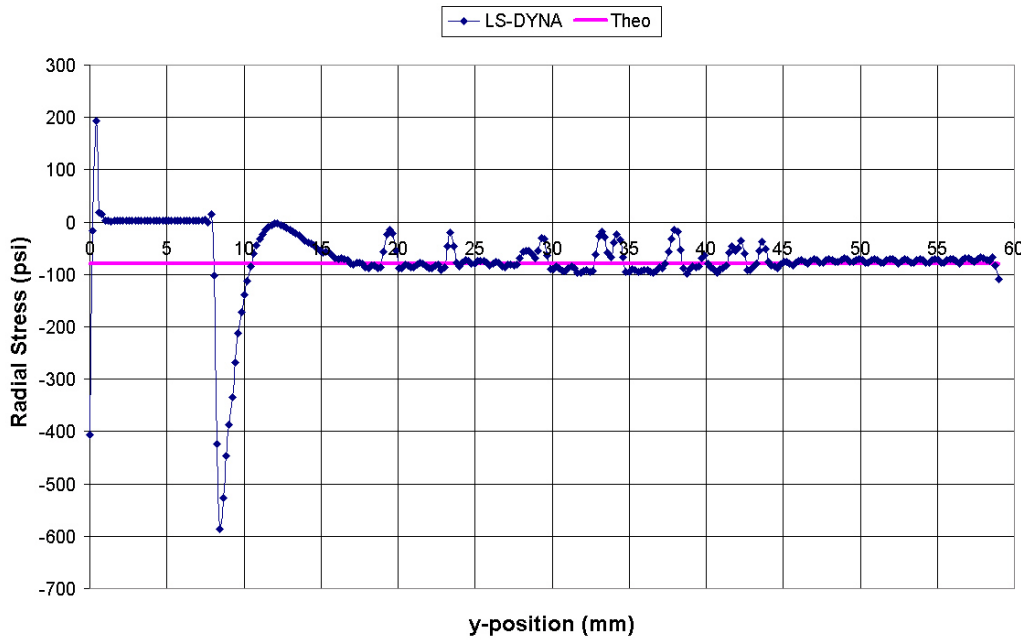


**Figure A.3** Outer cylinder radial stress distribution for shrink fit model #2 with 2400 elements

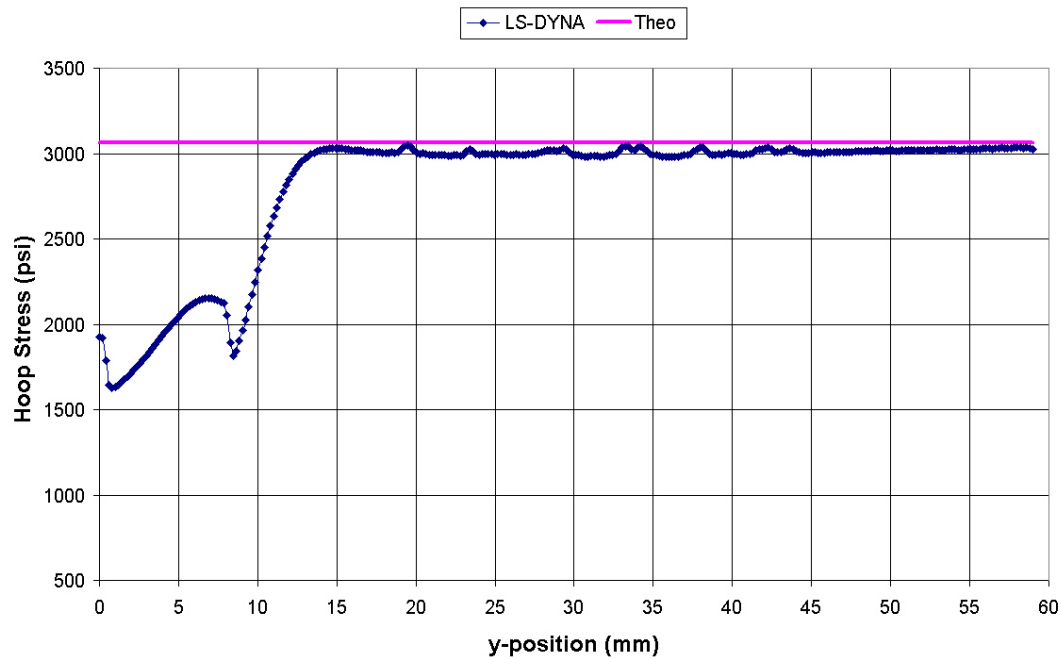


**Figure A.4** Outer cylinder hoop stress distribution for shrink fit model #2 with 2400 elements

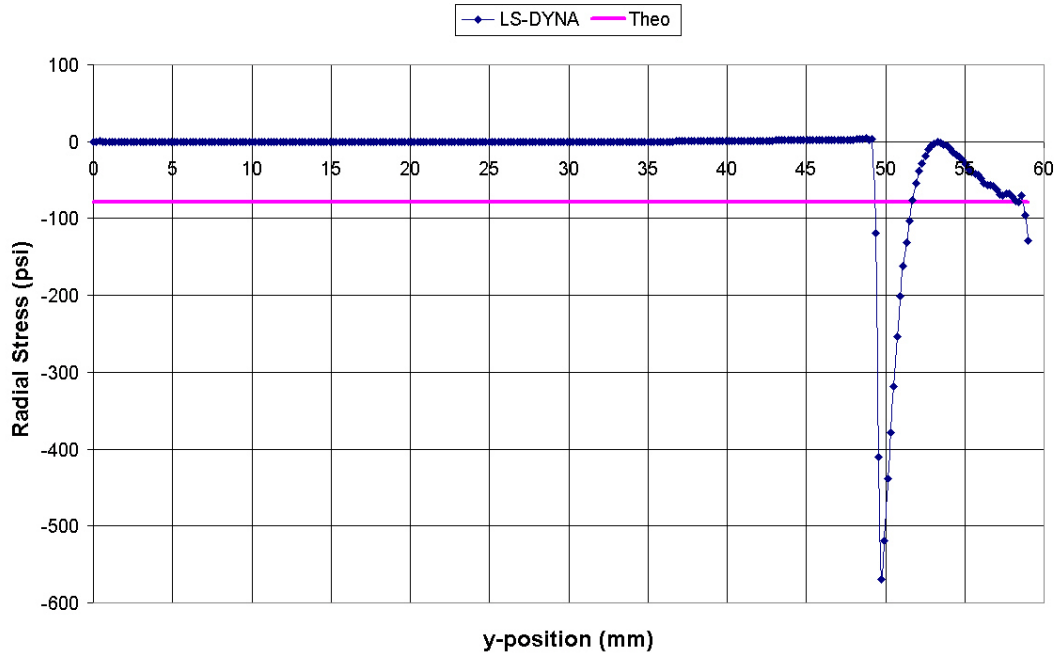


**Figure A.5** Outer cylinder radial stress distribution for shrink fit model #7 with 2400 elements

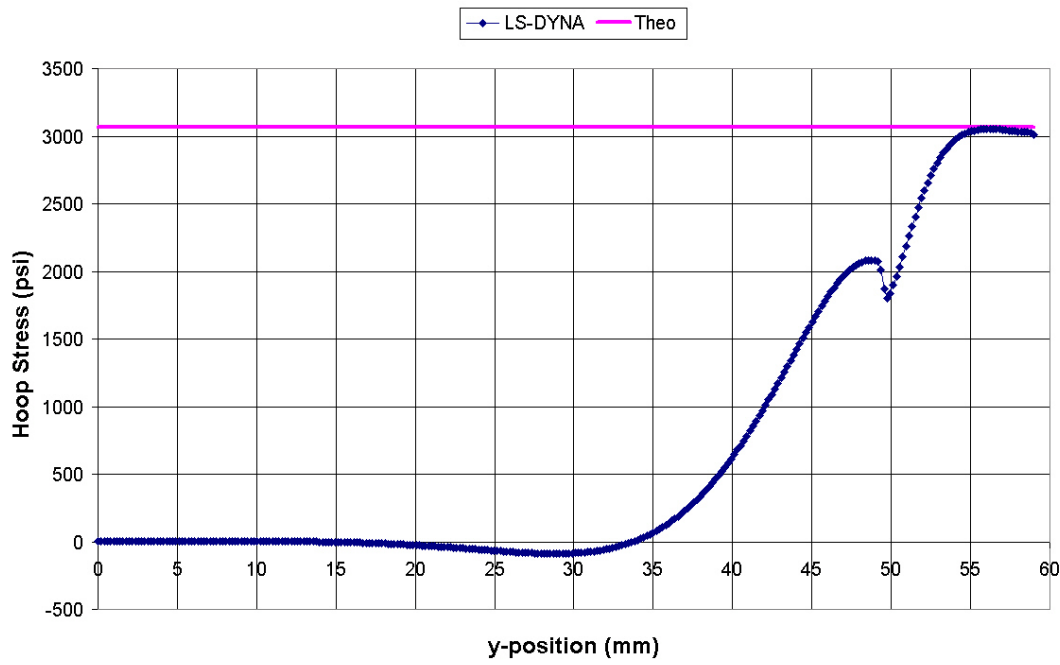


**Figure A.6** Outer cylinder radial stress distribution for shrink fit model #7 with 2400 elements

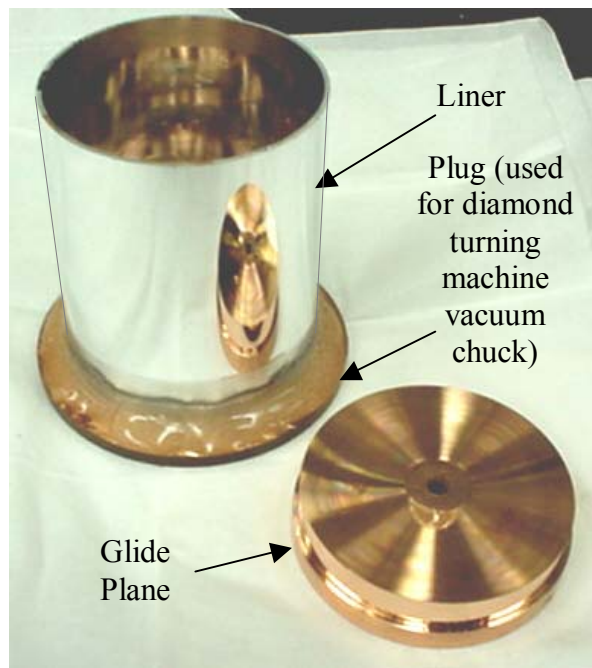


**Figure A.7** Test Specimen #3 components fabricated using the ASG-2500 Diamond Turning Machine

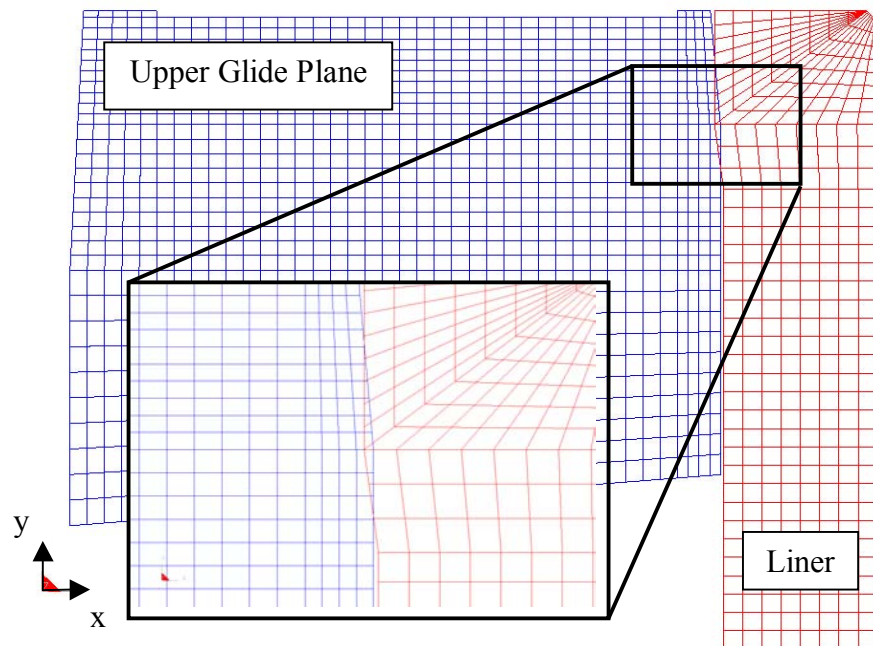


**Figure A.8** ATLAS Generation II glide plane/liner interface

## APPENDIX B

```
$ The following is a typical LS-DYNA code for an axisymmetric model such as ATLAS
$ Generation I.
$  
$ Each "Card" consists of eight columns, each with various parameters falling
$ under a given column.
$  
*KEYWORD
$  
$-----1-----2-----3-----4-----5-----6-----7-----8
$  
$ DYNA3D(936) DECK WAS WRITTEN BY: ETA/FEMB VERSION 26
$ DATE: Aug 1, 2001 at 14:36:14
$  
$-----1-----2-----3-----4-----5-----6-----7-----8
$ (1) TITLE CARD.
$-----1-----2-----3-----4-----5-----6-----7-----8
*TITLE
ATLAS_GENERATION_I
$  
$-----1-----2-----3-----4-----5-----6-----7-----8
$ (2) CONTROL CARDS.
$-----1-----2-----3-----4-----5-----6-----7-----8
*CONTROL_TERMINATION
$  
$ Specified time length of simulation (1.00 "seconds")
$  
$ ENDTIM    ENDCYC      DTMIN     ENDNEG     ENDMAS
.100E+01          0       .000       .000       .000
$  
*CONTROL_IMPLICIT_GENERAL
$  
$ Implicit time step size (100 time steps total)
$  
$ IMFLAG      DT0       IMFORM      NSBS       IGS
      1       0.01        1           1           1
$  
*CONTROL_IMPLICIT_SOLUTION
$  
$ "2" represents an implicit solution technique
$  
$ NSOLVR
      2
$  
*CONTROL_HOURGLASS
$ IHQ      QH
      1       .100
*CONTROL_BULK_VISCOSITY
$ Q2      Q1
      1.500     .060
*CONTROL_SHELL
$ WRPANG    ITRIST      IRNXX     ISTUPD      THEORY      BWC      MITER
      20.000     2         -1          0          2          2          1
*CONTROL_CONTACT
$ SLSFAC    RWPNAL      ISLCHK     SHLTHK     PENOPT     THKCHG     ORIEN
      .100
```

```

$    USRSTR      USRFAC      NSBCS      INTERM      XPENE
      0          0           10          0       4.000
$    SFRIC      DFRIC       EDC        VFC        TH      TH_SF      PEN_SF
*CONTROL_ENERGY
$    HGEN       RWEN       SLNTEN      RYLEN
      1          2           1           1
*CONTROL_DAMPING
$    NRCYCK      DRTOL      DRFCTR      DRTERM      TSSFDR      IRELAL      EDTTL      IDRFLG
      250       .001       .995
*CONTROL_OUTPUT
$    NPOPT       NEECHO      NREFUP      IACCOP      OPIFS      IPNINT      IKEDIT
      0          0           0           0       .000          0       100
$
$----+---1----+---2----+---3----+---4----+---5----+---6----+---7----+---8
$              (3) DATABASE CONTROL CARDS - ASCII HISTORY FILE
$----+---1----+---2----+---3----+---4----+---5----+---6----+---7----+---8
$ *DATABASE_HISTORY_OPTION
$    ID1        ID2        ID3        ID4        ID5        ID6        ID7        ID8
$
$    OPTION: BEAM      BEAM_SET     NODE      NODE_SET
$            SHELL      SHELL_SET    SOLID     SOLID_SET
$            TSHELL     TSHELL_SET
$
$----+---1----+---2----+---3----+---4----+---5----+---6----+---7----+---8
$              (4) DATABASE CONTROL CARDS FOR ASCII FILE
$----+---1----+---2----+---3----+---4----+---5----+---6----+---7----+---8
$    OPTION: SECFORC   RWFORC     NODOUT    ELOUT     GLSTAT
$            DEFORC     MATSUM     NCFORC    RCFORC    DEFGEO
$            SPCFORC   SWFORC     ABSTAT    NODFOR   BNDOUT
$            RBDOUT     GCEOUT    SLEOUT    MPGS     SBTOUT
$            JNTFORC   AVSFLT    MOVIE
$
$----+---1----+---2----+---3----+---4----+---5----+---6----+---7----+---8
$              (5) DATABASE CONTROL CARDS FOR BINARY FILE
$----+---1----+---2----+---3----+---4----+---5----+---6----+---7----+---8
$ Frequencies of post-processor plot outputs
$
*DATABASE_BINARY_D3PLOT
$    DT/CYCL      LCDT      NOBEAM
      .500E-01
*DATABASE_BINARY_D3THDT
$    DT/CYCL      LCDT      NOBEAM
      .500E-01
$ *DATABASE_BINARY_OPTION
$    DT/CYCL      LCDT      NOBEAM
$
$    OPTION: D3DRFL  D3DUMP   RUNRSF  INTFOR
$ 
$----+---1----+---2----+---3----+---4----+---5----+---6----+---7----+---8
*DATABASE_EXTENT_BINARY
      0          0           3           0           1           1           1           1
      0          0           0           0           0           0
$----+---1----+---2----+---3----+---4----+---5----+---6----+---7----+---8

```

```

$-----1-----2-----3-----4-----5-----6-----7-----8
$ (6) DEFINE PARTS CARDS
$-----1-----2-----3-----4-----5-----6-----7-----8
$ PID = "Part ID"
$ SID = "Section ID"
$ MID = "Material ID"
$
*PART
$HEADING
  PART PID =      1 PART NAME : SMALL GP
$    PID      SID      MID      EOSID      HGID      GRAV      ADPOPT      TMID
    1          1          1
*PART
$HEADING
  PART PID =      2 PART NAME : LINER
$    PID      SID      MID      EOSID      HGID      GRAV      ADPOPT      TMID
    2          1          2
*PART
$HEADING
  PART PID =      3 PART NAME : LARGE GP
$    PID      SID      MID      EOSID      HGID      GRAV      ADPOPT      TMID
    3          1          1
$-----1-----2-----3-----4-----5-----6-----7-----8
$ (7) MATERIAL CARDS (MATERIAL PROPERTIES)
$-----1-----2-----3-----4-----5-----6-----7-----8
*MAT_ELASTIC_PLASTIC_THERMAL
$MATERIAL NAME: COPPER
$    MID      RHO
      1 1.000E+00
$    T1      T2
      0      500
$    E1      E2
      1.595E7  1.595E7
$    PR1      PR2
      0.35     0.35
$    ALPHA1   ALPHA2
      9.1E-6   9.1E-6
$    SIGY1    SIGY2
      50000    50000
$    ETAN1    ETAN2
      1E-3     1E-3
$
*MAT_ELASTIC_PLASTIC_THERMAL
$MATERIAL NAME: 1100 ALUMINUM
$    MID      RHO
      2 1.000E+00
$    T1      T2
      0      500
$    E1      E2
      1.001E7  1.001E7
$    ALPHA1   ALPHA2
      0.33     0.33
$    ALPHA1   ALPHA2
      13.0E-6  13.0E-6
$    SIGY1    SIGY2
      5000     5000
$    ETAN1    ETAN2
      1E-3     1E-3
$-----1-----2-----3-----4-----5-----6-----7-----8

```





```

$-----1-----2-----3-----4-----5-----6-----7-----8
$ (17) DEFINE LOADS
$-----1-----2-----3-----4-----5-----6-----7-----8
$ Loads representing weights of parts
$
*LOAD_NODE_POINT
$     NODE      DOF      LCID      SF      CID      M1      M2      M3
      390       2        3     -22.32
      6825      2        3     -1.14
$
$-----1-----2-----3-----4-----5-----6-----7-----8
$ (18) DEFINE CURVE
$-----1-----2-----3-----4-----5-----6-----7-----8
$ Points defined along each curve (A's are x-values, O's are y-values)
$
$ CURVE #1: USED FOR THERMAL LOADING
*DEFINE_CURVE
$     LCID      SIDR      SCLA      SCLO      OFFA      OFFO
      1          0
$           A1          O1
          0.00      0.0000
          0.25      1.0000
          0.50      0.0000
          0.80      0.0000
$ CURVE #2: USED FOR UPWARD MOTION
*DEFINE_CURVE
$     LCID      SIDR      SCLA      SCLO      OFFA      OFFO
      2          0
$           A2          O2
          0.000      0.00000
          0.750      0.00001
          0.800      0.05000
$ CURVE #3: USED FOR APPLIED LOADS
*DEFINE_CURVE
$     LCID      SIDR      SCLA      SCLO      OFFA      OFFO
      3          0
$           A3          O3
          0.000      0.0000
          0.500      0.0000
          0.750      1.0000
          0.800      1.0000
$
$-----1-----2-----3-----4-----5-----6-----7-----8
$ (19) LOCAL COORDINATE SYSTEM
$-----1-----2-----3-----4-----5-----6-----7-----8
$-----1-----2-----3-----4-----5-----6-----7-----8
$ (20) NODAL CONSTRAINT CARDS
$-----1-----2-----3-----4-----5-----6-----7-----8

```

```

$-----1-----2-----3-----4-----5-----6-----7-----8
$ (21) DEFINE CONTACT SURFACE
$-----1-----2-----3-----4-----5-----6-----7-----8
$ PSIDS = "Slave Part"
$ PSIDM = "Master Part"
$ SFACT = "Spring Factor" or "Penalty Factor"
$ TBIRTH = "Birth Time of Contact"
$ FS = "Static Frictional Coefficient"
$ FD = "Dynamic Frictional Coefficient"
$
*CONTACT_2D_AUTOMATIC_SURFACE_TO_SURFACE
$   PSIDS      PSIDM      SFACT      FREQ          FS        FD      DC      MEMBE
      2           1       100.0
$   TBIRTH     TDEATH      SOS       SOM       NDS       NDM    IPFLG      INIT
      0.251
*SET_PART_LIST
$   SID        DA1        DA2        DA3        DA4
      1
$   PID1       PID2       PID3       PID4
      1       3
*SET_PART_LIST
$   SID        DA1        DA2        DA3        DA4
      2
$   PID1       PID2       PID3       PID4
      2
$
$-----1-----2-----3-----4-----5-----6-----7-----8
$ (22) DEFINE RIGID WALL
$-----1-----2-----3-----4-----5-----6-----7-----8
*END

```